Ultraclean carbon nanotubes and superconducting coplanar resonators: Materials, nano-electromechanics, and few-electron systems

Dissertation

zur Erlangung des Doktorgrades der Naturwissenschaften (Dr. rer. nat)
der Fakultät Physik der Universität Regensburg

vorgelegt von

Peter Stiller

aus Laub

unter Anleitung von Dr. Andreas K. Hüttel

Januar 2016

Das Promotionsgesuch wurde am 26.10.2015 eingereicht.
Das Kolloquium fand statt am 06.04.2016.

Die Arbeit wurde von Dr. Andreas K. Hüttel angeleitet.

Prüfungsausschuss:	Vorsitzender:	Prof. Dr. Klaus Richter
	1. Gutachter:	Dr. Andreas K. Hüttel
	2. Gutachter:	Prof. Dr. Jascha Repp
	weiterer Prüfer:	Prof. Dr. Rupert Huber

Für meine Eltern

Contents

List of Figures viii

List of Tables ix

List of Symbols x

1 Introduction 1

2 Fundamental electronic properties of carbon nanotubes 5
- 2.1 Carbon nanotube lattice . . . 6
- 2.2 Carbon nanotube band structure . . . 8

3 Fabrication and measurement techniques for CNT devices 13
- 3.1 Fundamental nanofabrication techniques . . . 15
- 3.2 Electrode geometry for the carbon nanotube overgrowth . . . 17
- 3.3 Room temperature characterization . . . 17
- 3.4 The dilution refrigerator . . . 20

4 Electronic transport through CNT quantum dots 23
- 4.1 Quantum dots . . . 24
- 4.2 Carbon nanotube quantum dots . . . 27
- 4.3 Quantum dot transport spectroscopy . . . 28

5 Carbon nanotubes in a parallel magnetic field 33
- 5.1 Carbon nanotube single particle spectrum . . . 34
- 5.2 Quantum mechanical transmission . . . 38
- 5.3 Transmission calculations for different kinds of CNTs . . . 40
- 5.4 Magnetic field dependence of $k_{\parallel}$ . . . 45

5.5 Comparison of numerical and analytical results . . . 48
5.6 Numerical calculations and the measured spectrum . . . 50

6 Magnetic field induced electron-vibron coupling 53
6.1 Vibrational modes in carbon nanotubes . . . 54
6.2 Franck-Condon model . . . 56
6.3 Magnetic field induced coupling . . . 58
6.4 Physical origin of the magnetic field induced coupling . . . 62

7 Negative frequency tuning of a CNT mechanical resonator 65
7.1 Mechanical properties of suspended, doubly clamped CNTs . . . 66
7.2 Gate tuning of mechanical resonance . . . 67
7.3 Measurement setup and detection technique . . . 68
7.4 Electronic device characterization . . . 68
7.5 Driven mechanical resonator . . . 71
7.6 Negative frequency tuning . . . 72

8 Coplanar waveguide resonators for CNT integrated circuits 77
8.1 Device fabrication . . . 78
8.2 Microwave frequency measurement setup . . . 81
8.3 Quality factor evaluation . . . 83
8.4 Characterization of niobium quarter wavelength resonators . . . 85
8.5 Two-level system loss in CPWs . . . 88
8.6 Matthis Bardeen theory for CPWs . . . 95
8.7 Calculating the kinetic inductance fraction . . . 97
8.8 Combining CNT and CPW . . . 98

9 Conclusions and outlook 103

A Fabrication details and recipes 107
A.1 Carbon nanotube quantum dot devices . . . 107
A.2 Coplanar waveguide fabrication . . . 112

B Calculating a theoretical value β 114

C Numerical transmission calculations of carbon nanotubes 116
C.1 Hopping integrals . . . 116
C.2 Additional transmission calculations . . . 117

D Coplanar waveguide parameters 120
D.1 Calculation of the effective permittivity . . . 120
D.2 Resonant and relaxation susceptibility tensors . . . 122

E HF measurement technology 124

List of Figures

2.1 Definition of carbon nanotube chiral vector and translation vector 7
2.2 Tight binding calculation of graphene dispersion relation 9
2.3 Tight binding calculation of carbon nanotube band structures . . 11

3.1 Device fabrication for overgrown carbon nanotubes 14
3.2 Carbon nanotube growth setup 16
3.3 SEM image of overgrown carbon nanotubes 18
3.4 Device geometry for rhenium contact electrodes 19
3.5 SEM image of the device geometry for rhenium and molybdenum alloys 19
3.6 Carbon nanotube room temperature characterization 20
3.7 Functionality of a dilution refrigerator 21

4.1 Sketch of a quantum dot and its coupling to the environment . . . 24
4.2 Single electron transport through a quantum dot 26
4.3 Band structures at the carbon nanotube-metal interface 28
4.4 Sketch of the conductance as a function of both gate voltage and bias voltage 30
4.5 Current and conductance measurements as function of gate voltage and bias voltage 31

5.1 Dispersion relation near the K and K' points 36
5.2 Comparison of the measured carbon nanotube single particle spectrum and an analytic model 37
5.3 Calculated transmission for a $(5, 2)$ carbon nanotube 42
5.4 Calculated transmission for a $(29, 20)$ carbon nanotube 44
5.5 Magnetic field values for the Dirac point crossing as a function of the radius and the chiral angle of a carbon nanotube 45

5.6 Calculated transmission for a $(29, 20)$ carbon nanotube with different length . . . 46
5.7 Magnetic field values for the Dirac point crossing as a function of the length of a carbon nanotube . . . 47
5.8 Dependence of the momentum shift $k_{\parallel}$ on the momentum shift $k_{\perp}$ 48
5.9 Comparison of numerical transmission calculations and an analytic model . . . 51

6.1 Vibrational modes in carbon nanotubes . . . 55
6.2 Poisson distribution for the Franck-Condon model . . . 58
6.3 Current and conductance as a function of both bias voltage and parallel magnetic field . . . 59
6.4 Traces of the conductance and the current as a function of bias voltage for constant parallel magnetic field . . . 60
6.5 Electron-vibron coupling factor as function of a parallel magnetic field . . . 60
6.6 Conductance as a function of both bias voltage and parallel magnetic field . . . 62
6.7 Comparison of two different methods to obtain the electron-vibron coupling parameter . . . 63
6.8 Maximal current of the ground state as a function of a parallel magnetic field . . . 64

7.1 Low temperature measurement setup . . . 69
7.2 Photograph of the contact-free cryogenic antenna . . . 70
7.3 Room temperature conductance measurement . . . 70
7.4 Low temperature conductance measurement . . . 71
7.5 Conductance as function of both gate voltage and bias voltage displaying the so-called Coulomb diamond stability diagram . . . 72
7.6 Current as a function of the applied radio frequency . . . 73
7.7 Negative frequency tuning of a carbon nanotube mechanical oscillator . . . 74

8.1 SEM image of the coplanar waveguide design . . . 79
8.2 Critical temperature of niobium . . . 80
8.3 Photograph of the used sample holder system . . . 81
8.4 Photograph of our dilution system and microwave setup . . . 82
8.5 Photograph of the HEMT amplifier and the circulator . . . 83
8.6 $|S_{21}|^2$ transmission of a niobium coplanar waveguide resonator . . . 85
8.7 Characterization of a niobium resonator at 4 K . . . 86
8.8 Temperature dependence of a resonance feature of a niobium coplanar waveguide resonator . . . 87

8.9 Internal quality factor of a niobium coplanar waveguide resonator as a function of temperature 88
8.10 Resonance frequency of a niobium coplanar waveguide resonator as a function of temperature 89
8.11 Two-level system fit for a niobium coplanar waveguide resonator . 92
8.12 Power dependence of two-level system loss in a niobium coplanar waveguide resonator 94
8.13 Matthis Bardeen fit for a niobium coplanar waveguide resonator . 96
8.14 Room temperature conductance measurement 100
8.15 SEM image of a potential sample design for combining carbon nanotubes and coplanar waveguide resonator 101

B.1 Height dependence of the second derivative C''_{gate} 115

C.1 Coordinates for the hopping integrals 117
C.2 Calculated transmission for a $(14, 11)$ carbon nanotube with different length 118
C.3 Calculated transmission through different carbon nanotubes . . . 119

D.1 Sketch for the calculation of ϵ_{eff} 121

List of Tables

2.1 Solutions $E(k_x, k_y) = 0$ of the graphene dispersion relation $E(k_x, k_y)$ 8

5.1 Extracted values of an analytic fit of the measured carbon nanotube single particle spectrum 38
5.2 Magnetic field values for the Dirac point crossing for different kinds of carbon nanotubes obtained from numerically transmission calculations 41

8.1 Design frequencies of our coplanar waveguide resonator resonators 80
8.2 Resonance frequencies of a niobium coplanar waveguide resonator at 4 K 86
8.3 Comparison of our results obtained by influence of two-level systems with literature 93
8.4 Comparing different qubit-photon coupling experiments 100

List of Symbols

a	Lattice constant of graphene ($a = 2.46 \cdot 10^{-10}\,\mathrm{m}$)	6
$\vec{a}_{1,2}$	Unit vectors of the hexagonal graphene lattice	6
A	Cross section	66
$B_{\parallel}$	Parallel magnetic field	33
B_{min}	Parallel magnetic field corresponding to the Dirac point crossing	36
$C_{\Sigma,s,d,g}$	Total, source, drain and gate capacitances of a quantum dot	27
$\vec{C}_h$	Chiral vector	6
d	Lead coupling parameter	40
d_{CNT}	Diameter	7
$\vec{d}$	Dipole moment	90
δ	Spin-orbit coupling parameter	35
Δ_0	Tunnel splitting	88
Δ_{BCS}	BCS energy gap	95
$\Delta_{T=0}$	Superconducting energy gap for $T = 0$	95
δ_{TLS}	Two-level system loss tangent	91
δ^*_{TLS}	Effective, reduced two-level system loss tangent	91
Δ_{TLS}	Two-level system asymmetry	88
$\Delta k_{\perp}$	Sub-band spacing	8
$\Delta\epsilon$	Energy splitting induced by charge carrier quantum confinement	8
$\Delta_{\mathrm{KK'}}$	KK' splitting	34
Δ_{SO}	Spin-orbit splitting	34
e	Elementary charge, $e = 1.602 \cdot 10^{-19}\,\mathrm{C}$	23
E	Young's modulus	66

E_C	Charging energy of a quantum dot	24
E_i	Quantum dot ground state energy with i charge carriers	25
E_{RBM}	Energy of the radial breathing mode	54
E_{SM}	Energy of the stretching mode	55
ϵ	Eigenenergies	90
ϵ_0	Vacuum permittivity ($\epsilon_0 \simeq 8.854 \cdot 10^{-12}\,\mathrm{A\,s/(V\,m)}$)	67
ϵ_{eff}	Effective permittivity	78
η	Linear damping	66
f_{design}	Designed resonance frequency of a CPW resonators	78
f_{res}	Measured resonance frequency of a CPW resonators	84
F	Two-level system filling factor	91
F_{ac}	Time-dependent external force	67
F_{dc}	Static external force	67
F_{ext}	External force driving a carbon nanotube	66
g	Electron-phonon coupling parameter	53
$g_{\mathrm{g,f}}$	Geometrical factors for ground plane and CPW feedline	97
G	Conductance	23
G_{CNT}	Maximal carbon nanotube conductance	23
Γ	Tunneling rate	56
$\hbar$	Reduced Planck constant, $\hbar = 6.58 \cdot 10^{-16}\,\mathrm{eVs}$	2
h	Vertical distance height between gate and carbon nanotube	67
h_0	Equilibrium height	67
I	Momentum of inertia	66
I_{max}	Maximal current at the ground state	58
$k_\perp$	Wave vector perpendicular to the carbon nanotube axis	9
$k_\parallel$	Wave vector parallel to the carbon nanotube axis	8
k_b	Boltzmann constant, $k_b = 8.62 \cdot 10^{-5}\,\mathrm{eVK^{-1}}$	2
l	Classical displacement of carbon nanotube lattice	56
l_0	Length scale of the quantum harmonic oscillator	56
l_{cpw}	Length of the meandering CPW resonator	78
L	Length of a suspended carbon nanotube	66
$L_{k,m}$	Kinetic and magnetic inductance per unit length	97
λ_F	Fermi wavelength	26
μ	Electro-chemical potential of a quantum dot	25
μ_B	Bohr magneton, $\mu_B \simeq 5.788 \cdot 10^{-5}\,\mathrm{eV/T}$)	38

$\mu_{s,d}$	Electro-chemical potential of source and drain	25
n, m	Chiral indices	6
n_s	Charge carrier density of states	26
n_{vib}	Vibrational mode number	55
N	Number of charge carriers	25
P	Output power of a RF generator	71
$P_{\text{generator}}$	Output power of a microwave generator	85
P_{in}	Effective input power at the sample	85
P_{TLS}	Two-level system density of states	90
Φ_0	Magnetic flux quantum	33
Ψ_i	Vibrational wave function	56
Q_c	Coupled quality factor	84
Q_e	External quality factor	84
Q_i	Internal quality factor	84
Q_l	Loaded quality factor	84
R_{CNT}	Carbon nanotube device resistance	69
ρ	Mass density	66
s	Distance between CPW feedline and ground plane	78
S_{ij}	Scattering matrix element from port j to port i	83
σ	Valley quantum number	34
σ_i	Pauli matrices	90
$\sigma_{1,2}$	Real and imaginary part of the complex conductivity	95
T	Sample temperature	2
T_0	Residual tension	66
T_{ac}	Time-dependent tension	67
T_c	Critical temperature	78
T_{dc}	Static tension	67
T_{mech}	Tension	66
$\vec{T}$	Translation vector	6
τ	Spin quantum number	34
Θ	Chiral angle	6
U_{ac}	Time-dependent displacement	66
U_{dc}	Static displacement	66
$U(z,t)$	Time dependent elongation	66
v_F	Fermi velocity	34

V_{bias}	Bias voltage	28
V_{gate}	Gate voltage	28
V_i^{in}	Voltage input at port i	83
V_i^{out}	Voltage output at port i	83
w	Width of the CPW feedline	78
$\xi_{\text{res,rel}}$	Resonant and relaxation tensor	90
Z	Atom number of a carbon nanotube unit cell	6

CHAPTER 1

Introduction

Carbon nanotubes are a prominent carbon based nano-material. In 1952 first multi-walled carbon nanotubes were discovered in TEM images [Radushkevich and Luk'yanovich, 1952]. Subsequently, single-walled carbon nanotubes were observed in discharge experiments [Iijima and Ichihashi, 1993, Bethune et al., 1993]. Ongoing progress in nano-fabrication techniques lead to first measurements of single carbon nanotubes contacted to metallic leads; showing a quantum wire like transport at low temperatures [Tans et al., 1997] and transistor behavior at room temperature [Tans et al., 1998]. Further improvements of fabrication techniques and measurement setups led to a rich field of carbon nanotube physics. Nowadays carbon nanotubes can be grown defect-free directly on the substrate by chemical vapor deposition. Carbon nanotubes are intrinsic one-dimensional conductors, and the formation of a "zero-dimensional" quantum dot system is straightforward compared, e.g., to electrostatically constricting a two-dimensional electron gas. The quantum confinement of electrons in carbon nanotubes leads to a rich spectrum of transport phenomena; many different parameter regimes have already been observed. Carbon nanotubes display Luttinger-liquid behavior [Bockrath et al., 1999, Postma et al., 2001], show ballistic transport [Cao et al., 2005] and Fabry-Perot like oscillations in an open transport regime [Liang et al., 2001]. Carbon nanotubes can be connected to many different types of metallic leads, including ferromagnetic [Jensen et al., 2005] and superconducting materials [Morpurgo et al., 1999].

In addition, carbon nanotubes also show excelling mechanical properties, having a low mass, high stiffness and an extremely high Young's modulus [Lu, 1997]. They can act as mechanical beam resonators on the nano-scale [Sazonova et al., 2004], achieving high-quality factors in carbon nanotube nano-electromechanical devices [Hüttel et al., 2009a]. Recently quality factors of the mechanical bending

mode vibration of a carbon nanotube resonator up to $5 \cdot 10^6$ were demonstrated [Moser et al., 2014]. Low mass and ultimate quality factor made it possible to employ carbon nanotubes as ultra-sensitive mass sensors [Lassagne et al., 2008]. Due to their high mechanical resonance frequency of several hundreds of megahertz [Hüttel et al., 2009a, Stiller et al., 2013] carbon nanotubes also provide a promising system for reaching the quantum limit of mechanical motion. This requires $k_b T << \hbar\omega$, which can here be in principle directly reached with common dilution refrigerators.

A rather new development regarding carbon nanotubes is the integration in superconducting microwave circuits. Coplanar waveguides (CPW) were first suggested in [Wen, 1969], here a transmission strip-line is fabricated on a dielectric substrate material. Later CPWs were used as superconducting resonators [Day et al., 2003]; the small size of CPW resonators allowed the integration in on-chip microwave circuits. In [Wallraff et al., 2004] the combination of a CPW resonator acting as an on-chip cavity and a qubit defined in a cooper pair box was presented leading to a solid state based cavity quantum electrodynamic system, a proposal first was given by [Blais et al., 2004, Childress et al., 2004]. The Cooper pair box acts as a charge qubit; its states are coupled to the electric field of the transmission line resonator. A qubit is a fully manipulable quantum mechanical two-level system; it is the basic unit for quantum computing and quantum cryptography. The microwave resonator can be employed for read-out and manipulation of the qubit quantum states. As an example, a single electron in a double quantum dot or the polarization of a single photon can act as a qubit. The experiments coupling a superconducting microwave resonator and a qubit target the fundamental interaction of matter and light [Jaynes and Cummings, 1963, Childress et al., 2004]. The Jaynes-Cummings model describes the interaction of a two-level system and a quantized harmonic mode of an optical cavity; by using a superconducting microwave resonator and an artificial atom, an analogon to a optical cavity can be achieved.

Carbon nanotubes are a common material to define single and double quantum dots, allowing also the formation of a charge or spin qubits; the absence of hyperfine interaction in carbon yields a large spin decoherence time in carbon nanotubes necessary for a manipulation of spin states [Fischer et al., 2009].

Recently the combination of a carbon nanotube single [Delbecq et al., 2011] and double quantum dot [Viennot et al., 2014, Viennot et al., 2015] and a half wavelength CPW resonator was presented. In carbon nanotubes the confinement of electrons is much stronger than in a two-dimensional electron gas since they are smaller in size and intrinsically one-dimensional. Furthermore carbon nanotubes can display large electric dipole moments leading to a much stronger coupling of both systems.

For the combination of carbon nanotube quantum dots and CPW resonators, a reliable fabrication for both systems is necessary. In this thesis electronic and mechanical experiments on clean, suspended carbon nanotubes are presented; in

addition first measurements of niobium quarter wavelength CPW resonators are shown.
This thesis starts with a short introduction of the fundamental electronic properties of carbon nanotubes in chapter 2. In the following chapter 3 the fabrication process for overgrown carbon nanotube devices is explained. In addition the required room temperature and low temperature measurement setups are shown. Chapter 4 presents the basic concept of quantum dot systems in carbon nanotubes. Numerical transmission calculations on carbon nanotubes and the influence of a parallel magnetic field on the carbon nanotube single particle spectrum are shown in chapter 5 with the objective to identify the chirality of a measured carbon nanotube. The interaction of phonons and electrons in carbon nanotubes and the influence of a magnetic field is discussed in chapter 6. Chapter 7 discusses a specific device where an applied gate voltage enables negative frequency tuning of the carbon nanotube mechanical resonator. Preparatory measurements on superconducting quarter-wavelength resonators are shown in chapter 8, discussing also the potential design of the combination of superconducting resonators and carbon nanotubes. Finally the experimental results of this thesis are concluded, and a short outlook on possible future experiments is given. Technical details to the different chapters are additionally presented in the appendix.

CHAPTER 2

Fundamental electronic properties of carbon nanotubes

In this chapter a brief overview of the fundamental properties of carbon nanotubes is given. First, the lattice quantities defining a carbon nanotube are explained. Then the band structure in zone-folding approximation is demonstrated.
The carbon atom, foundation of all organic chemistry, has an electronic shell configuration of $2s^1\,2s^2\,2p^2$, i.e. every carbon atoms has six electrons. Particular for carbon are the well known sp, sp^2, and sp^3 hybridizations leading to the wide field of organic chemistry; a linear combination of the $2s^2$ electron and the $2p^2$ electrons form energetically degenerate hybridized orbitals. An sp^3 hybridized carbon atom forms four covalent bonds via hybridization of the 2s orbital and the three 2p orbitals; this forms for instance diamond. The four hybridized orbitals are arranged in a tetrahedron like structure to maximize the distance between them. Another well known carbon compound, graphite, consists of sp^2 hybridized carbon atoms. Here the 2s orbital and two 2p orbitals form three hybridized orbitals. These are arranged in a plane with an angle of 120° between each hybridized orbital. This builds up a hexagonal lattice, which is sketched in figure 2.1. Graphite consists of many of these layers adhering via van-der-Waals interaction. One single layer is called graphene; a recently isolated two dimensional nano-scale material. The fabrication of single layer graphene started a new field in physics due to the excelling electronic properties of graphene [Novoselov et al., 2004]. The investigation was honored with the Nobel prize in 2010. Since that time many different researchers work on graphene. In this case of sp^2 hybridization, the third, non-hybridized p orbital of the carbon atoms in graphene forms delocalized π orbitals. These are responsible for the electronic transport since σ bonds are far away form the Fermi energy and do not contribute to electronic transport. Carbon nanotubes can be imaged as rolled up graphene sheets; so it is not surprising to start with the graphene lattice to derive the properties of carbon nanotubes.

2.1 Carbon nanotube lattice

Starting from graphene one can define the basic lattice parameters of carbon nanotubes. The two atom unit cell of graphene is defined by two primitive lattice vectors $\vec{a}_1$ and $\vec{a}_2$ (see figure 2.1) and a corresponding bond length $a_{\text{bond}} = 1.42\,\text{Å}$. The resulting lattice constant reads

$$a = |\vec{a}_1| = |\vec{a}_2| = a_{\text{bond}}\sqrt{3} = 2.46\,\text{Å}. \tag{2.1}$$

An important quantity for carbon nanotubes is the so-called chiral vector

$$\vec{C}_h = n\vec{a}_1 + m\vec{a}_2; \tag{2.2}$$

defining the roll-up direction for carbon nanotubes. In a thought-experiment, where a graphene sheet is rolled up into a carbon nanotube it subsequently lies along the circumference of the carbon nanotube. Together with the translation vector $\vec{T}$ it defines the carbon nanotube unit cell. The translation vector reads

$$\vec{T} = \frac{2m+n}{g} \cdot \vec{a}_1 - \frac{2n+m}{g} \cdot \vec{a}_2, \tag{2.3}$$

with g being the greatest common divisor of $(2m+n)$ and $(2n+m)$. The atom number Z within one unit cell can be calculated using the vectors $\vec{C}$ and $\vec{T}$; the results is

$$Z = 2 \cdot \frac{|\vec{C} \times \vec{T}|}{|\vec{a}_1 \times \vec{a}_2|}. \tag{2.4}$$

As one can easily see each carbon nanotube is fully described by its chiral indices n and m, see figure 2.1. The chiral angle is given by

$$\cos(\Theta) = \frac{\vec{C} \cdot \vec{a}_1}{|\vec{C}||\vec{a}_1|} = \frac{2n+m}{2\sqrt{n^2+nm+m^2}} \tag{2.5}$$

and is defined as the angle between $\vec{a}_1$ and $\vec{C}_h$. The hexagonal lattice restricts the chiral angle to values between $\Theta = 0°$ and $\Theta = 30°$.
Depending on Θ different carbon nanotube classes arise. For $\Theta = 0°$ a so-called zigzag type carbon nanotube is obtained and for $\Theta = 30°$ the carbon nanotube is of armchair type. Both types are so-called achiral carbon nanotubes since they

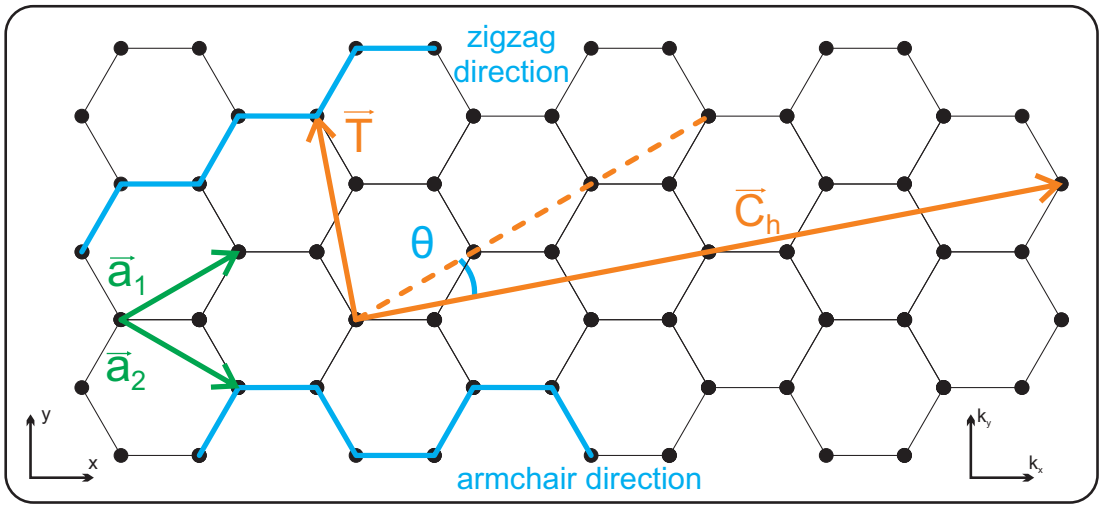

Figure 2.1: Sketch of a graphene lattice. The carbon atoms are depicted as black dots. The two lattice vectors $\vec{a}_1$ and $\vec{a}_2$, the chiral vector $\vec{C}_h$ and the translation vector $\vec{T}$ of an exemplary $(4, 2)$ carbon nanotube are shown. Zig-zag and armchair directions are depicted in cyan. The names arise from the shape of the circumference.

have a mirror symmetry, all other types of carbon nanotubes are called chiral. The roll-up direction for both types is sketched in figure 2.1.
The diameter of a (n, m) carbon nanotube reads

$$d_{\mathrm{CNT}} = \frac{|\vec{C}|}{\pi} = \frac{a\sqrt{n^2 + nm + m^2}}{\pi}, \tag{2.6}$$

which is typically in the range of a few nanometers. These values are the basic quantities defining the carbon nanotube lattice. To derive an approximation for the band structure and the electronic properties of a carbon nanotube one starts with the dispersion relation for the π electrons of graphene

$$E(k_x, k_y) = \pm \left\{ 1 + 4\cos\left(\frac{\sqrt{3}k_x a}{2}\right)\cos\left(\frac{k_y a}{2}\right) + 4\cos^2\left(\frac{k_y a}{2}\right) \right\}^{1/2}, \tag{2.7}$$

obtained using a tight binding approximation; a more detailed discussing can be found in [Saito et al., 1998].

Figure 2.2(a) shows this well-known dispersion relation of graphene. The π and π^* bands touch each other at the corners of the reciprocal first Brillouin zone, these corner points are labeled as K in solid state physics. Only two of the six corner points are independent in the reciprocal graphene lattice, the other points are connected by lattice vectors. In graphene and carbon nanotubes the two independent points are labeled K and K'. The dispersion relation becomes linear near the K and K' points. Graphene is a so-called zero band gap semiconductor since the density of states at the Fermi energy goes to zero; but the valence and conduction band touch each other at the K and K' points. Setting $E(k_x, k_y) = 0$ one can locate the six coordinate pairs $(k_x a, k_y a)$; they are listed in table 2.1.

	$(k_x a, k_y a)$	$(k_x a, k_y a)$	$(k_x a, k_y a)$
group 1	$\left(0, -\frac{4\pi}{3}\right)$	$\left(\frac{2\pi}{\sqrt{3}}, \frac{\pi}{3}\right)$	$\left(-\frac{2\pi}{\sqrt{3}}, \frac{\pi}{3}\right)$
group 2	$\left(0, +\frac{4\pi}{3}\right)$	$\left(\frac{2\pi}{\sqrt{3}}, -\frac{\pi}{3}\right)$	$\left(-\frac{2\pi}{\sqrt{3}}, -\frac{\pi}{3}\right)$

Table 2.1: Solutions $E(k_x, k_y) = 0$ of the graphene dispersion relation $E(k_x, k_y)$, only two of six points are independent in the graphene lattice, see text. The six points are marked in figure 2.2(b).

2.2 Carbon nanotube band structure

The carbon nanotube band structure can be approximated using the so-called zone-folding technique. The wave function along the carbon nanotube circumference has to fulfill a 2π periodicity, requiring

$$\vec{k} \cdot \vec{C}_h = k_x a \frac{\sqrt{3}}{2} (n + m) + k_y \frac{a}{2} (n - m) = 2\pi q \tag{2.8}$$

for the wave vector $\vec{k}$ with an integer q. The one-dimensional sub-bands are separated in momentum space by

$$\Delta k_\perp = \frac{2\pi}{\left|\vec{C}_h\right|}. \tag{2.9}$$

Note that the wave vectors $k_\parallel$ along the carbon nanotube axis remain continuous. One can see that the two-dimensional band structure of graphene this way collapses to one dimensional sub-bands.

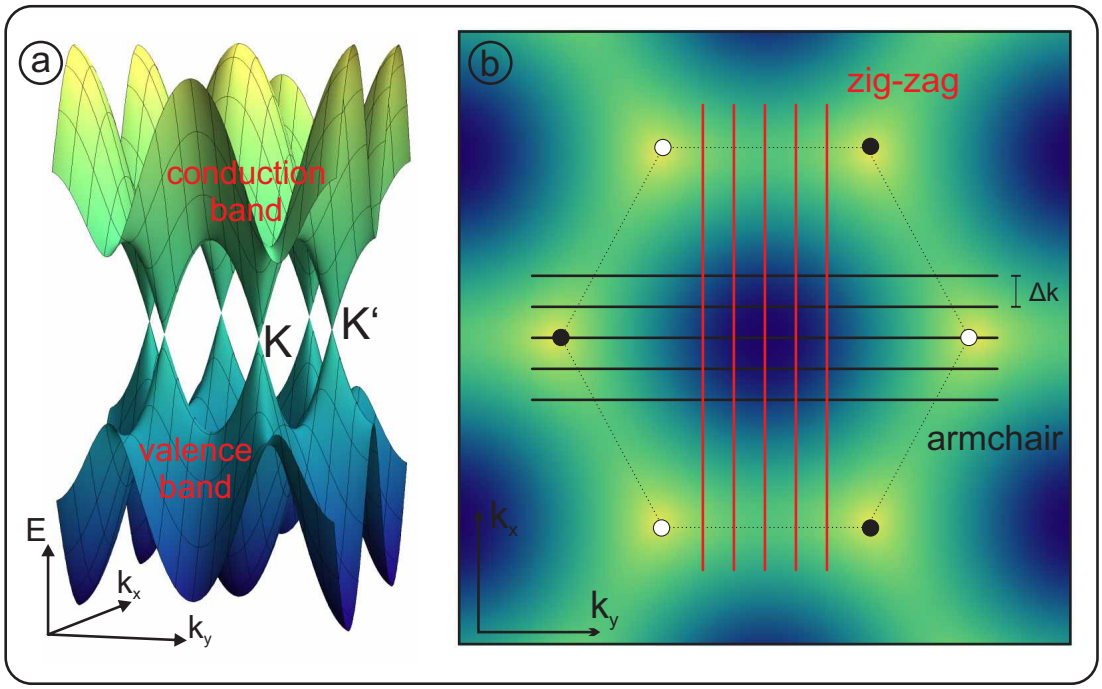

Figure 2.2: (a) Band structure of graphene, following equation 2.7. The valence and conduction band touch each other at six points, the so-called K and K' points. The dispersion relation becomes linear near the K and K' points. (b) Plot of the graphene dispersion relation $E(k_x, k_y)$ in the $\vec{k}_x - \vec{k}_y$−plane; K and K' points are marked with black and white dots. Solid lines depict the one-dimensional dispersion lines for zig-zag (red) and armchair (black) carbon nanotubes spaced by Δk, see text.

As mentioned already above in the zone-folding approximation a carbon nanotube is metallic if the one-dimensional sub-bands intersect one of the K or K' points located at $(k_x a, k_y a) = \left(0, \pm\frac{4\pi}{3}\right)$. Using equation 2.8 a carbon nanotube intersects the valleys for

$$0 \cdot (m+n) \pm \frac{4\pi}{3} \cdot \frac{1}{2}(m-n) = 2\pi q. \tag{2.10}$$

Since q is an integer, this is fulfilled for $(n-m) = 3q$. Thus, every third carbon nanotube would be expected to show metallic behavior.

Armchair type

Armchair carbon nanotubes are rolled up in $\vec{x}$-direction; so $\vec{k}_x$ corresponds to $\vec{k}_\perp$ and $\vec{k}_y$ corresponds to $\vec{k}_\parallel$. The quantization of $\vec{k}_\perp$ is given by

$$\sqrt{3}nak_{\perp} = 2\pi q. \tag{2.11}$$

Accordingly one obtains a spacing of the sub-bands in $\vec{k}_{\perp}$-direction as

$$k_{\perp} = \frac{2\pi q}{\sqrt{3}na}. \tag{2.12}$$

This situation is sketched in figure 2.2(b). One can see that the sub-band for $q = 0$ will always intersect the points $(k_x a, k_y a) = \left(0, \pm\frac{4\pi}{3}\right)$; so armchair carbon nanotubes are always metallic.
Using the dispersion relation of graphene the resulting one-dimensional dispersion relation in $\vec{k}_y$-direction for an armchair carbon nanotube reads

$$E(k_x, k_y) = \pm\left\{1 + 4\cos\left(\frac{\pi q}{n}\right)\cos\left(\frac{k_y a}{2}\right) + 4\cos^2\left(\frac{k_y a}{2}\right)\right\}^{1/2}. \tag{2.13}$$

In figure 2.3(a) and (b) the band structure of a (2,2) carbon nanotube and of a (7,7) carbon nanotube are depicted; no band gap exists and the carbon nanotube has metallic behavior like expected for armchair carbon nanotubes.

Zigzag type

In a zigzag type carbon nanotube the quantization is given by

$$nak_{\perp} = 2\pi q \Rightarrow k_{\perp} = \frac{2\pi q}{na} \tag{2.14}$$

and the band structure reads as

$$E(k_x, k_y) = \pm\left\{1 + 4\cos\left(\frac{\sqrt{3}k_x a}{2}\right)\cos\left(\frac{\pi q}{n}\right) + 4\cos^2\left(\frac{\pi q}{n}\right)\right\}^{1/2}. \tag{2.15}$$

Figure 2.3(c) shows an exemplary (5,0) zig-zag carbon nanotube; as mentioned above a (5,0) zigzag carbon nanotube has a band gap since $(n - m) = 5 \neq 3q$ for an integer q. This can also be seen in the calculated band structure using equation 2.15; a band gap arises. In figure 2.3(d) the band structure of a (6,0) zig-zag carbon nanotube is depicted also using equation 2.15. Now the condition $(n - m) = 6 = 3q$ is fulfilled for $q = 2$, the carbon nanotube is metallic, and no band gap exists.

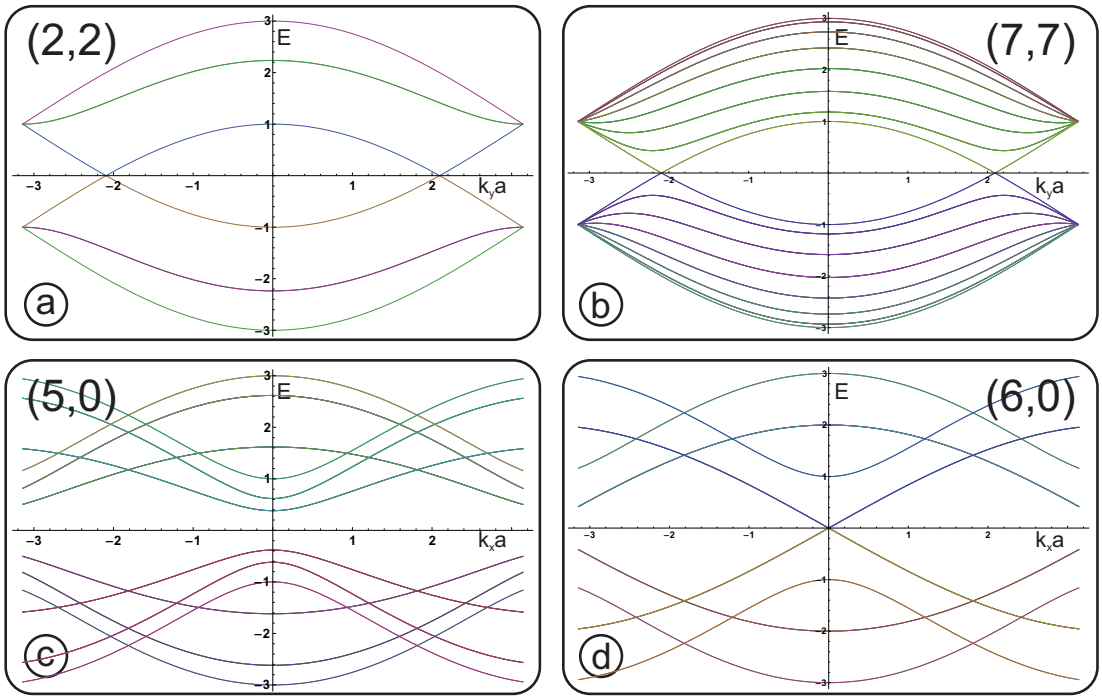

Figure 2.3: Shown are the low-energy band structures of four different carbon nanotubes, following the zone-folding approximation. The figures (a) and (b) depict armchair carbon nanotubes (2,2) and (7,7); both have no band gap and show metallic behavior. (c) depicts a (5,0) zig-zag carbon nanotube; a band gap arises. A (6,0) zig-zag carbon nanotube (d) shows a metallic behavior within zone-folding approximation.

Limits of the zone-folding approximation

The zone-folding approximation used so far for the calculation of the band structure for armchair and zig-zag carbon nanotubes does not account for effects arising due to the curvature of the carbon nanotube; for instance a nearly absent spin-orbit coupling in graphene is significantly enhanced in carbon nanotubes. The curvature is also responsible for the fact that only armchair carbon nanotubes are truly metallic; in all other types being metallic in zone-folding approximation a small band gap arises, giving these carbon nanotubes the name small band gap carbon nanotubes.

CHAPTER 3

Fabrication and measurement techniques for carbon nanotube devices

Many different methods for growing carbon nanotubes are known in literature. One common way is chemical vapor deposition (CVD); this method is employed for the carbon nanotube growth in this thesis. The CVD growth process was optimized for clean and single-walled carbon nanotubes [Kong et al., 1998]. For fabrication of the devices discussed here, the carbon nanotube growth is shifted to the very last step in fabrication processing. This leads to defect-free carbon nanotubes since no contaminations and defects occur due to further fabrication steps [Cao et al., 2005].
Fundamental techniques necessary for the sample fabrication are explained in this chapter. The detailed processing parameters can be found in appendix A.1. For the measurements shown in chapter 4, 5, 6 and 8 a dilution system is employed for cooling; in the end of this chapter a brief overview of the cooling mechanism is presented.
Two slightly different electrode geometries for our device fabrication are used within this thesis, also using different contact materials. Suitable metals have to be chosen since the contact material has to survive the growth conditions of 850° C and hydrogen/methane atmosphere. In the beginning we used rhenium (Re) as contact material; as a second contact material an alloy of rhenium and molybdenum (ReMo) was employed.
Figure 3.1 shows the processing sequence for both device types. As substrate material a highly p-doped silicon wafer is used with a 500 nm thick silicon dioxide layer on top.

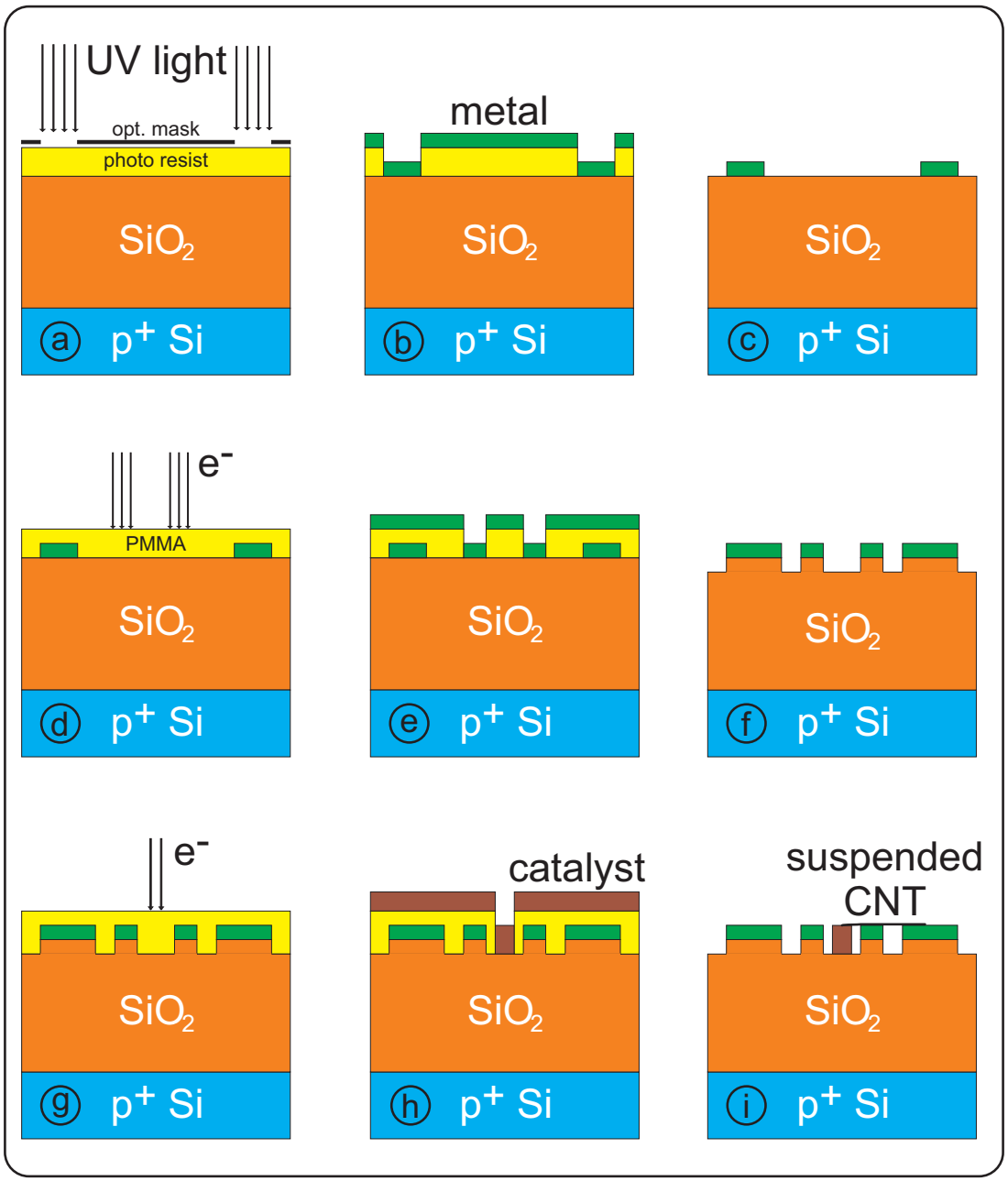

Figure 3.1: Fabrication sequence for suspended carbon nanotube devices. Optical lithography is done for bond pads structures (a). After metallization (b) and lift-off (c) a PMMA resist is brought onto the chip and illuminated using a scanning electron microscope (d). A further metallization and lift-off process is necessary (e) and reactive ion etching deepens the trenches subsequently (f). Local deposition of the catalyst is achieved by EBL (g). Finally the catalyst solution is dropped onto the chip (h) and carbon nanotubes are grown in a CVD process (i). Adapted from [Stiller, 2011].

3.1 Fundamental nanofabrication techniques

Optical lithography

Optical lithography is a standard clean room fabrication technique. It is used for fast processing of rather large structures. A photosensitive resist is spin-coated onto a substrate chip. Afterwards the chip is baked out on a hot plate. The structures are defined on a glass mask coated with a fine chromium layer. In a mask aligner system used for illumination, the position of the chip can be adjusted and finally controlled by an optical microscope. The whole chip can be exposed within one fabrication step.
For the devices discussed here the bond pads and labels are patterned by optical lithography. The fine inner structures are defined via electron beam lithography (EBL) since they are too small for optical lithography. Scanning electron microscope (SEM) pictures of the devices are shown in chapter 3.2, see e.g. figures 3.4 and 3.5.

Electron beam lithography

To achieve a higher resolution electron beam lithography (EBL) is employed. A PMMA (Polymethylmethacrylat) resist is spin-coated onto the chip. The accelerated electron beam cracks the long-chained PMMA molecules; the exposed resist is dissolved during development.

Electrode material

Since the electrode material should stay conductive and not melt during the carbon nanotube growth, special requirements are necessary for the used material. In this thesis rhenium (Re) and rhenium/molybdenum alloys (ReMo) are employed; both materials survive the carbon nanotube growth. For ReMo we use a ratio of 75% rhenium to 25% molybdenum. Re is sputtered in an UHV chamber using an argon plasma; ReMo is co-sputtered by simultaneously driving two sputter sources. The ratio of both materials is varied by the applied power. Both layers are adjusted to a thickness of 40 nm.

Reactive ion etching

To ensure freely suspended carbon nanotubes the trenches between the metallic electrodes are deepened to about 220 nm by reactive ion etching. The metal electrodes serve as etch mask. For selective etching of the silicon dioxide trifluormethane (CHF_3) is used. Argon is employed for a general cleaning step.

Chemical vapor deposition

In preparation for the carbon nanotube grown by chemical vapor deposition (CVD), a catalyst suspension is drop-cast onto the substrate with an EBL patterned resist followed by a lift-off procedure. Afterwards the chip is placed into a glass tube and centered in the CVD oven; after heating it up to about 850° C the gas flow through the quartz tube is adjusted by mass flow controller. Figure 3.2 shows a sketch of the used CVD system. Methane gas is used for the growth; it is cracked by the catalyst particles and provides the carbon feedstock for the carbon nanotubes. A crucial point for the CVD growth is the leakproofness of the gas handling system; small amounts of oxygen can already burn the carbon nanotubes. Different improvements were done during this thesis. Following [Jin et al., 2007] electronic gas flow controllers were installed. Only the latter samples consisting of ReMo contact electrodes were grown using a low, regulated gas flow; details about the growth recipe are listed in appendix A.1. In figure 3.3 SEM pictures of different test devices for overgrown carbon nanotubes are depicted.

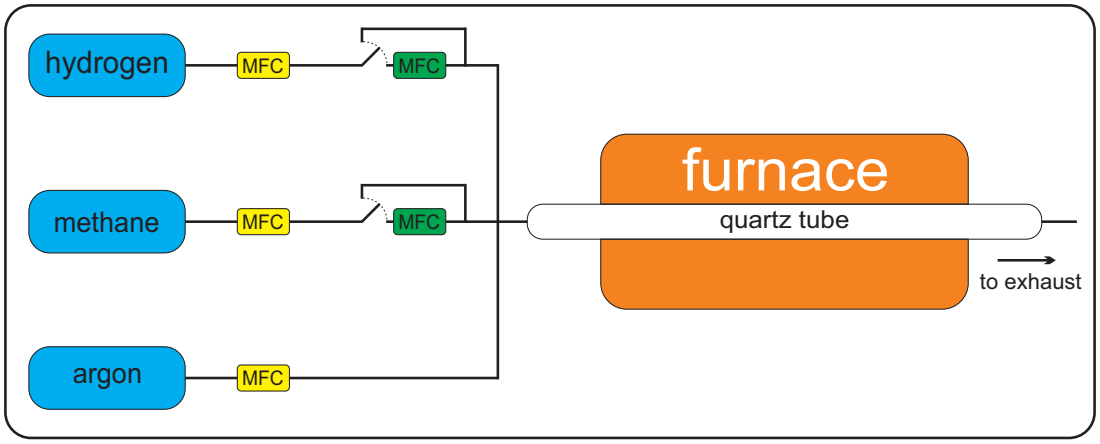

Figure 3.2: Sketch of the CVD growth setup used in Regensburg. For high and low gas flow different mass flow controller are installed. The gas lines are connected to a quartz tube. MFCs (Yellow) are used for high gas flow and green ones for low gas flow.

3.2 Electrode geometry for the carbon nanotube overgrowth

As mentioned earlier two different sets of device geometries and electrode materials are used within this thesis. The device names are derived from the electrode material.

Re sample

The first type of devices uses Re metallized electrodes. The electrode structure is arranged circular around the catalyst material to improve the chance for an overgrowth, see figure 3.4. The trenches between the metallic electrodes for a possible overgrowth of a carbon nanotube are deepened by reactive ion etching, ensuring freely suspended carbon nanotubes. The trench width ranges from 300 nm to 800 nm. Each contact ring has its own bond pad fabricated by optical lithography. To ease lift-off of the innermost circular structures, the right side of the three circular structures was opened; this region is marked in figure 3.4.

ReMo sample

For later integration of carbon nanotubes into coplanar waveguide devices we intend to use a gate finger, since substrates with a conductive back gate are not suitable for high frequency applications due to the high signal damping; for the details see chapter 8. The electrode geometry is changed to a triangular structure making the gate finger implementation easier compared to the circular structure of the Re sample. Figure 3.5 shows SEM pictures of the device geometry. Three sets of electrodes and gate fingers are arranged around the catalyst material. The trenches have a width of 500 nm and are deepened to about 220 nm. Bond pads are again deposited using optical lithography; inner structures in a first EBL step. After reactive ion etching deepening of the trenches the gate fingers and their corresponding bond pads are prepared in a second EBL step.

3.3 Room temperature characterization

To avoid contamination suitable devices are only tested by electronic room temperature measurements. For this purpose we employ a probe station with fine needles for contacting the bond pads of the samples, see figure 3.6. A voltage is applied to the source contact and the resulting current is recorded. The gate is used to vary the electro-chemical potential within the carbon nanotube. If a devices is showing a gate dependence of the current it is marked for low temperature measurements (see also chapter 7.4). The chip is then glued into a chip carrier and contacted by aluminum bond wires.

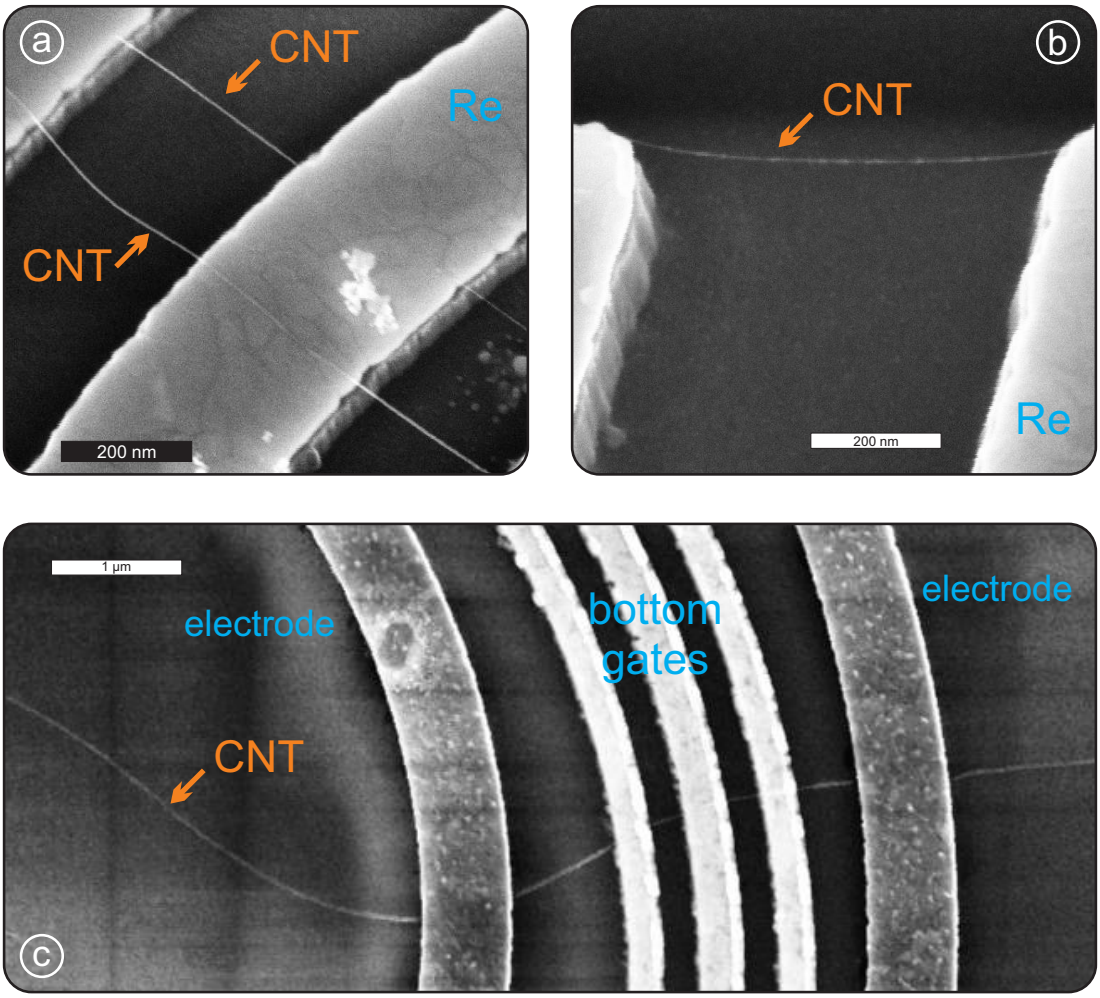

Figure 3.3: SEM pictures of CVD grown carbon nanotube test samples; note that suitable low temperature devices are not imaged using an SEM to avoid contaminations by carbon deposition. (a) and (b) depict carbon nanotubes grown over pre-defined Re contacts. (c) shows a carbon nanotube grown over three gate electrodes isolated by an additional oxide layer.

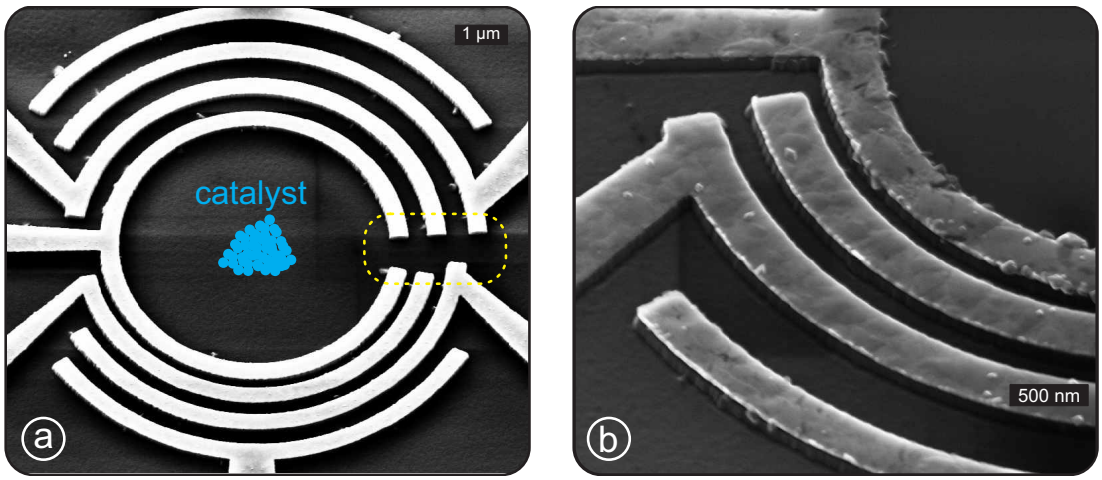

Figure 3.4: Tilted SEM pictures of the circular electrode geometry. Re is used as contact metal; trenches are deepened by RIE. The width of the structures ranges from 300 nm to 800 nm. Catalyst material is deposited in the center of the circular structures (blue area). (b) Detailed view of the circular contacts. The contaminations on the innermost electrode are caused by the CVD growth process.

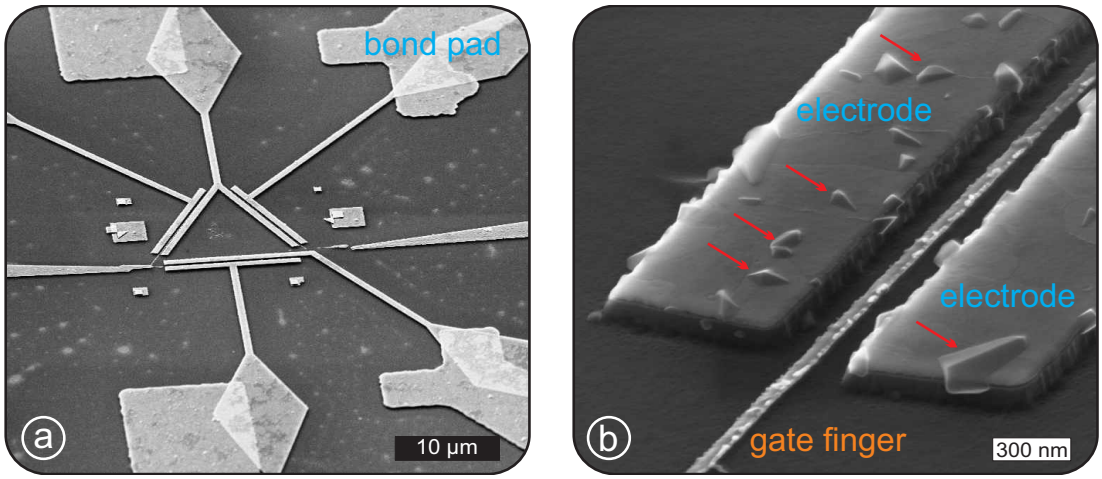

Figure 3.5: (a) Tilted SEM image of the second electrode design using now ReMo contacts. The design is changed to a triangular structure with a gate finger. (b) Enlargement of one gate finger and the corresponding electrodes. Small particles are visible at the ReMo contacts looking like metal pieces lying on-top of the contacts. Unclear is their origin, they might be caused by melting during CVD growth process.

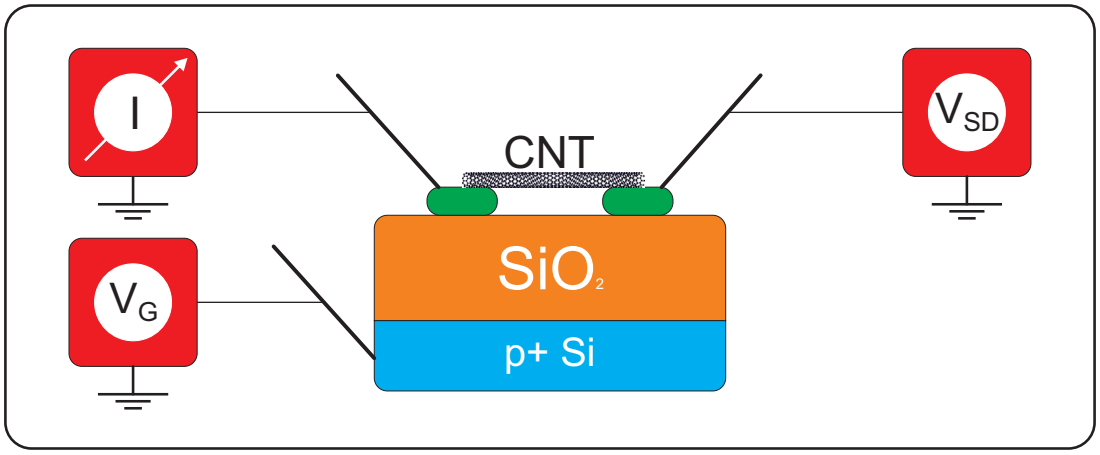

Figure 3.6: Sketch of the device pre-characterization using the room temperature probe station. Fine needles contact the bond pads of the electrode material. The gate is contacted at the edge of the substrate chip. Adapted from [Stiller, 2011].

3.4 The dilution refrigerator

The measurements presented in chapter 4, 5, 6 and 8 require a dilution refrigerator. Two different cooling setups were used. For the measurements of chapter 4, 5 and 6 a top-loading system is employed, reaching a nominal base temperature of 25 mK (the sample is surrounded by liquid helium of the mixing chamber). For the measurements presented in chapter 8 a dilution refrigerator system is optimized for microwave experiments, reaching a base temperature of 7 mK without cabling. In the following the general working principles are summarized. Below 880 mK two liquid phases arise in a mixture of liquid ^{3}He and ^{4}He. A ^{3}He poor phase (diluted phase) is found at the bottom of the mixing chamber, containing 6.6 % of ^{3}He solved in superfluid ^{4}He. The second phase on top of is a more or less pure ^{3}He phase (concentrated phase). Removing ^{3}He from the diluted phase leads to a diffusion of ^{3}He from the concentrated phase into the diluted phase, such that the amount of ^{3}He in the diluted phase is constant. This diffusion in analogy to ^{3}He "evaporating" into the superfluid ^{4}He "vacuum", requires entropy which is taken from the environment, leading to cooling. Refilling ^{3}He into the concentrated phase yields a continuous cooling cycle. Figure 3.7 shows a detailed sketch of the ^{3}He/^{4}He circulation in a dilution system; for more details it is referred to [Enss and Hunklinger, 2005, Pobell, 2007].

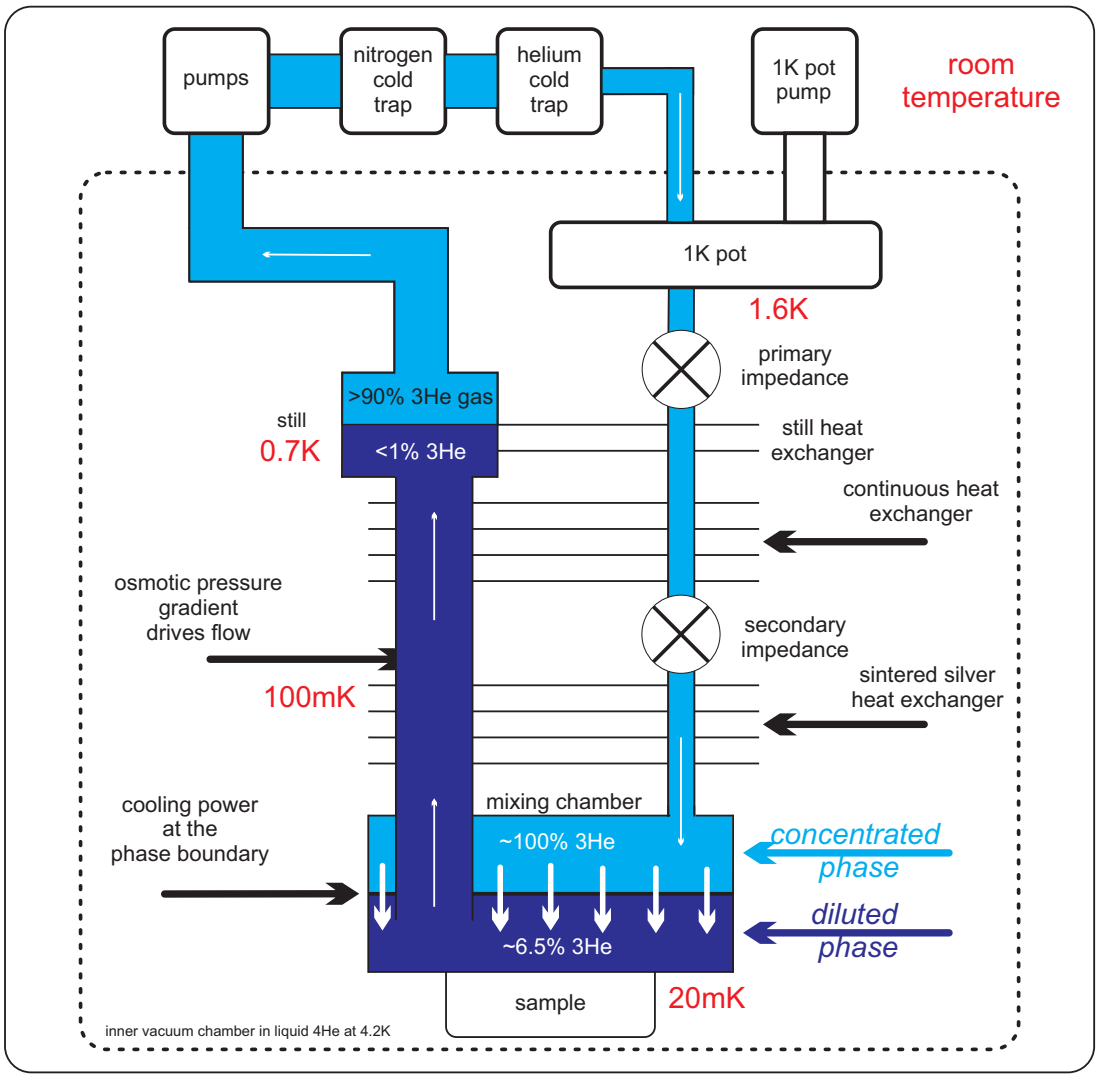

Figure 3.7: Functionality of a dilution refrigerator: Circulation of the ^{4}He and ^{3}He mixture. In the mixing chamber two phases arise; the interplay is responsible for cooling to the mK-regime. All lines and necessary facilities are depicted. Redrawn following [Craig and Lester, 2004].

CHAPTER 4

Electronic transport through carbon nanotube quantum dots

The fundamental electronic properties of carbon nanotubes were already presented in chapter 2. The typically ballistic nature of electronic transport through a carbon nanotube is due to a mean free path of the traveling electrons which is longer than the size of the carbon nanotube [White and Todorov, 1998, Javey et al., 2003]; it can reach several micrometers [Purewal et al., 2007]. In the Landauer-Büttiker formalism it turns out that each available spin degenerate transport sub-band contributes an universal conductance value [Datta, 1995]

$$G = 2 \cdot \frac{e^2}{h}. \tag{4.1}$$

In a defect-free carbon nanotube, the valleys K and K' in combination with spin-up and spin-down lead to four transport channels and thereby a maximal conductance of $G_{\mathrm{CNT}} = 2 \cdot G$, i.e., a minimal resistance of $R_{\mathrm{CNT}} \approx 6.5\,\mathrm{k\Omega}$. Note that this is the case of ideally transmitting one-dimensional channels. In the case of, e.g., tunnel barriers between leads and carbon nanotube higher device resistance are to be expected. Confining the electronic system further one obtains a zero-dimensional quantum dot system. This chapter gives a theoretical description of quantum transport through carbon nanotube quantum dots; in addition, an overview of the electronic characterization of one employed device is given. The device consists of a small band gap carbon nanotube lying over a 700 nm wide trench of a Re type sample structure (compare chapter 3). The carbon nanotube has a room temperature resistance of approximately 10 kΩ. The measurements on this device presented here and in chapter 5 and 6 were performed in cooperation with Daniel Schmid; additional data have already been published in [Stiller, 2011, Schmid, 2014, Schmid et al., 2015a].

4.1 Quantum dots

In general, a quantum dot is a small conducting island, placed in an otherwise isolating material. It is confined in all three spatial dimensions and is coupled by tunnel barriers to reservoirs typically named source and drain. In figure 4.1 a schematic drawing of such a system is depicted. A gate electrode is capacitively coupled to the quantum dot to tune its electro-chemical potential. More complex gate electrode structures are possible to define double [Pothier et al., 1992, van der Wiel et al., 2002] or even triple quantum dots [Gaudreau et al., 2012] in various systems. Also carbon nanotube single [Tans et al., 1997, Jarillo-Herrero et al., 2004] and double quantum dots [Biercuk et al., 2005, Sapmaz et al., 2006b, Jung et al., 2013] were already presented.
The transport through a quantum dot depends on the relevant energy scales. The charging energy E_C is the necessary energy to add an additional charge carrier to the quantum dot. If the thermal energy of the electrons k_BT is much higher than the charging energy ($E_C << k_BT$) the transport through the quantum dot behaves classically, i.e. no quantization effects will be seen. At low temperature classical and quantum Coulomb blockade can be observed. Here only a brief overview is given, for details it is referred to [van Houten et al., 1992, Kouwenhoven et al., 1997].

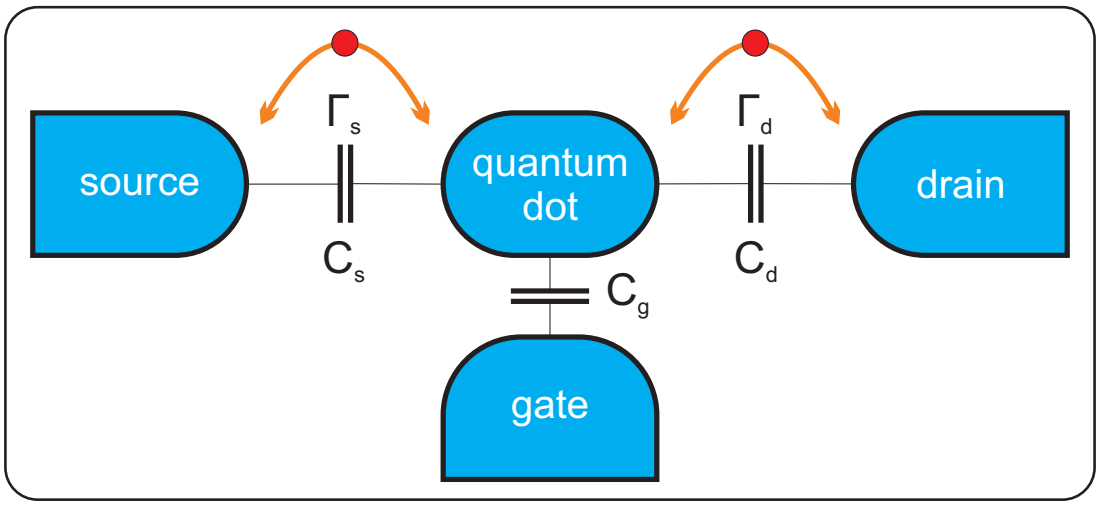

Figure 4.1: A quantum dot can be seen as a small conducting island. It is coupled to two reservoirs. Charge carriers can be exchanged via tunnel barriers Γ_s and Γ_d. A gate electrode is coupled capacitively to the quantum dot to tune the electro-chemical potential of the quantum dot.

Classical Coulomb blockade

Classical Coulomb blockade is observed if the thermal energy of the electrons k_BT is much smaller than the charging energy E_C; the charging energy depends on the size of the quantum dot and is typically in the range of meV. At liquid helium temperatures (4 K), the thermal energy of the electrons is $k_BT \approx 0.34\,\text{meV}$. This is the first requirement to observe classical Coulomb blockade. Additionally the tunnel resistance has to be high enough that the charge carrier number on the quantum dot is well defined. Using the Heisenberg uncertainty relation it turns out that the tunnel resistance must exceed the resistance quantum h/e^2. When these two requirements are fulfilled, the current through the quantum dot can be electrostatically suppressed by Coulomb blockade and the number of charge carriers on the quantum dot is fixed.
Current flow through the quantum dot means: The charge carrier number on the quantum dot is fluctuating at least by one. The electro-chemical potential of the quantum dot

$$\mu(N) = E_N - E_{N-1}, \tag{4.2}$$

is defined as the difference of the ground state energies E_i for N and $N-1$ charge carriers on the quantum dot. Electronic transport through the quantum dot is allowed, if the electro-chemical potential of the quantum dot $\mu(N)$ is aligned to the electro-chemical potentials of source μ_s and drain leads μ_d (until now we assume $V_{\text{bias}} = 0$ and thus $\mu_s = \mu_d$):

$$\mu(N) = \mu_s = \mu_d. \tag{4.3}$$

In figure 4.2(a) the electro-chemical potentials $\mu(N)$ and μ_s, μ_d are not aligned and the transport through the quantum dot via first-order tunneling processes is blocked; the charge carrier number on the quantum dot is fixed. The electro-chemical potential of the quantum dot can be tuned by a gate electrode, so the ladder of energy states is shifted. In figure 4.2(b) the condition $\mu(N) = \mu_s = \mu_d$ is fulfilled by a shift of the electro-chemical potential $\mu(N)$ due to the applied gate voltage; the charge carrier number can now fluctuate by one.

Quantum Coulomb blockade

Until now, the confinement of charge carriers within the quantum dot was neglected. A metallic quantum dot has a large, continuous density of states n_s and so a small Fermi wavelength

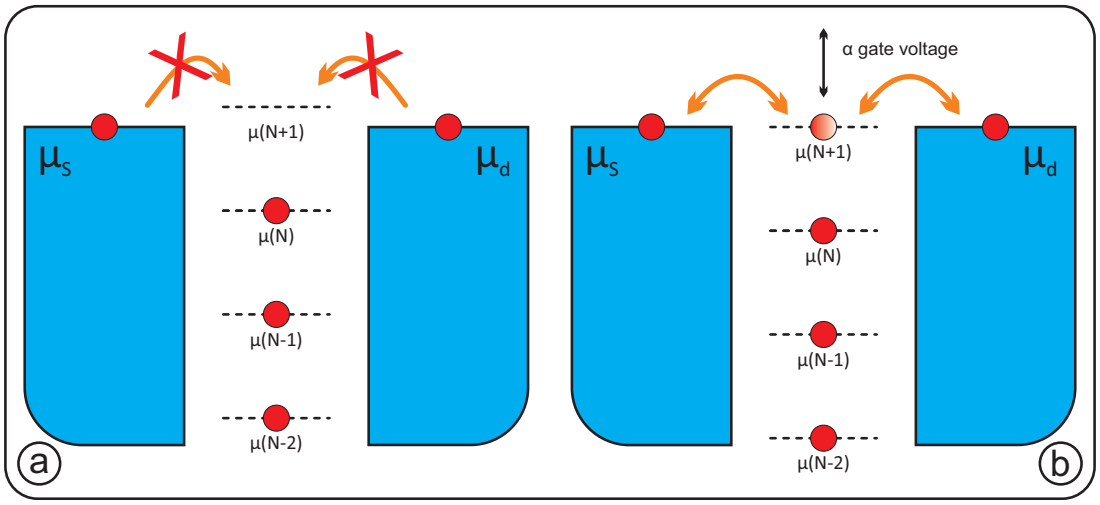

Figure 4.2: Quantization of electric charge in a zero-dimensional quantum dot system leads to a discrete ladder of quantum dot charging states. In (a) the current through the quantum dot is suppressed; no energy level $\mu(N)$ is aligned with the reservoirs. The energy ladder can be tuned by a capacitively coupled gate electrode (b). Now electronic transport is allowed and the charge carrier number is fluctuating by one.

$$\lambda_F = \sqrt{\frac{2\pi}{n_s}}, \tag{4.4}$$

which is typically much smaller than the size of the quantum dot. In semiconducting quantum dots, however, the Fermi wavelength is in the order of the quantum dot size due to the reduced, discrete density of states. This leads to the fact that the energy spacing $\Delta\epsilon$ between the quantum states induced by the quantum confinement of charge carriers is on the order of the charging energy E_C and has to be taken into account.
The energy splitting $\Delta\epsilon$ is typically in the range of 0.1 meV to 5 meV for semiconducting quantum dots. Common dilution refrigerators reach electron temperatures around 100 mK, this leads to a thermal energy $k_BT \approx 8.6\,\mu$eV. In this temperature range the thermal energy is much smaller than the energy splitting $\Delta\epsilon$ ($k_BT << \Delta\epsilon << E_C$). Within the constant interaction model [Kouwenhoven et al., 1997] the energy difference ΔE reads:

$$\Delta E = E_c + \Delta\epsilon, \tag{4.5}$$

it depends on the one hand the classical charging energy E_c and on the other hand the level spacing $\Delta\epsilon$ induced by the charge carrier quantum confinement.

The charging energy reads [Kouwenhoven et al., 1991]

$$E_C = \frac{e^2}{2C_\Sigma}, \tag{4.6}$$

where

$$C_\Sigma = C_{\text{source}} + C_{\text{drain}} + C_{\text{gate}}, \tag{4.7}$$

is the total capacitance of the quantum dot. The capacitance C_Σ is assumed to be independent of the occupation of the quantum dot. Coulomb interaction of the quantum dot electrons and the interaction of the quantum dot electrons with those of the leads and gates are parametrized in capacitances. Within the constant interaction model, the classical charging energy E_C is approximated as constant.

4.2 Carbon nanotube quantum dots

Quantum dots can easily be formed in semiconducting carbon nanotubes. In our carbon nanotube devices the quantum dot is defined on the suspended part of the carbon nanotube. The low temperature measurements of the employed carbon nanotube devices used in this thesis show both a highly transparent transport regime for negative gate voltages and Coulomb blockade transport regime for positive gate voltages, separated by a small band gap. The measurements will be shown later in this chapter and in chapter 7. This indicates that both carbon nanotubes are "p-doped" semiconductors. The electronic properties of a carbon nanotube device depend dramatically on the arising band deformation at the interface [Tans et al., 1998, Svensson and Campbell, 2011]. Figure 4.3 sketches the band deformation and the influence of an applied gate voltage. For a negative gate voltage the valence and conductance bands are shifted upwards. Between the semiconducting carbon nanotube and the metallic leads a weak Schottky barrier arise at the interfaces (not shown in figure 4.3). The resulting tunnel barriers are rather narrow and high conductance values are expected, which can approach the theoretical limit of $4e^2/h$. In figure 4.3 the Fermi energy lies below the valence band since transport is observed in our devices for zero gate voltage.
In the case of a positive gate voltage the bands are shifted downwards yielding broader tunnel barriers and single electron transport can typically be observed in such devices due to arising pn-junctions within the carbon nanotube.

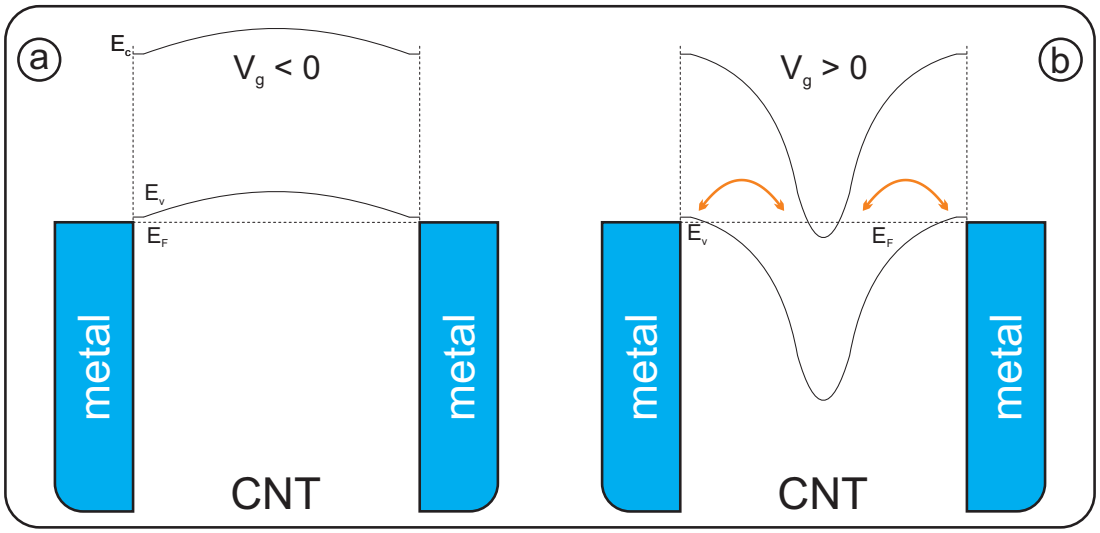

Figure 4.3: Drawn is a sketch of a metal - "p-doped" carbon nanotube - metal transition. The Fermi energy E_F of the carbon nanotube lies below the valence band in our devices. In (a) a negative gate voltage is applied to the carbon nanotube resulting in an upwards shift of valence and conduction band. For a positive gate voltage the bands are bent downwards, pn-junctions arises on both interfaces (b).

4.3 Quantum dot transport spectroscopy

In the previous section, the bias voltage V_{bias} was set to zero. Sharp peaks of the differential conductance as a function of the gate voltage V_{gate} are expected, whenever an energy "level" $\mu(N)$ is in resonance with source and drain reservoirs, as sketched in figure 4.4(a).
For a metallic quantum dot the spacing between the peaks would be equidistant since E_C is constant. Semiconducting quantum dots give rise to a more complex structure since the level spacing $\Delta\epsilon$ induced by the quantum confinement must be taken into account; as discussed before the energy splitting ΔE is not constant anymore and thus the conductance peaks observed by varying the gate voltage are not equidistant but depend on E_C and $\Delta\epsilon$.
Applying now a finite bias voltage

$$V_{\text{bias}} = \frac{\mu_d - \mu_s}{|e|}, \tag{4.8}$$

the width of the transport region increases due to the misalignment between source and drain reservoirs, see figure 4.4(b). Electronic transport through the quantum dot is now allowed for (assuming $\mu_s > \mu_d$)

$$\mu_s \geq \mu(N) \geq \mu_d. \tag{4.9}$$

The transport range increases for further increasing bias voltage V_{bias}; at a certain bias voltage V_{bias} two charging states lie within the opened transport window (figure 4.4(c)). Now the charge carrier number is fluctuating by two.
Varying both the gate voltage V_{gate} and the bias voltage V_{bias} a two-dimensional plot of the conductance arises as sketched in figure 4.4(e). A diamond shaped region with fixed charge carrier number is visible, also called Coulomb blockade diamond. If enough energy is provided (see equation 4.2) for excited charging states $\mu^*(N)$ additional transport channels within the bias window are opened. The charge carrier number is still fluctuating by one but the charge carrier can enter the charging states $\mu^*(N)$ instead of $\mu(N)$. Excited charging states $\mu^*(N)$ are visible as additional lines in the conductance as a function of both gate voltage and bias voltage, they start at the Coulomb blockade diamond with N confined charge carriers and run parallel to edge of the Coulomb diamond with $N-1$ charge carriers, see the red lines in figure 4.4(e).
In figure 4.5(a) a measurement of the current through the carbon nanotube as function of the gate voltage V_{gate} is depicted. A small bias voltage $V_{\text{bias}} = 50\,\mu\text{V}$ is applied to the source contact, the gate voltage V_{gate} is varied from 0 V to 5 V. On the electron conduction side ($V_{\text{gate}} > 0.6\,\text{V}$) pronounced Coulomb blockade features arise. For increasing gate voltage the tunnel barriers arising due to the pn-junctions are reduced and thus the current through the device increase. Visible are also higher order processes like the Kondo effect, where the zero-bias conductance is enhanced in every second Coulomb blockade valley [Goldhaber-Gordon et al., 1998]. A single unpaired electron spin on the quantum dot interacts with the electrons of the reservoirs.
The numerical derivative $|\mathrm{d}I/\mathrm{d}V|$ is plotted in figure 4.5(b) and (c) as a function of both gate voltage V_{gate} and bias voltage V_{bias}. In 4.5(b) the transition $N = 0$ to $N = 1$ electrons is depicted. The electron number is counted starting from the band gap using the conductance measurement of figure 4.5(a). One can clearly see the diamond like structure in the conductance measurement and also three additional lines corresponding to excited charging states are visible. The excitation energies are 0.71 meV, 1.50 meV and 1.96 meV; they can be extracted from the intersection of the excited charging state and the edge of the Coulomb diamond. The extracted difference in bias voltage ΔV_{bias} can be converted in energy: $\Delta E = e\Delta V_{\text{bias}}$. The excited charging state correspond to a one-electron excitation since the excitation lines end in the Coulomb diamond with one electron fixed on the quantum dot. If we go from $N = 1$ to $N = 2$ electrons (figure 4.5(c)) again the diamond like structure arises. Clearly visible is a rich spectrum of transport through excited charging states within the bias window.

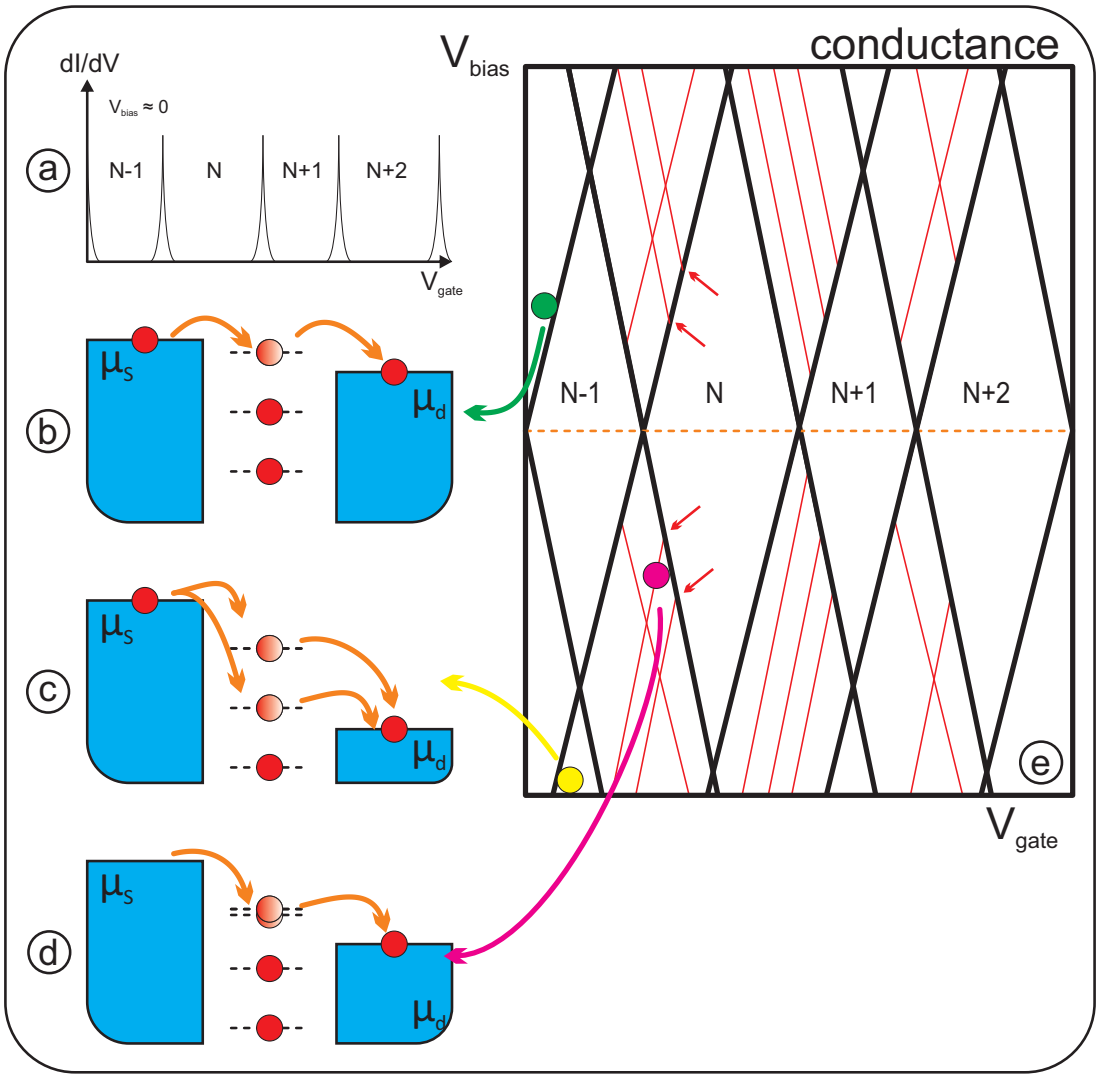

Figure 4.4: Measuring the conductance as a function of the gate voltage one obtains sharp peaks of the conductance whenever a charging state $\mu(N)$ of the quantum dot is aligned to the source and drain reservoirs (a). An applied bias voltage opens a transport gap, the charge carrier number can fluctuate by one (b) or two (c). (d) An excited charging state $\mu^*(N)$ provides an additional transport channel, however, the charge carrier number is still fluctuating by one. In (e) the conductance is plotted as a function of both gate voltage and bias voltage, the arising diamond like shape is called Coulomb blockade diamond. Red lines within the bias window represent excited charging state; the red arrows mark the excited charging state corresponding to an N charge carrier excitation. The orange line corresponds to the line cut for zero bias voltage in (a). The green, yellow, and violet dots mark the situations of (b), (c), and (d).

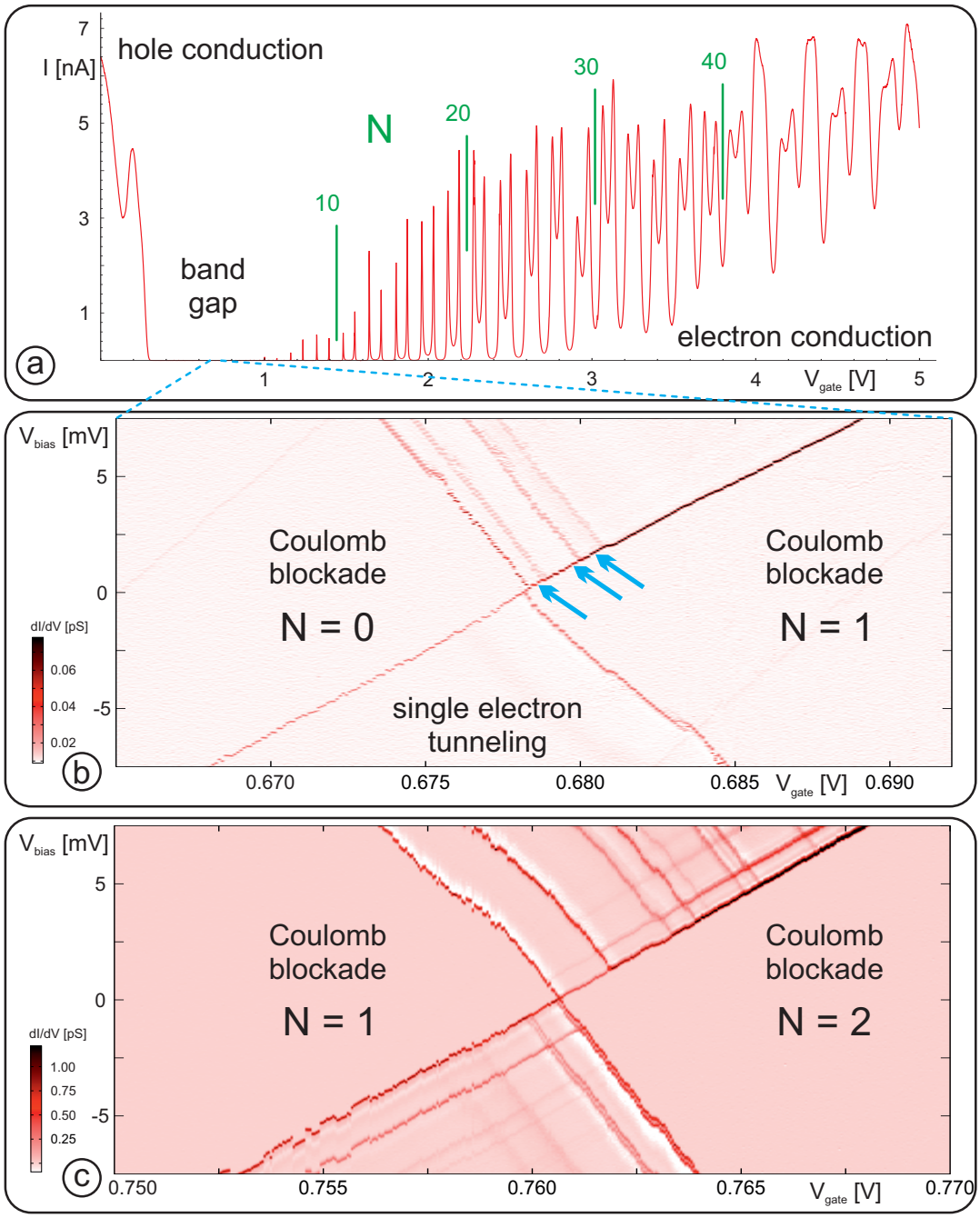

Figure 4.5: (a) Conductance is measured as a function of the gate voltage V_{gate} for a bias voltage $V_{\text{bias}} = -50\,\mu\text{V}$. On the electron conduction side Coulomb blockade arises, the electron number N on the quantum dot is counted starting from the band gap. The conductance as a function of both gate voltage and bias voltage is plotted in (b) and (c). In (b) the transition form $N = 0$ to $N = 1$ electrons is depicted. Several additional excited energy lines are visible in single electron tunneling (cyan arrows). The transition from $N = 1$ to $N = 2$ electrons yields a more complex structure of excited states. Measurement done at 25 mK.

CHAPTER 5

Carbon nanotubes in a parallel magnetic field

The combination of spin and orbital degrees of freedom in carbon nanotubes leads to a four-fold degeneracy of the carbon nanotube single particle spectrum. A finite parallel magnetic field lifts the four-fold degeneracy, which will be described first in this chapter together with the carbon nanotube single particle spectrum.
In [Ajiki and Ando, 1993] it was predicted that the orbital degeneracy is lifted by a finite parallel magnetic field $B_{\parallel}$. Two main effects are responsible for the carbon nanotube single particle spectrum evolving in a parallel magnetic field. Due to the Aharonov-Bohm effect the quantization condition in a carbon nanotube for $k_{\perp}$ is replaced by

$$k_{\perp} \rightarrow k_{\perp} + \frac{\Phi}{r\Phi_0}, \tag{5.1}$$

where Φ/Φ_0 represents the magnetic flux through the carbon nanotube and $\Phi_0 = h/2e$ is the flux quantum. Additionally the Zeeman effect introduces a linear shift in energy depending on the magnetic field; the sign of the slopes is different for spin-up and spin-down.
To obtain a more detailed understanding of the influence on the single particle spectrum of radius, chiral angle, and length of a carbon nanotube in a parallel magnetic field, numerical transmission calculations for carbon nanotubes are performed, working towards the objective of identifying the chirality from electronic measurements. Fundamental techniques for numerical calculations are provided in the text book of [Datta, 1995]. These can be used to obtained the transmission through carbon nanotubes [Nemec, 2007]; in this chapter only a short guideline for the numerical calculations is given. The work of this chapter is done in cooperation with Magdalena Marganska, University of Regensburg.

5.1 Carbon nanotube single particle spectrum

Low magnetic field

In the previous chapter 4 fundamentals of the quantum transport through a carbon nanotube was explained; at low temperature a quantum dot is formed within the carbon nanotube. The measurement in figure 4.5(b) shows a conductance measurement for the transition from $N = 0$ to $N = 1$ electrons. The ground state and three excited states are visible, all two-fold degenerate. We observe the first two shells since each state is double-degenerate as explained below and each shell has four energy states. In absence of electron-electron interaction and with weak tunneling rates to the leads, i.e. low state decay rate, the single particle spectrum can be observed. Low temperatures are necessary since the conductance peak broadening is temperature dependent. The single particle spectroscopy for low parallel magnetic fields was already discussed in [Schmid, 2014]. The spin-orbit coupling Δ_{SO} and the KK' mixing $\Delta_{\mathrm{KK'}}$ have to be taken into account for analytic modeling of the carbon nanotube single particle spectrum. Both lead to a formation of two Kramers doublets, but the nature of the Kramers states is quite different in the two cases [Kuemmeth et al., 2008]. KK' mixing leads to double-degenerate spin states; in contrast spin-orbit coupling breaks the symmetry by coupling orbital and spin degrees of freedom. Recent theoretical calculations showed that the KK' mixing can not only be induced by disorder but splitting also occurs in clean, armchair-like carbon nanotubes due to their finite size and fact that they have the same crystal angular momentum at both valleys [Marganska et al., 2015]. For a finite spin-orbit coupling Δ_{SO} and a finite KK' mixing $\Delta_{\mathrm{KK'}}$ the energy splitting of the two Kramers doublets reads

$$\Delta = \sqrt{\Delta_{\mathrm{SO}}^2 + \Delta_{\mathrm{KK'}}^2}, \tag{5.2}$$

for zero parallel magnetic field.

High magnetic fields

For a high parallel magnetic field the full dispersion relation of a carbon nanotube has to be taken into account [Izumida et al., 2009]:

$$E(\tau, \sigma, B) = \hbar v_F \sqrt{(k_\perp)^2 + \left(k_\parallel\right)^2} + \tau\sigma\epsilon_{\mathrm{SO}} + \sigma\mu_B B, \tag{5.3}$$

where $\sigma = \pm 1$ represents the spin and $\tau = \pm 1$ the valley quantum number.

The momentum $k_\perp$ and the momentum $k_\parallel$ read:

$$k_\perp = k'_\perp + \tau \Delta k_\perp^c + \sigma \Delta k_\perp^{\mathrm{SO}} + \frac{\pi r B}{\Phi_0} \tag{5.4}$$

$$k_\parallel = k'_\parallel + \tau k_\parallel^c, \tag{5.5}$$

the magnetic field shifts the momentum $k_\perp$; the momentum $k_\parallel$ is assumed to be constant for the analytic model.
The shift $\Delta k_\perp^c$ is curvature induced and depends on whether the carbon nanotube is metallic $\Delta k_\perp = \Delta k_\perp^{\mathrm{c}}$ or not $\Delta k_\perp = \Delta k_\perp^{\mathrm{c}} + \frac{\nu}{3r}$, where $\nu = (n-m)|_{\mathrm{mod}\ 3}$ and

$$\Delta k_\perp^{\mathrm{c}} = \frac{a}{r^2}\left(1 + \frac{3}{8}\frac{V_{\mathrm{pp}}^\sigma - V_{\mathrm{pp}}^\pi}{V_{\mathrm{pp}}^\pi}\right)\cos\left(3\Theta\right), \tag{5.6}$$

V_{pp}^σ and V_{pp}^π are defined in appendix C. The curvature induced shift of the momentum $k_\perp$ leads to a small band gap in nominally metallic carbon nanotubes.
The spin-orbit induced shift of the momentum $k_\perp$ reads:

$$\Delta k_\perp^{\mathrm{SO}} = \frac{2\delta}{r}\left(1 + \frac{3}{8}\frac{V_{\mathrm{pp}}^\sigma - V_{\mathrm{pp}}^\pi}{V_{\mathrm{pp}}^\pi}\right), \tag{5.7}$$

where δ is the spin-orbit coupling parameter. A second spin-orbit coupling term $\tau\sigma\epsilon_{\mathrm{SO}}$ is introduced depending on the spin and valley quantum number [Steele et al., 2013]. The full Hamiltonian for a parallel magnetic field including KK' mixing, using $E\left(\tau, \sigma, B\right)$, from equation 5.3, reads:

$$\begin{aligned} H_{\mathrm{full}} = &\begin{pmatrix} E\left(K,\uparrow,B\right) & 0 & 0 & 0 \\ 0 & E\left(K,\downarrow,B\right) & 0 & 0 \\ 0 & 0 & E\left(K',\uparrow,B\right) & 0 \\ 0 & 0 & 0 & E\left(K',\downarrow,B\right) \end{pmatrix} \\ &+ \frac{1}{2}\begin{pmatrix} 0 & 0 & \Delta_{\mathrm{KK'}} & 0 \\ 0 & 0 & 0 & \Delta_{\mathrm{KK'}} \\ \Delta_{\mathrm{KK'}} & 0 & 0 & 0 \\ 0 & \Delta_{\mathrm{KK'}} & 0 & 0 \end{pmatrix} + a_B B \begin{pmatrix} 1 & 0 & 0 & 0 \\ 0 & 1 & 0 & 0 \\ 0 & 0 & 1 & 0 \\ 0 & 0 & 0 & 1 \end{pmatrix}. \end{aligned} \tag{5.8}$$

The second term includes the KK' mixing and the third term includes a phenomenological asymmetry term (details will follow later in this chapter). The energies of non-interacting electrons in a carbon nanotube are obtained by diagonalization of this Hamiltonian.

Influence of a magnetic field

The graphene dispersion relation is linear near the K, K' points, see chapter 2. Carbon nanotube spectra are quantized in $k_\perp$; in direction along the carbon nanotube axis ($k_\parallel$) a hyperbolic dispersion relation arises. The parallel magnetic field changes the quantization conditions (see equation 5.1), this shifts the dispersion relation in $k_\perp$-direction. This is sketched in figure 5.1; for the K' point this leads to an linear increase of the energy as a function of the parallel magnetic field. In the case of the K point first a decrease of the energy is observed, and after going through the K point the energy increases again. This results in a minimum in energy for a high enough magnetic field. The magnetic field value B_{min} corresponds to the crossing point. Due to the doublet formation at zero magnetic field a slightly different values of B_{min} for the two spins (up and down) are observed.

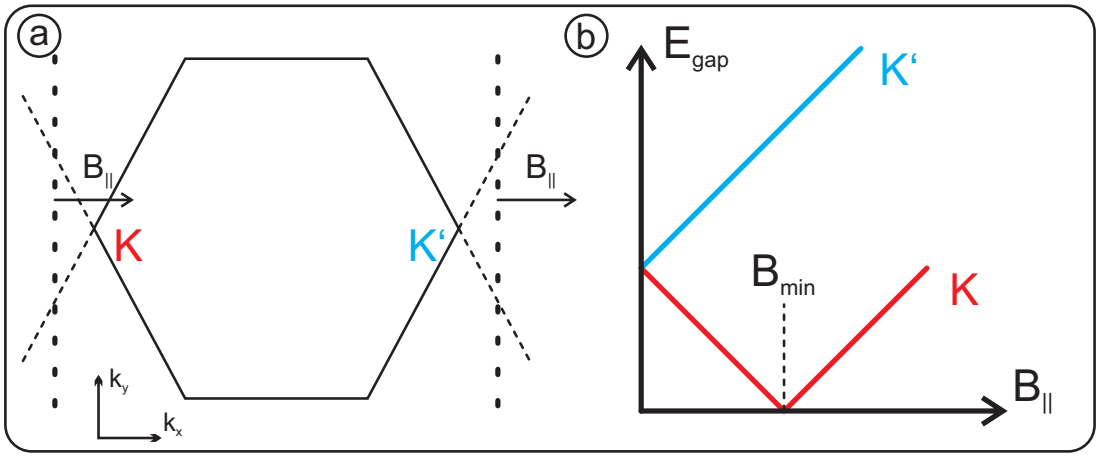

Figure 5.1: Sketched is the dispersion relation near the K and K' point in the $\vec{k}_x - \vec{k}_y$−plane (a). The dotted lines represent the hyperbolic dispersion relation of a carbon nanotube. A parallel magnetic field shifts the momentum, if the dotted lines intersect the $K(K')$ point the energy gap is closed. The corresponding magnetic field is labeled B_{min} (b). Redrawn following [Steele et al., 2013].

Measurement of the carbon nanotube single particle spectrum

Figure 5.2(a) shows the numerically derived conductance plotted as a function of both bias voltage and parallel magnetic field. The bias voltage is varied from $0\,\text{mV} \leq V_{\text{bias}} \leq 15\,\text{mV}$ and the parallel magnetic field from $0\,\text{T} \leq B_\parallel \leq 17\,\text{T}$. The gate voltage is set to $V_{\text{gate}} = 0.675\,\text{V}$, in order to observe the transition $N = 0$ to $N = 1$ electrons (compare figure 4.5(b)). For a magnetic field around $B_\parallel \approx 6\,\text{T}$ a minimum in bias voltage arises. This corresponds to a minimum in energy. Observed is also a decrease of the numerically derived conductance at high magnetic fields above $B_\parallel \approx 10\,\text{T}$.

The peaks of the conductance are extracted and plotted in figure 5.2(b) as a function of the parallel magnetic field. Shown are the four "levels", all belonging to the K valley, exhibiting a minimum in bias voltage. The straight lines represent an analytic fit using the Hamiltonian of equation 5.3. In table 5.1 the used fitting parameters are listed. For a qualitative fit a different momentum $k_{\parallel}$ for both shells is assumed.
In equation 5.8 an asymmetry term was introduced depending on the valley quantum number and on the magnetic field. The physical origin, however, of this term is still unclear but it improves the analytic fit significantly. Two different asymmetry parameter a_B are assumed for shell 1 and shell 2.

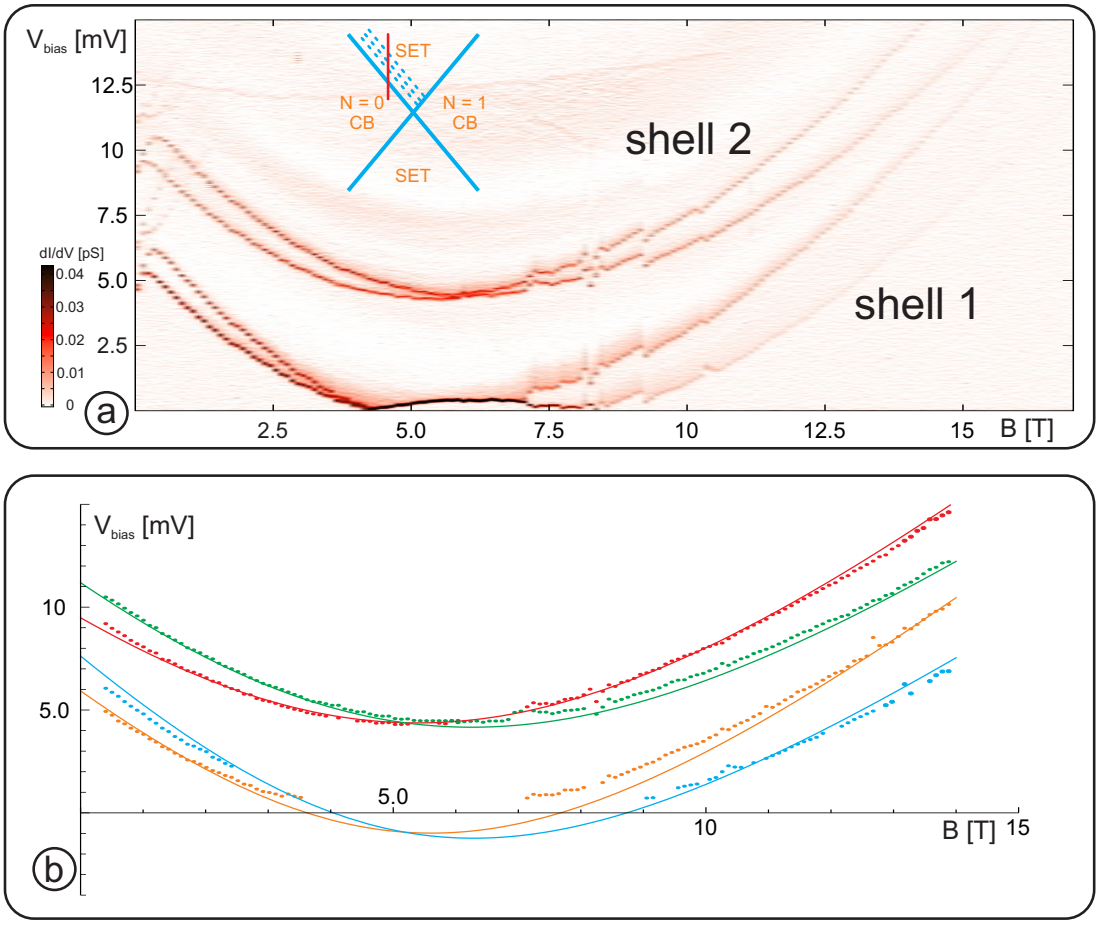

Figure 5.2: (a) Numerically derived conductance is plotted as a function of both bias voltage ($0\,\mathrm{mV} \leq V_{\mathrm{bias}} \leq 15\,\mathrm{mV}$) and parallel magnetic field ($0\,\mathrm{T} \leq B_{\parallel} \leq 17\,\mathrm{T}$). The conductance peaks are extracted and plotted as function of the parallel magnetic field (b). The straight lines represented the analytic fit using equation 5.3 with the asymmetry term added. The cyan cross marks the employed gate voltage.

shell	r [nm]	$\Delta k_\perp^{\mathrm{c}}$ [1/nm]	$\Delta k_\perp^{\mathrm{SO}}$ [1/nm]	ϵ_{SO} [meV]	$k_\parallel$ [1/nm]	a_B [meV]
1	2.2	-0.00845	0.0001	-0.3	0.0095	-0.15
2	2.2	-0.00845	0.0001	-0.3	0.0120	-0.10

Table 5.1: Shown are values used for fitting of the experimental data of figure 5.2(a). For both shells a different momentum $k_\parallel$ and asymmetry a_B is assumed.

5.2 Quantum mechanical transmission

A carbon nanotube electronic device can be seen as a two-terminal device with a Hamiltonian of the form:

$$H = \begin{pmatrix} H_L & H_{LC} & H_{LR} \\ H_{CL} & H_C & H_{CR} \\ H_{RL} & H_{RC} & H_R \end{pmatrix} = \begin{pmatrix} H_L & 0 & 0 \\ 0 & 0 & 0 \\ 0 & 0 & H_R \end{pmatrix} + V = H_o + V, \tag{5.9}$$

where a Hamiltonian H_{ij} links i and j, for example conductor C and right lead R. The operator "V" contains the conductor and its coupling to the environment. Since there is no direct interaction between left and right lead:

$$H_{LR} = H_{RL} = 0. \tag{5.10}$$

The retarded and advanced Greens function are defined as:

$$G^r = (E - H + i\epsilon)^{-1} \tag{5.11}$$
$$G^a = (E - H - i\epsilon)^{-1} \tag{5.12}$$

where ϵ is a small offset energy. With these Green's functions one can define the spectral function of the left and right lead:

$$A_{L/R} = i\left(G^r_{0L/0R} - G^a_{0L/0R}\right), \tag{5.13}$$

where $G_{0R/0L}$ are the Green's functions for the disconnected right/left lead. Since effects occurring due to the direct interaction between the leads are neglected, the transmission can be written as:

$$T(E) = \mathrm{Tr}\left[A_R H_{RC} G^r_C H_{CL} A_L H_{LC} G^a_C H_{CR}\right], \tag{5.14}$$

where $G_C^{r,a}$ are the Green's functions projected to the conductor:

$$G_C^{r,a} = (E - H_C - \Sigma_L^{r,a} - \Sigma_R^{r,a})^{-1}, \tag{5.15}$$

which can be obtained using a decimation technique [Nemec, 2007]. The self energy of the leads read:

$$\Sigma_{L/R}^{r,a} = H_{CL/CR}(E \pm i\epsilon - H_{L/R})^{-1} H_{LC/RC}. \tag{5.16}$$

Using the definition

$$\Gamma_L = H_{CL} A_L H_{LC} = i(\Sigma_L^r - \Sigma_L^a), \tag{5.17}$$

one finally obtains the transmission T(E):

$$T(E) = \mathrm{Tr}\left[\Gamma_R G_C^r \Gamma_L G_C^a\right]. \tag{5.18}$$

The form of these Γ, G objects depends on the employed system.

Carbon nanotube Hamiltonian

The position of each carbon atom within a carbon nanotube is defined by the chiral indices (n, m), which also determine the chiral angle Θ and the radius r of the carbon nanotube. The length of the carbon nanotube is set by the number of unit cells. Using the position of each carbon nanotube atom one can set up a first-nearest neighbor tight-binding Hamiltonian. To obtain the transmission through the carbon nanotube from this Hamiltonian, one has to calculate the Greens function as defined in the previous section. The transition from one carbon atom to the other is described by the hopping integrals, the complete expressions are given in appendix C.

Carbon nanotubes connected to leads

In addition one has to define the coupling of the carbon nanotube to the leads. The transmission though a carbon nanotube depends crucially on its contacts and the size of the contact area. For the calculation done in this chapter the end atoms of the carbon nanotube are connected to the leads. In principle each carbon atom in a carbon nanotube has three neighboring carbon atoms (due to sp^2 hybridization). At both ends of a finite carbon nanotube the last atoms have only two carbon atoms as neighbors, and these are the atoms which are coupled to the contact electrodes.

The coupling between the leads and the carbon nanotube is assumed to be constant; so the self energies read:

$$\Sigma^r_{L/R} = -i\left(\frac{d}{2}\right)\mathbb{1}, \tag{5.19}$$

this also includes a symmetric coupling from left and right lead to the carbon nanotube. These "wide-band" leads include the assumption that the coupling of the leads and the system does not depend on the energy, due to the "wide bands" of the metals compared to the spectrum of the system.
For a carbon nanotube connected to "wide-band" leads one obtains a Breit-Wigner form of the transmission [Breit and Wigner, 1936, del Valle et al., 2011]

$$T(E) = \sum_n \frac{d^2}{(E - E_n)^2 + d^2}. \tag{5.20}$$

Whenever the energy hits the levels E_n a peak in the transmission is observable, if the coupling parameter d is smaller than the spacing of the energy levels E_n. For a too large coupling factor d, the single peaks are smeared out and are not visible anymore in the transmission. For the case of a carbon nanotube the coupling is typically in the range of some meV. The Breit-Wigner form is obtained in general for "wide-band" leads; not only for carbon nanotubes or molecules.

5.3 Transport calculations for different kinds of carbon nanotubes

The chiral indices (n, m) and the number N of the unit cells define the radius r, the length L, and the chiral angle Θ of a carbon nanotube. In figure 5.3 the transmission is depicted as a function of both energy and parallel magnetic field for a $(5, 2)$ carbon nanotube with a radius $r = 0.2445\,\text{nm}$, a length $L = 88.68\,\text{nm}$ $(N = 100)$ and a chiral angle $\Theta = 16.01°$.
In order to observe individual "levels" of the carbon nanotube, the lead coupling parameter is set to $d = 5\,\text{meV}$.
In absence of spin-orbit coupling (figure 5.3(a)) a splitting into two doublets, with a energy spacing $\Delta_{KK'} = 0.08\,\text{meV}$, for zero magnetic field is visible. For a finite spin-orbit coupling $\delta = 0.0008$, the splitting $\Delta = 1.27\,\text{meV}$ is enhanced. The spin-orbit coupling Δ_{SO} and the spin-orbit coupling parameter δ are connected via [Jhang et al., 2010]:

$$\Delta_{\text{SO}} = 2\hbar v_F \left|\Delta k_\perp^{\text{SO}}\right| = 2\hbar v_F \left|\frac{2\delta}{r}\left(1 + \frac{3}{8}\frac{V^\sigma_{\text{pp}} - V^\pi_{\text{pp}}}{V^\pi_{\text{pp}}}\right)\right|. \tag{5.21}$$

For a value $\delta = 0.0008$ we obtain $\Delta_{\mathrm{SO}} \approx 0.93\,\mathrm{meV}$ and $\Delta \approx 0.94\,\mathrm{meV}$. This is in good agreement to the obtained value from the numerical transmission calculation; note that the relation given by equation 5.21 is in principle only correct for infinite long carbon nanotubes.
In figure 5.3(b)-(d) the transmission as a function of both energy and parallel magnetic field for three different values of δ is depicted. As discussed before, a finite parallel magnetic field lifts the degeneracy and four levels are observed. For finite spin-orbit coupling an anti-crossing of the energy levels is visible, marked in figure 5.3. Increasing values of δ shift the anti-crossing to higher values of the magnetic fields due to an increased splitting at zero magnetic field.
For several carbon nanotubes the transmission is calculated as a function of both energy and parallel magnetic field to examine the dependence of B_{min} trying to reproduce our measured carbon nanotube and thus identify its chiral indices. The corresponding transmission calculations are shown in appendix C and the extracted values for B_{min} are listed in table 5.2. The minimum in energy as function of a parallel magnetic field depends on different physical quantities of the carbon nanotube, which will be discussed below.

(n, m)	unit cells	radius r [nm]	length L [nm]	chiral angle Θ	B_{min} [T]
(14,8)	60	0.7549	82.10	21.05	37.39
(14,11)	35	0.8495	107.86	26.04	26.86
(21,12)	75	1.1325	102.70	21.05	21.61
(24,15)	55	1.3338	88.71	22.41	28.2
(25,19)	20	1.4962	108.55	25.50	11.85
(28,22)	35	1.6991	107.86	26.04	9.67
(29,20)	20	1.6704	121.19	23.95	9.71

Table 5.2: Listed are different carbon nanotube segments, defined by the chiral indices (n, m) and the number of unit cells. The values for B_{min} are extracted from the numerical calculated transmission as a function of both energy and parallel magnetic field. The spin-orbit coupling parameter δ and the lead coupling d vary slightly, the values for each carbon nanotube can be found in the corresponding plot. The calculation for the $(29, 20)$ carbon nanotube is depicted in figure 5.4 and the additional ones in appendix C.

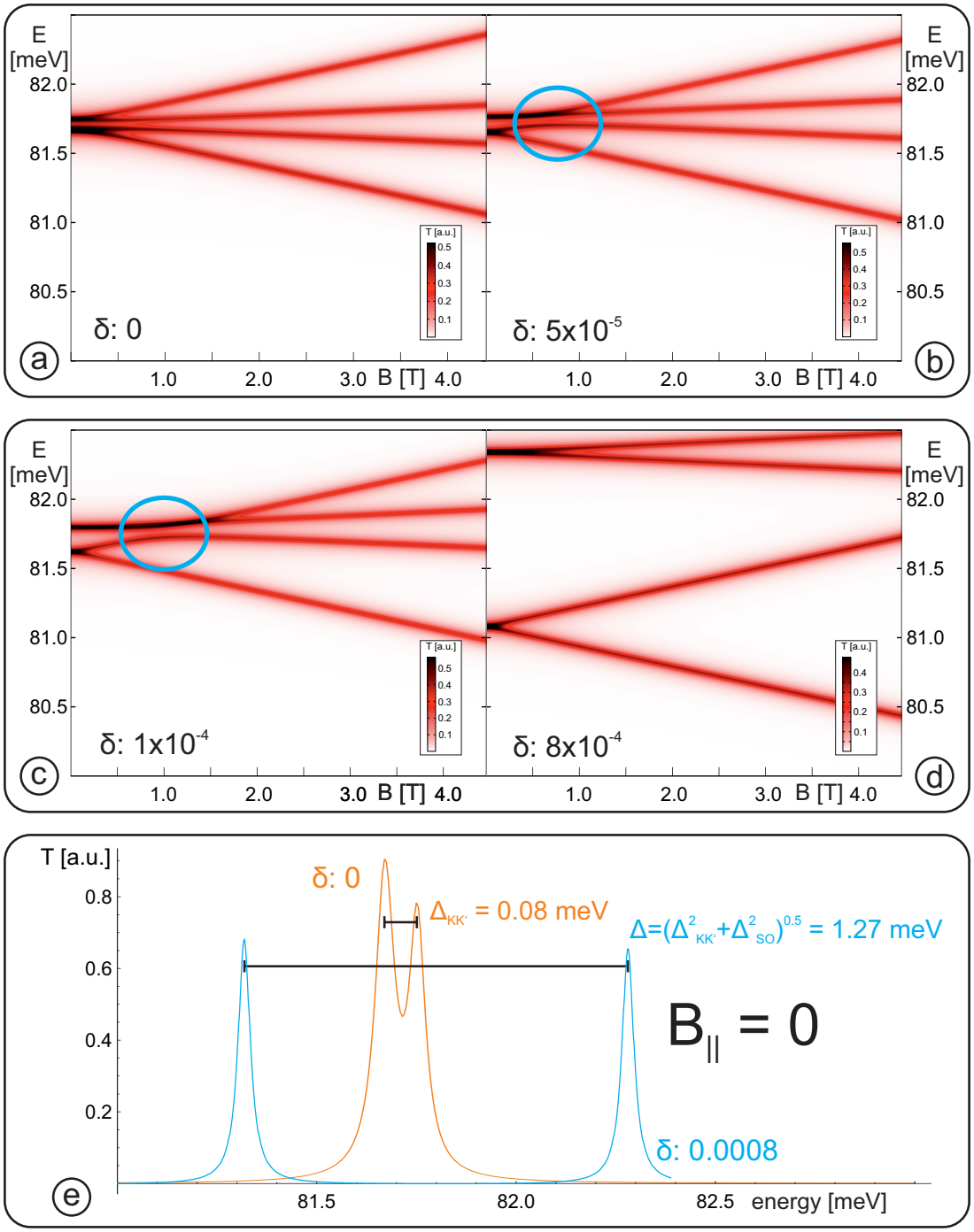

Figure 5.3: Calculated transmission as a function of both energy and parallel magnetic field for a $(5, 2)$ carbon nanotube with a length of 88.68 nm ($N = 100$). The lead coupling is set to $d = 5$ meV. The spin-orbit coupling is varied from $\delta = 0$ (a) to $\delta = 0.0008$ (d). (e) shows two line traces at zero magnetic field for $\delta = 0$ (orange) and $\delta = 0.0008$ (cyan). For $\delta = 0$ the KK' splitting is directly observable; for finite δ the energy splitting Δ is visible.

spin-orbit parameter δ

In figure 5.4 the transmission is calculated as a function of both energy and parallel magnetic field for a $(29, 20)$ carbon nanotube with a length $L = 121.19\,\mathrm{nm}$ $(N = 20)$. The spin-orbit parameter δ is varied from $\delta = 0$ (a) to $\delta = 0.0005$ (d). The coupling parameter $d = 6\,\mathrm{meV}$ for the leads is kept constant. The value for B_{min} decreases with increasing δ. The spin-orbit coupling induces a shift of the momentum $k_\perp$ (compare equation 5.7):

$$\Delta k_\perp^{\mathrm{SO}} \propto \frac{\delta}{r}, \tag{5.22}$$

and for a constant radius r and an increasing value of δ leads to a decrease of the band gap near the K point. This results in a lower magnetic field value B_{min} for crossing the Dirac point.

radius r and chiral angle Θ

In order to see the effect which a change of the radius has on the spectrum of a carbon nanotube, we compare a $(14, 11)$ and $(28, 22)$ carbon nanotube, each with 35 unit cells. Their chiral angle and length are the same, the radii are $r_{(14,11)} = 0.8495\,\mathrm{nm}$ and $r_{(28,11)} = 1.6991\,\mathrm{nm}$. The value B_{min} decreases from $26.86\,\mathrm{T}$ to $9.67\,\mathrm{T}$. Both carbon nanotubes are nominally metallic and a band gap is introduced due to the curvature. The induced shift of the momentum $k_\perp$ (compare equation 5.6)

$$\Delta k_\perp^{\mathrm{c}} \propto -\frac{\cos(3\Theta)}{r^2}, \tag{5.23}$$

depends on the chiral angle and the radius. For a constant chiral angle the increased radius decreases the negative shift of the momentum $k_\perp$ and thus the Dirac point crossing is observed for lower magnetic field values.
In figure 5.5 the magnetic field value B_{min} for the Dirac point crossing is plotted as a function of $\cos(3\Theta)/r^2$; all shown carbon nanotubes are nominally metallic, increasing values

$$\cos(3\Theta)/r^2$$

lead to an increasing value for the Dirac point crossing. Not accounted for is here the slight variation in the length of the employed carbon nanotubes.

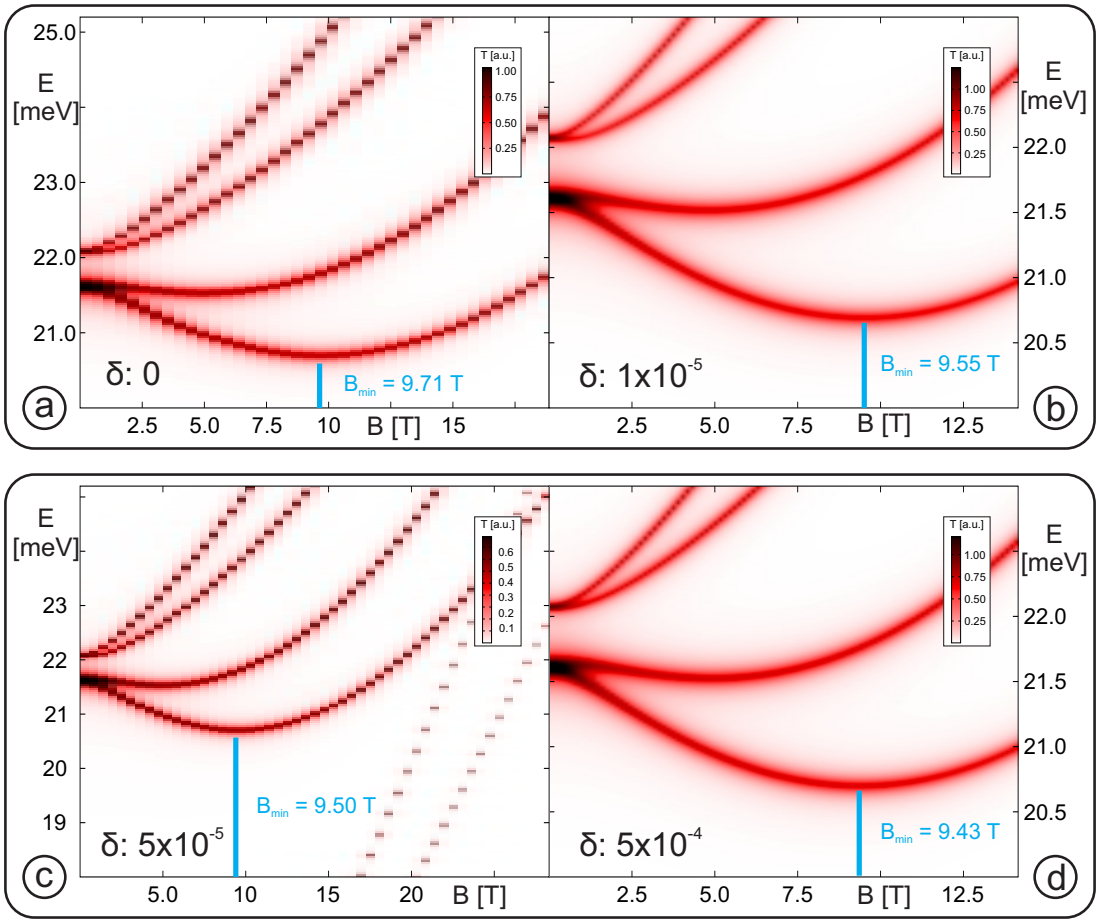

Figure 5.4: Calculated transmission as a function of both energy and parallel magnetic field for a $(29, 20)$ carbon nanotube with different spin-orbit coupling parameters δ. Lead coupling $d = 6\,\text{meV}$ and length $L = 121.19\,\text{nm}$ are kept constant. The Dirac point crossing shifts to lower values in magnetic field for increasing δ. The two additional lines visible in (c) are explained in section 5.5.

length L

In figure 5.6 the transmission is calculated as a function of both energy and magnetic field, for different lengths of a $(29, 20)$ carbon nanotube. The contact coupling parameter $d = 6\,\text{meV}$ and the spin-orbit coupling parameter $\delta = 1 \cdot 10^{-5}$ are kept constant. For an increasing length, the crossing through the Dirac point is shifted to lower magnetic field values B_{min}. Figure 5.7 shows the values B_{min} as function of the length of the carbon nanotube. A fast decrease of B_{min} is observed up to a length of 100 nm; above a length of 200 nm the value for the crossing through the Dirac point decreases a lot more slowly.

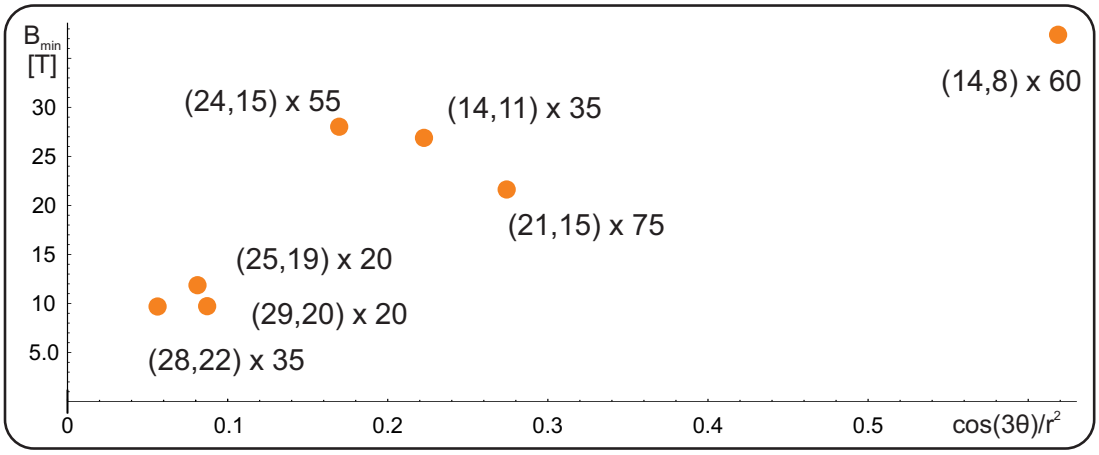

Figure 5.5: Value of the magnetic field $B_{\min}$ for the Dirac point crossing as a function of $\cos(3\Theta)/r^2$.

The length dependence of the Dirac point crossing reads:

$$B_{\min} \propto \frac{1}{\sqrt{L}}, \tag{5.24}$$

see cyan dashed line in figure 5.7.
The length dependence of the Dirac point crossing for a $(14, 11)$ carbon nanotube is also depicted in figure 5.7, again the magnetic field value for the Dirac point crossing is proportional to $L^{-0.5}$ (orange dashed line in figure 5.7). The calculated transmissions for the $(14, 11)$ carbon nanotube are shown in appendix C.

5.4 Magnetic field dependence of $k_{\|}$

For high magnetic field we observe a decrease of the transmission through the carbon nanotube, e.g. a $(29, 20)$ carbon nanotube with a length of 500 nm were the transmission decrease above 5 T (compare figure 5.6(f)). This decrease was also observed in the measured, numerical derived conductance, see figure 5.2.
The decrease of the magnetic field value for the Dirac point crossing and the decrease of the transmission/conductance can be explained with a magnetic field dependent value for the momentum shift $k_{\|}$; in equation 5.3 the momentum shift $k_{\|}$ was assumed to be constant. First the variation of $k_{\|}$ in a magnetic field is introduced, and then both observations due to its dependence on the carbon nanotube length are explained.

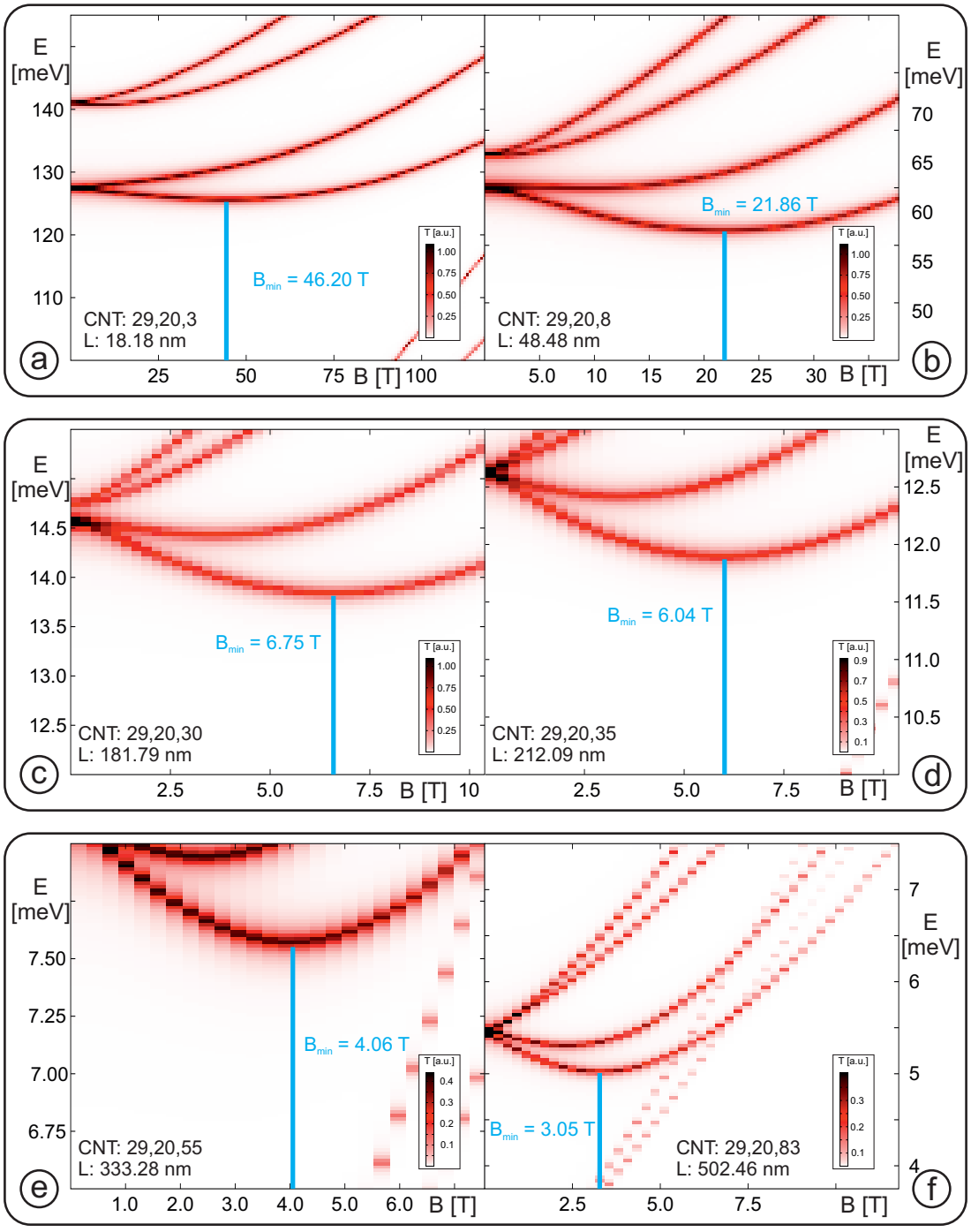

Figure 5.6: Calculated transmission as a function of both energy and parallel magnetic field for a $(29, 20)$ carbon nanotube with different lengths. The lead coupling $d = 6\,\text{meV}$ and the spin-orbit coupling parameter $\delta = 1 \cdot 10^{-5}$ are kept constant. The crossing through the Dirac point shifts to lower values in magnetic field for increasing length.

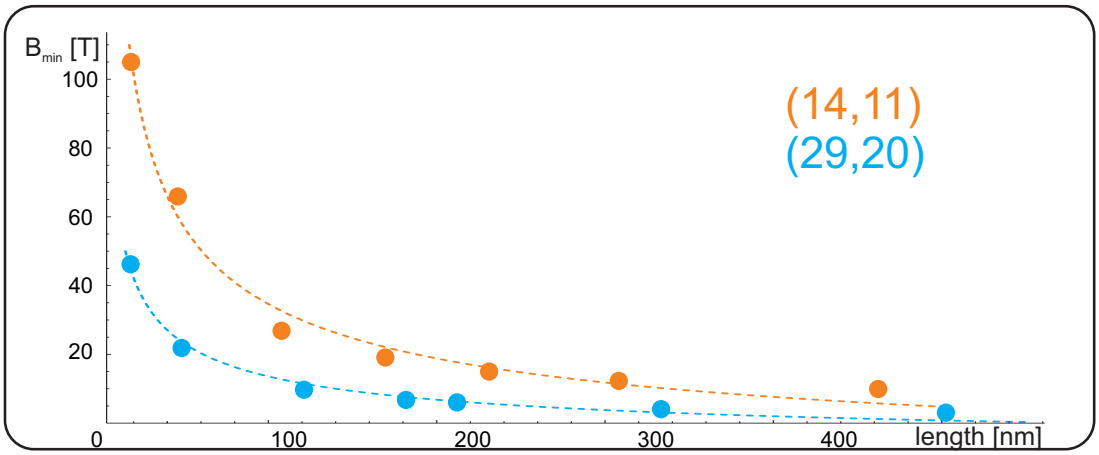

Figure 5.7: Value of the magnetic field for the crossing through the K point, as function of the length for a $(14, 11)$ and $(29, 20)$ carbon nanotube. The value B_{min} decreases for increasing length. The dashed lines represent a fitting curve proportional to $L^{-0.5}$, see text.

It was shown that the momentum shift $k_\parallel$ depends on the momentum shift $k_\perp$ [Marganska et al., 2011]:

$$\frac{\tau k_\perp + i k_\parallel}{\tau k_\perp - i k_\parallel} = e^{2 i k_\parallel L}, \tag{5.25}$$

and thus the moment shift $k_\parallel$ depends also on an applied parallel magnetic field. The value for $\tau k_\perp$ predicts whether the value for $k_\parallel$ is real or imaginary; a trivial solution of equation 5.25 would be $k_\parallel = 0$. If the momentum shift $k_\parallel$ is a real value, equation 5.25 can be written as:

$$\tau k_\perp = k_\parallel \cot\left(k_\parallel L\right). \tag{5.26}$$

this corresponds to an extended state. In figure 5.8 the solutions for the real values of $k_\parallel$ are plotted as a function of the value $k_\perp$, the imaginary and trivial solutions are omitted. For $k_\perp = 0$ the momentum shift $k_\parallel$ reads:

$$k_\parallel = \left(\frac{1}{2} + n\right)\frac{\pi}{L}, \tag{5.27}$$

see red dotted line in figure 5.8. For increasing values of $k_\perp$, the momentum shift $k_\parallel$ reaches asymptotically the value:

$$k_\parallel \xrightarrow{\text{increasing B}} \frac{n\pi}{L}, \tag{5.28}$$

compare green dotted line in figure 5.8. The consequence of this behavior is the following: For $k_\perp$ the factor 1/2 is responsible for the fact that the wave function of each sub-lattice A and B (see chapter 2) of a carbon nanotube has a node only at one end. If the magnetic field increases one obtains a shift of the momentum $k_\perp$ and this also induces a shift of the momentum $k_\parallel L$ following equation 5.25. The asymptotically reached value $k_\parallel = \frac{n\pi}{L}$ is like the quantum box and then the wave functions on both sub-lattices have nodes at both ends [del Valle et al., 2011, Marganska et al., 2011].

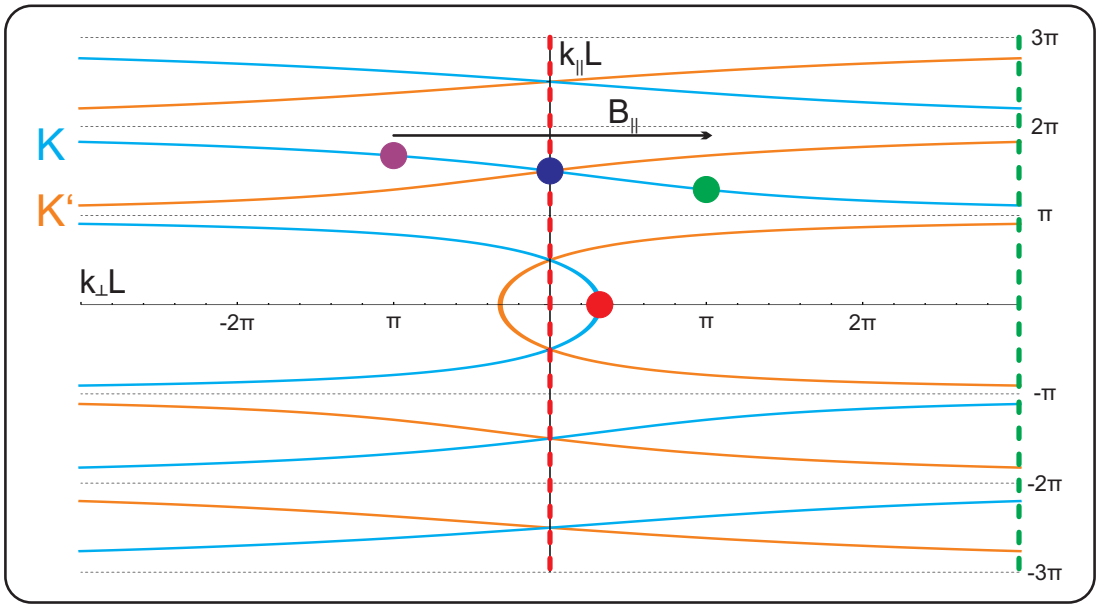

Figure 5.8: Plotted are the real solutions of equation 5.25, the trivial and imaginary solutions are omitted. Cyan lines correspond to the K valley and orange ones to the K' valley. The violet, blue and green dots mark the shifts of the momentum $k_\parallel$, see text. The black arrow indicates the shift of $k_\perp$ induced by a parallel magnetic field. The red dot marks the point, where only imaginary values for $k_\parallel$ are possible.

5.5 Comparison of numerical and analytical results

The change in the momentum $k_\parallel$ can explain the observed decrease of the transmission for high magnetic field and the decrease of the magnetic field value for the crossing through the K point with increased length.

Decrease of the transmission

Electronic transport through a carbon nanotube is possible if the wave functions for the two sub-lattices have a finite overlap and if at least a part of the electronic density is located near the contacts. This is the case for zero (and low) magnetic fields. As argued in the previous section for high magnetic fields the electronic density is more and more located at the center of the carbon nanotube. This implies that the electrons are far away from the ends and thus can not hop into the leads.
This was observed in the numerical transport calculations of the last section in a decrease of the transmission through a carbon nanotube, e.g. in figure 5.6(f) the transmission decreases for high magnetic fields.
This effect induced by the magnetic field depends on the length of the carbon nanotube. For shorter segments in figure 5.6 or the $(5, 2)$ carbon nanotube in figure 5.3, only a weak decrease of the transmission is visible in the calculated range of the magnetic field.

Length dependence of the magnetic field value corresponding to the crossing through the K point

We have observed in the numerical results that an increasing length of a carbon nanotube decreases the value $B_{\min}$ for the crossing point through the K point. Looking at figure 5.8 we start for the K point on the left side of the $k_\perp = 0$ axis for zero magnetic field (violet dot). The magnetic field decreases the momentum $k_\perp$ (shift towards the blue dot indicated by the black arrow); this leads also to a decrease of the momentum $k_\parallel$ and thus the energy depending on $\sqrt{k_\parallel^2 + k_\perp^2}$ decreases. At a certain value of the magnetic field one reaches $k_\perp = 0$ (blue dot). Further increased magnetic field will now increase $k_\perp$ again (shift towards green dot), but $k_\parallel$ will still decrease. The energy depends on $\sqrt{k_\parallel^2 + k_\perp^2}$ and so the variation of the energy depends now on the interplay of an increasing $k_\perp$ and decreasing $k_\parallel$. At a certain magnetic field the increase of $k_\perp$ can compensate the decrease of $k_\parallel$ and thus the energy is raising again. This is magnetic field value we named $B_{\min}$.
Note that we start on the second line for the valley K. If we start on the first one at a certain point (red dot) only imaginary values for $k_\parallel$ are possible. These correspond to evanescent waves localized at the carbon nanotube ends. The two levels corresponding to the first line of the valley K' increase linearly and are visible in several numerical transmission calculations, e.g. figure 5.4(c) or figure 5.6(f).
Increasing the length of the carbon nanotube compresses the lines in figure 5.8. For short carbon nanotubes $k_\parallel$ decreases faster than for long carbon nanotubes. Accordingly the influence of $k_\parallel$ is weaker for long carbon nanotubes and the value $B_{\min}$ is mostly governed by the decrease of $k_\perp$.

Influence of a magnetic field depended $k_\parallel$ on the analytic model

In section 5.1 a comparison of the recorded measurement data and an analytic model was shown. For this model, the momentum shift $k_\parallel$ was kept constant with respect to the magnetic field. From the numerical transmission calculations it turns out that a magnetic field induced shift of the momentum $k_\parallel$ has to be included. In figure 5.9 the numerical calculations for a $(28, 22)$ carbon nanotube are compared to the analytic model. If the $k_\parallel$ is kept constant, both models do not fit together, see figure 5.9(a). Including a shift of the momentum $k_\parallel$ induced by a shift of the momentum $k_\perp$ depending on equation 5.25 leads to good agreement of numerical transmission calculations and analytic model, see 5.9(b). In figure 5.9(c,d) the analytic model with non-constant $k_\parallel$ is compared with the numerical transmission calculations for a $(29, 20)$ with a length of $L = 121.19\,\mathrm{nm}$ (c) and $L = 502.46\,\mathrm{nm}$ (d); again a good agreement is observed. In figure 5.9(b) the agreement for high magnetic fields is much better than in 5.9(c,d). This fact might be due to the to small magnetic field range shown in 5.9(c,d) up to only $22(12)\,\mathrm{T}$. In the analytic model used in figure 5.2 an additional asymmetry term ($\propto a_B B_\parallel$) depending on the magnetic field was introduced to obtain a qualitative agreement with the experiment. This term was neglected in figure 5.9. The magnetic field induced shift of the momentum $k_\parallel$ might be related to the asymmetry term $a_B(B_\parallel)$ employed for the analytic fit of our measurement.

5.6 Comparing numerical transmission calculations and measured single particle spectrum

In figure 5.2 the measured conductance is plotted as a function of both bias voltage and parallel magnetic field. The single particle spectrum of the first electron is observed in the experiment. The Dirac point crossing is observed at a parallel magnetic field around $6\,\mathrm{T}$.
In this chapter we presented numerical transmission calculations as a function of both energy and parallel magnetic field. We could show that the Dirac point crossing crucially depend on length, radius and chiral angle of a carbon nanotube; in addition a slight influence of the spin-orbit coupling is observed. If one can fit the numerical calculations to the measured device, in principle the indices (n, m) of the carbon nanotube can be identified.
Since one has four different parameters, it is hard to obtain a quantitative agreement of the measured carbon nanotube and numerical calculations. The results of this chapter show that we can tune the values n, m, N, δ to achieve a crossing around the value obtained in the experiment. The best way would be to fix same of the values by means of other experiments, e.g. fix the radius of the carbon nanotube via atomic force microscopy measurements.

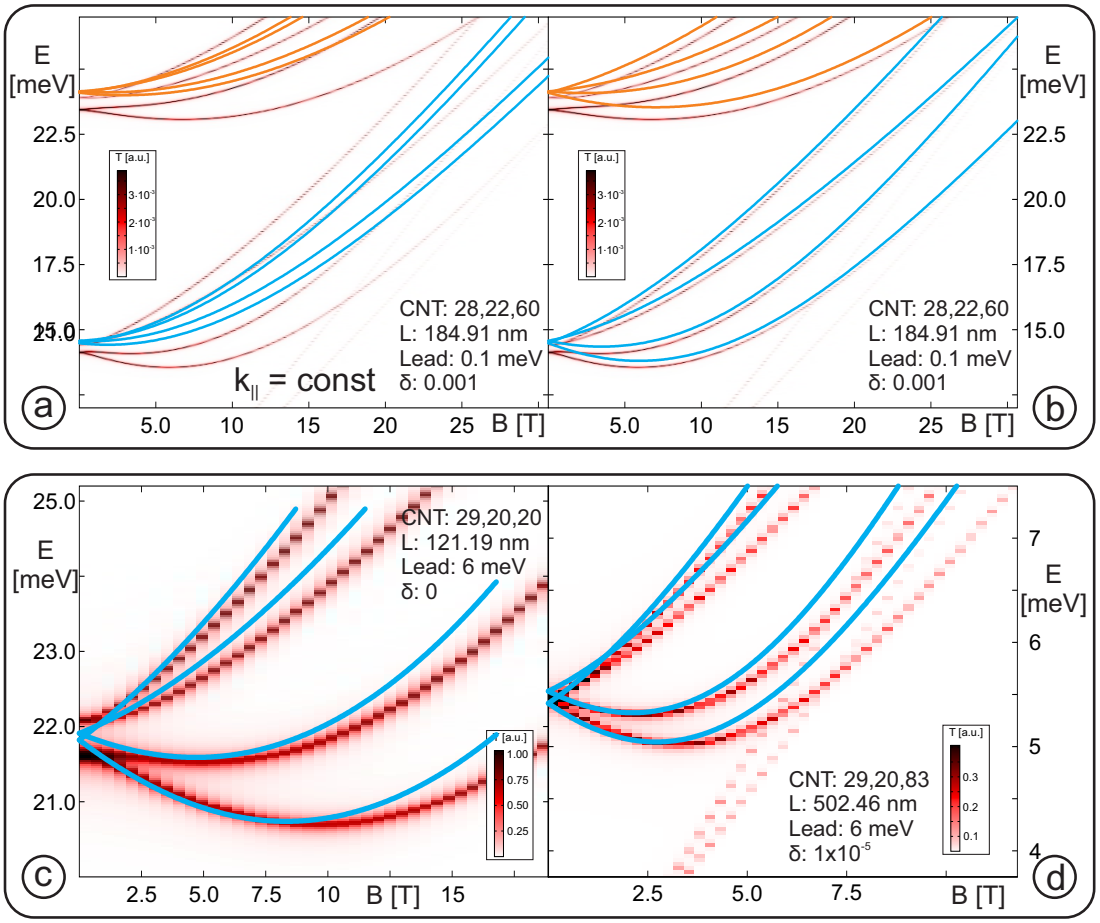

Figure 5.9: Depicted are numerical transmission calculations as a function of both energy and parallel magnetic field for a $(28, 22)$ (a,b) with a length of $L = 184.91\,\text{nm}$ and a $(29, 20)$ carbon nanotube with a length of $L = 121.19\,\text{nm}$ (c) and a length of $L = 502.46\,\text{nm}$ (d). In addition an analytic model for each carbon nanotube is shown. In (a) the momentum shift $k_\parallel$ was kept constant; numerical calculation and analytic model does not coincide. For (b-d) a shift of $k_\parallel$ according to equation 5.25 was employed for the analytic fit, yielding a good agreement with the numerical transmission calculations for the shown carbon nanotubes.

CHAPTER 6

Magnetic field induced electron-vibron coupling in a carbon nanotube quantum dot

The interplay of electronic transport and mechanical motion in single electron tunneling was first observed in a C_{60}-oscillator; equidistant excited lines in the differential conductance were observed [Park et al., 2000]. The effect of vibrational sidebands on the transport properties was studied theoretically using molecular junctions [Braig and Flensberg, 2003]. Vibrational sidebands visible in the electronic transport are explained by a model based on the Franck-Condon principle; a short overview will follow later in this chapter. The Franck-Condon principle is known from molecular physics: the electronic transitions are so fast that the nuclear positions do not change [Franck and Dymond, 1926, Condon, 1926]. The transition rate is proportional to the overlap integral of the two involved, spatially displaced quantum states. A first experimental observation of a coupling of electrons and the longitudinal stretching mode in a suspended carbon nanotube was reported by [Sapmaz et al., 2006a]; transport spectroscopy measurements as function of both gate voltage and bias voltage were presented exhibiting a Coulomb diamond stability diagram, see chapter 4. The vibrational sidebands lead to additional steps in the recorded d.c. current as a function of the bias voltage. The important quantity is the electron-vibron coupling parameter g. For a coupling factor $g << 1$ additional steps would not be observed. A coupling factor much larger than one leads to phonon blockade in low bias transport [Leturcq et al., 2009]. The relevant measurements of the numerically derived conductance for few electrons in the carbon nanotube quantum dot were already presented in chapter 4; the single particle spectrum evolving in a parallel magnetic field was briefly discussed in chapter 5. In this chapter we will focus on the transition from $N = 1$ to $N = 2$ electrons.

6.1 Vibrational modes in carbon nanotubes

Different vibrational modes arise in suspended carbon nanotubes, here we will focus on the typically low energetic ones:

Radial breathing mode

The radial breathing mode (RBM) describes a motion of the carbon nanotube lattice perpendicular to the carbon nanotube axis, see figure 6.1(a). Due to the elongation and constriction perpendicular to the axis, the energy depends on the diameter d and is independent of the length L of the carbon nanotube. For the fundamental, radially symmetric carbon nanotube RBM the energies reads [LeRoy et al., 2004, Dresselhaus and Eklund, 2010]:

$$E_{\mathrm{RBM}} = 27.8 d^{-1}[\mathrm{nm}]\,\mathrm{meV}. \tag{6.1}$$

Bending mode

The bending mode of a carbon nanotube is typically observed in driven beam experiments, compare chapter 7. The carbon nanotube oscillates perpendicular to its axis (see figure 6.1(c)), the quantization energies depend on the tension T, the radius r and the length L. For the temperature range accessible with common dilution systems the quantization of the bending mode cannot be observed. In [Mariani and von Oppen, 2009] it is claimed that even for $\hbar\omega \approx k_B T$ the coupling factor g is much smaller than one and no signs of an electron-vibron coupling are to be expected.
In [Island et al., 2012] an experimental observation of an electron-vibron coupling in the bending mode induced by a positive feedback of electron tunneling and the mechanical vibrating bending mode of the carbon nanotube was claimed. Indeed the coupling factor is on the order of 10^{-3}; the observations are explained by an enhanced effective coupling due to a positive feedback by a oscillating electrostatic force induced by the bending vibration of the carbon nanotube. This positive feedback effect is also observed in other experiments [Schmid et al., 2012, Stiller et al., 2013].

Stretching mode

Another mode occurring in carbon nanotube is the stretching mode; the carbon nanotube moves along its longitudinal axis. The vibrational energy quantum for the stretching mode reads [Landau and Lifschitz, 1989, Sapmaz et al., 2006a]:

$$h f_{\mathrm{SM}} = E_{\mathrm{SM}} = \frac{n_{\mathrm{vib}} h}{L}\sqrt{\frac{E}{\rho}} \approx \frac{0.11\,\mathrm{meV}}{L[\mu m]}, \tag{6.2}$$

including the Young's modulus E, the carbon nanotube mass density ρ and the vibrational mode number n_{vib}. In figure 6.1(d) the energies for the different modes are plotted as a function of the carbon nanotube length. For comparison the expected length dependents of electronic excitations are marked. Different experiments on suspended carbon nanotubes and their corresponding energies are marked. The dotted orange line corresponds to the length of 700 nm; the length of the suspended part of the carbon nanotube in our device.

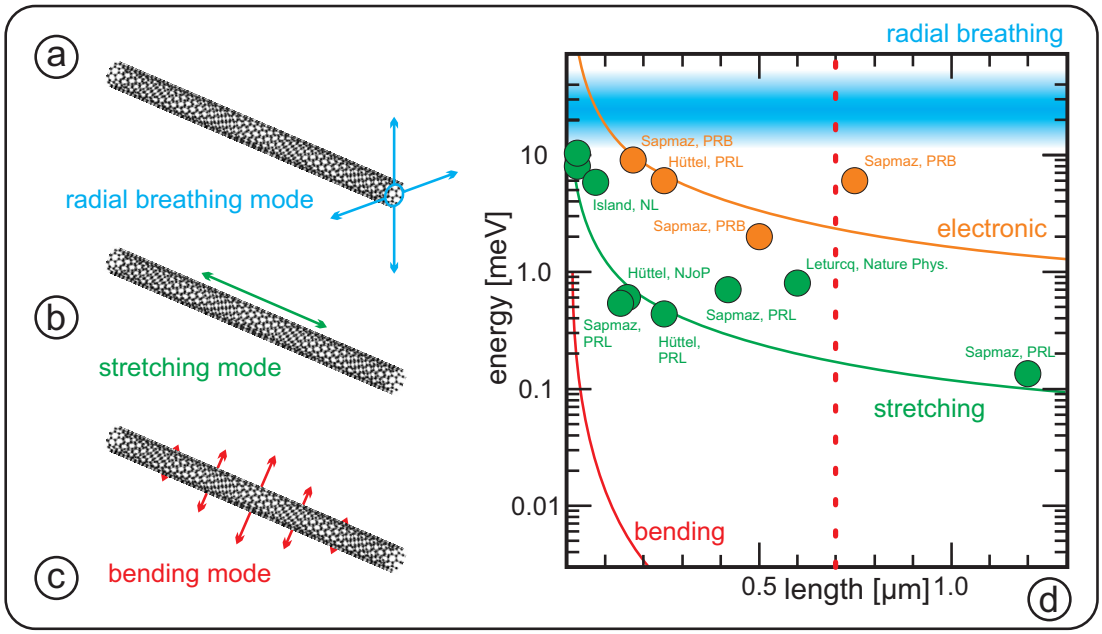

Figure 6.1: (a) RBM of a carbon nanotube; the motion is perpendicular to the carbon nanotube axis. The stretching mode deforms the carbon nanotube lattice along the carbon nanotube axis (b). The transverse bending mode is sketched in (c). (d) Vibrational energy quantum hf as a function of the length of the carbon nanotube. The orange line corresponds to the energy dependence of electronic excitation; orange dots represent the experiments [Sapmaz et al., 2005, Hüttel et al., 2009b]. The green line corresponds to the energy dependence of excitations due to the stretching mode; green dots represent the experiments [Sapmaz et al., 2006a, Hüttel et al., 2008, Hüttel et al., 2009b, Leturcq et al., 2009, Island et al., 2012]. The red straight line sketches the energy dependence of the bending mode; the blue line represents the RBM. The red dotted line corresponds to the trench width of our device and thus the estimated suspended part of the carbon nanotube. Redrawn following [Hüttel et al., 2008].

6.2 Franck-Condon model

The Franck-Condon model in molecular physics assumes that the electronic transition is so fast that the nuclear position does not change during the transition. For the case of a carbon nanotube this means: The atomic carbon nanotube lattice does not move during the electronic tunneling. To obtain tunnel rates one has to take into account the vibrational part of the macro-molecule wave function. Only the initial and final state of the vibration influence the tunnel rate. So the overall tunnel rate Γ reads:

$$\Gamma = \Gamma_{\text{electron}} | < \Psi_{\text{initial}} | \Psi_{\text{final}} > |^2, \tag{6.3}$$

where Γ_{electron} is the electronic tunnel rate. $| < \Psi_{\text{initial}} | \Psi_{\text{final}} > |$ represents the overlap of the two vibrational wave functions; in absence of vibrational effects $| < \Psi_{\text{initial}} | \Psi_{\text{final}} > | = 1$ since $\Psi_{\text{initial}} = \Psi_{\text{final}}$, and thus $\Gamma = \Gamma_{\text{electron}}$. A detailed expression for the current through a molecular junction including the vibrational effects is presented in [Braig and Flensberg, 2003].
A step-like behavior of the current is predicted as a function of the bias voltage. For finite temperature the system can absorb and emit vibrons; if the temperature is going to zero only emission is possible and the function P_n is describing the current step heights by a Poisson distribution [Braig and Flensberg, 2003]:

$$P_n = \frac{e^{-g} g^n}{n!}, \tag{6.4}$$

with

$$Q_n = \sum_n P_n = 1, \tag{6.5}$$

the parameter g describes the coupling between electrons and vibrons. The approximation using the step-function Q_n is valid for strong relaxation; the initial state involved in the vibrational transition is then always its ground state.
The coupling parameter g is defined as the ratio:

$$g = \frac{l^2}{2 l_0^2}. \tag{6.6}$$

The classical displacement l of the carbon nanotube lattice describes the shift of the ground state position induced by an additional charge carrier; the length l_0 of the quantum harmonic oscillator can be seen as a zero-point motion of the mechanical oscillator [Hüttel et al., 2008]:

$$l_0 = \sqrt{\frac{\hbar}{m\omega}}. \tag{6.7}$$

The length l_0 is on the order of a few picometer for $\omega \approx 1\,\mathrm{THz}$ and $m \approx 10^{-21}\,\mathrm{kg}$. The step-function P_n is sketched in figure 6.2 for different values of g. For $g = 0$ no steps arise; for $g << 1$ the steps are very small and it is expected that a coupling effect of vibrons and electrons is not observable; for $g \approx 1$ additional steps in the current characteristics can be observed and for high values of g the current for low bias is blocked. This is called phonon blockade and was already observed experimentally in carbon nanotubes [Leturcq et al., 2009]; a coupling factor of 3.3 was observed there.
In [Sapmaz et al., 2006a] it is already discussed that an inhomogeneous electron density (e.g. charge located in the center of the suspended carbon nanotube) can lead to coupling factors $g \approx 1$. The electron density can be modified by substrate impurities and the back gate.
The coupling of the carbon nanotube lattice motion and the transverse and parallel electric fields is discussed in the early theoretical work of [Flensberg, 2006]. The electric fields are caused by the traveling electrons and the electrostatic interaction with a gate electrode. It is predicted that the longitudinal electric field is too weak to observe a coupling to the carbon nanotube lattice motion. Indeed a coupling to transverse electric fields can provide a coupling of electrons and vibrons with a coupling factor $g \approx 1$. Furthermore the location and the size of the vibron compared to the electronic state have significant influence on the coupling factors. If the vibron is located inside the quantum dot defined within the carbon nanotube, the Franck-Condon coupling factor is position-dependent. Also a asymmetric location of the vibron with respect to the electronic quantum dot leads to asymmetric coupling factors at the tunnel barriers [Cavaliere et al., 2010].
In [Mariani and von Oppen, 2009] the electron-vibron coupling originating from intrinsic electron-phonon coupling in carbon nanotubes is discussed in detail; the coupling strengths for RBM, bending, and stretching mode are discussed.
A recent theoretical work by [Donarini et al., 2012] predicts that the size and position relation between electronic quantum dot and vibron strongly influence the coupling regime. A detailed analysis of the electron-vibron coupling including also multiple vibronic modes is provided; details will be discussed later.

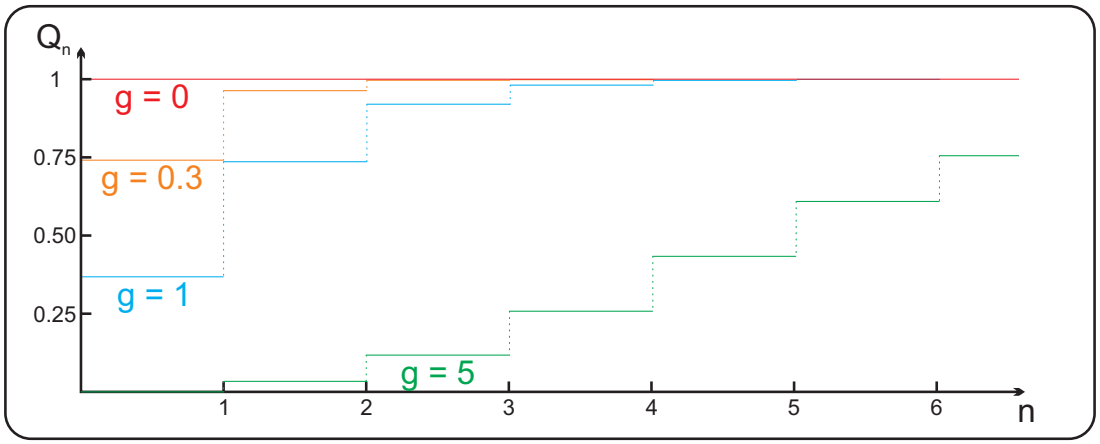

Figure 6.2: Function P_n for different values of the coupling parameter g. For $g = 0$ no steps are visible; for increasing values of g steps arise. For $g > 1$ the first steps are suppressed exponentially.

6.3 Magnetic field induced coupling

Regarding the electronic properties, the measurements of the single particle spectrum in a high parallel magnetic field were already discussed in chapter 5. Figure 6.3(a) shows the current through the carbon nanotube as function of both bias voltage V_{bias} and parallel magnetic field $B_{\parallel}$. The gate voltage is set to $V_{\text{gate}} = 0.7599\,\text{V}$ in order to observe the transition from $N = 1$ to $N = 2$ electrons, compare chapter 4. The cyan crosses in figure 6.3 sketch the position of the applied gate voltage relative to the regions of single electron tunneling and Coulomb blockade in the stability diagram. The bias voltage is varied as $0\,\text{mV} \leq V_{\text{bias}} \leq 3.75\,\text{mV}$ and the parallel magnetic field is varied as $-0.1\,\text{T} \leq B_{\parallel} \leq 3.15\,\text{T}$. Figure 6.3(b) shows the conductance $|\text{d}I/\text{d}V|$ derived numerically from the current recorded in figure 6.3(a).
For increasing parallel magnetic field additional side peaks of the electronic ground state energy arise. Below 1 T only a main peak is observed, up to 2 T one additional side peak. For higher magnetic field values ($B_{\parallel} \approx 3\,\text{T}$) a spectrum of equidistant side peaks is observed, see figure 6.4(a): the main peak and three additional side peaks are visible, the energy spacing between the peaks is about 74 µeV. This would correspond to a carbon nanotube length of 1.5 µm; compared to other experiments (see figure 6.1) this is the correct order of magnitude.
In figure 6.4(b) the current through the carbon nanotube is plotted as a function of the bias voltage for a constant parallel magnetic field. Steps in the $I\,(V_{\text{bias}})$ arise (though broadened) as predicted by the Franck-Condon model. We take the current I_0 of the first plateau in the $I\,(V_{\text{bias}})$ curves. After normalizing the current I_0 by setting the maximal current $I_{\text{max}} = 1$ (see figure 6.4(b)), we can calculate the coupling constant g from the function $P_0 = I_0 = e^{-g}$. The addi-

tional current steps (I_1 in figure 6.4(b)) can be calculated using the extracted g. In figure 6.4(b) we obtain a value of $g = 0.302$ for $B_{\parallel} = 2.90\,\mathrm{T}$. The coupling factor g is extracted for several magnetic fields; in figure 6.5 the coupling factor g is plotted as a function of $B_{\parallel}$. Below the value of $B_{\parallel} \approx 1.5\,\mathrm{T}$ only one peak in the numerically derived conductance is visible, and no steps in the $I\,(V_{\mathrm{bias}})$ curves and thus the coupling parameter g could not be extracted. At a parallel magnetic field $B_{\parallel} \approx 1.5\,\mathrm{T}$ the coupling factor g increases linearly.

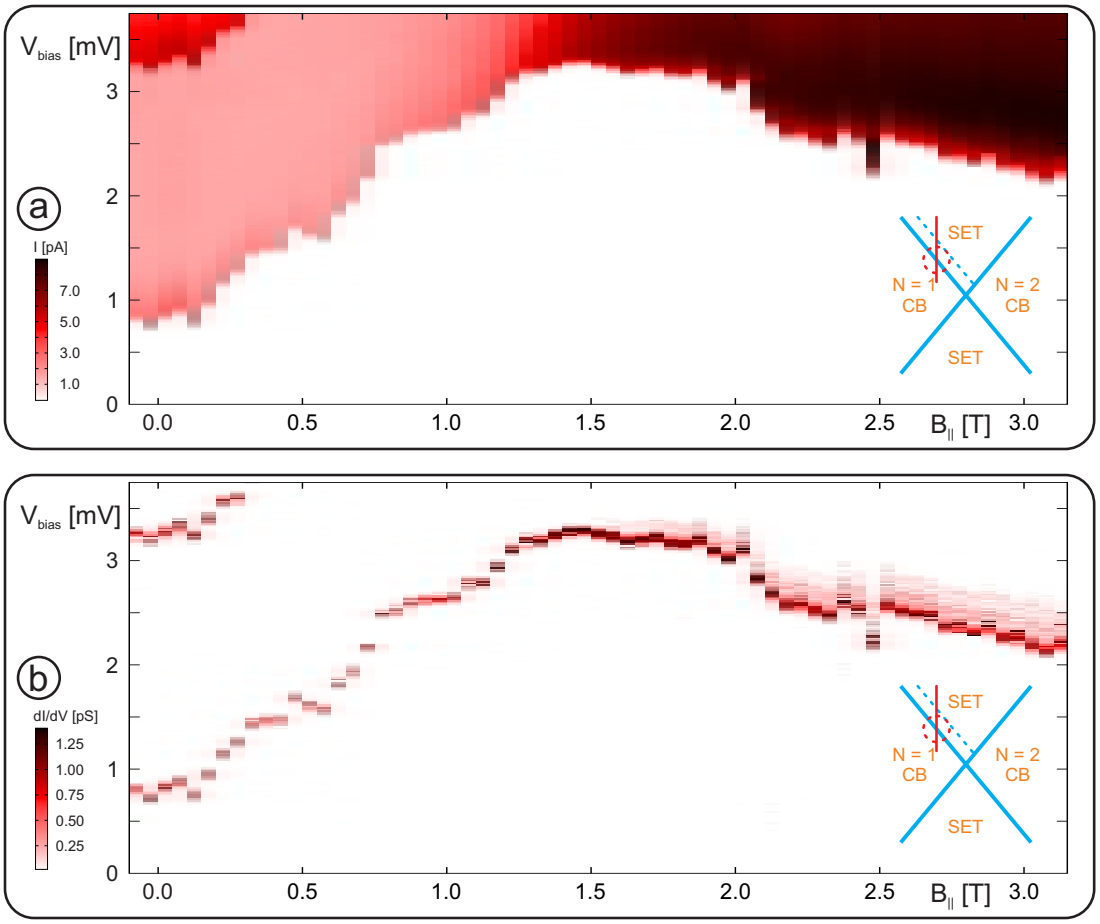

Figure 6.3: (a) Current as function of both bias voltage V_{bias} and parallel magnetic field $B_{\parallel}$. The gate voltage is fixed to $V_{\mathrm{gate}} = 0.7599\,\mathrm{V}$, the cyan crosses sketch the position of the applied gate voltage. The bias voltage is varied from $0\,\mathrm{mV} \leq V_{\mathrm{bias}} \leq 3.75\,\mathrm{mV}$ and the parallel magnetic field from $-0.1\,\mathrm{T} \leq B_{\parallel} \leq 3.15\,\mathrm{T}$. Above 1 T the current after the ground state spectral line increases. In (b) the numerically derived conductance $|\mathrm{d}I/\mathrm{d}V|$ obtained from (a) is plotted.

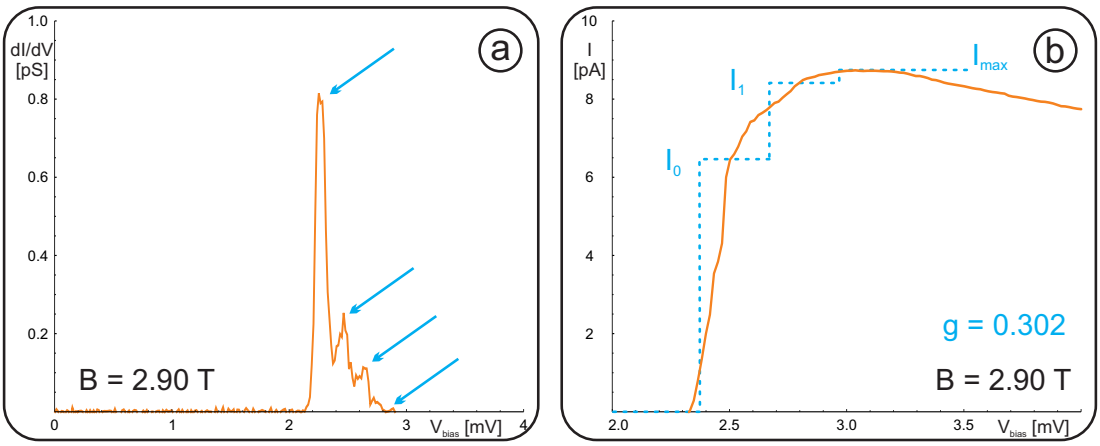

Figure 6.4: A trace of the numerically derived conductance $|\mathrm{d}I/\mathrm{d}V|$ as a function of the bias voltage V_{bias} for $B_{\parallel} = 2.90\,\mathrm{T}$ is shown (a). A main peak and three additional side peaks arise (marked with cyan arrows). (b) Current as function of the bias voltage. The maximal current I_{max} is set to one and the step-function P_n is employed to extract the coupling factor $g = 0.302$. Both traces are obtained from figure 6.3.

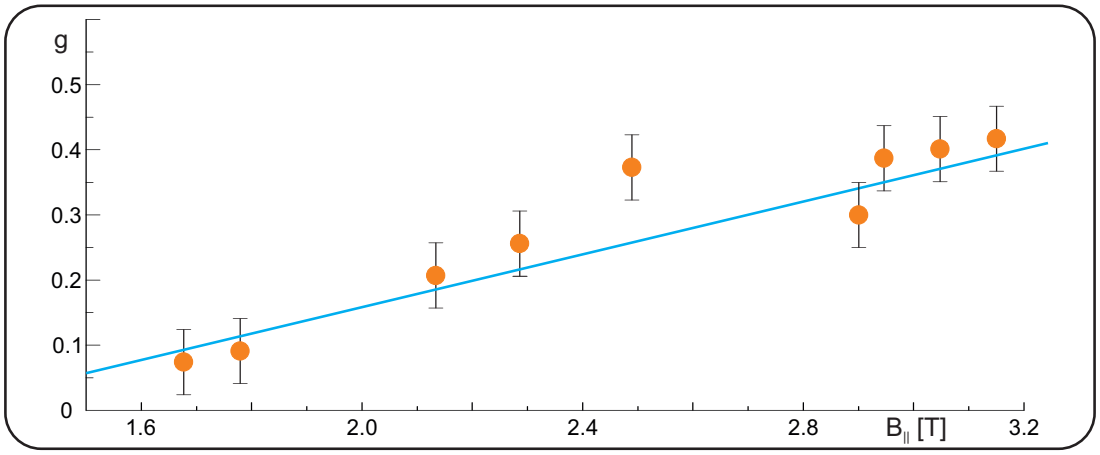

Figure 6.5: Plotted is the coupling factor g as a function of the parallel magnetic field. Above 1.5 T the coupling factor increases linearly. For each data point a trace of the current as a function of the bias voltage ($I\,(V_{\mathrm{bias}})$) is taken at fixed parallel magnetic field, and g is extracted employing the $I_{\mathrm{max}} = 1$ and the step function P_n, see text for details. In figure 6.4(b) an example is depicted.

In figure 6.6 the numerically derived conductance is plotted as a function of both bias voltage and parallel magnetic field. The gate is again set to $V_{\text{gate}} = 0.7599\,\text{V}$, and the bias voltage is varied from $0\,\text{mV} \leq V_{\text{bias}} \leq 10\,\text{mV}$, however the parallel magnetic field is now varied over a much larger range $0\,\text{T} \leq B_{\parallel} \leq 15\,\text{T}$. A lot of excited states are visible; we concentrate on the ground state corresponding to the lowest bias voltage. For increasing magnetic fields again additional side peaks arise. Note what we again focus on the same ground state spectral line as depicted in the measurement of figure 6.3. At a magnetic field $B_{\text{parallel}} \approx 1.5\,\text{T}$ an anti-crossing (marked green in figure 6.6) and thus a ground state transition is visible, details will follow later.
Though we observe additional side peaks in the numerically derived conductance, in this data set no clear steps in the $I\,(V_{\text{bias}})$ traces are visible and thus we can not extract the coupling factor g that way.
Instead we use the area under the differential conductance peaks, this is mathematically equivalent since:

$$\int \frac{\mathrm{d}I}{\mathrm{d}V_{\text{bias}}} \mathrm{d}V_{\text{bias}} = I \tag{6.8}$$

The ratio of the calculated areas are then employed to calculate the coupling factor g:

$$\frac{A_1}{A_0} = \frac{P_1}{P_0} = \frac{e^{-g}g}{e^{-g}} = g, \tag{6.9}$$

where A_0 is the area under the main peak and A_1 the area under the side peak 1. Note that we assume constant spacing between the conductance peaks. In addition we use the area ratio of side peak 2 (A_2) and side peak 1:

$$\frac{A_2}{A_1} = \frac{P_2}{P_1} = \frac{0.5e^{-g}g^2}{e^{-g}g} = 0.5g, \tag{6.10}$$

In figure 6.7(a) the extracted coupling factors g are plotted as a function of the parallel magnetic field $B_{\parallel}$; red squares correspond to a coupling factor extracted from the ratio side peak 1/main peak, and the green stars represent the coupling factor extracted from the ratio side peak 2/side peak 1. Within the error bars a agreement of both coupling values is visible. Starting of a value $B_{\parallel} \approx 2\,\text{T}$ the coupling factor increases linearly with a maximum value $g \approx 0.45$ at $B_{\parallel} \approx 3.3\,\text{T}$. For further increased values of the parallel magnetic field, we observe a slight decrease of the coupling factor. In figure 6.7(b) the extracted coupling factors of the two measurements shown in figure 6.3 and figure 6.6 are compared. Both methods are in good agreement in the low magnetic field range ($1.5\,\text{T} < B_{\parallel} < 3.5\,\text{T}$).

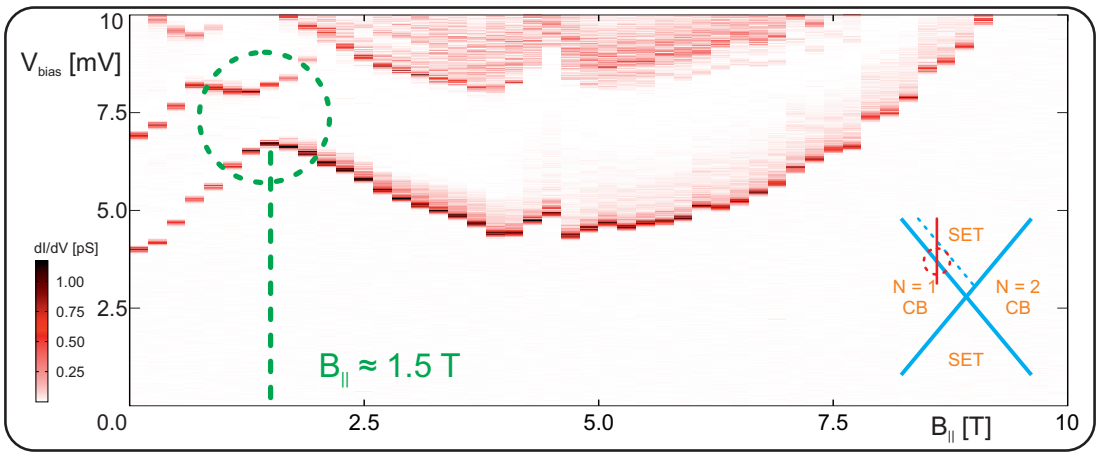

Figure 6.6: Depicted is the numerically derived conductance $|\mathrm{d}I/\mathrm{d}V|$ as function of both bias voltage and parallel magnetic field. The gate voltage is fixed to $V_{\mathrm{gate}} = 0.7599\,\mathrm{V}$, the cyan cross sketches the applied gate voltage. The bias voltage is varied from $0\,\mathrm{mV} \leq V_{\mathrm{bias}} \leq 10\,\mathrm{mV}$ and the parallel magnetic field from $0\,\mathrm{T} \leq B_{\parallel} \leq 10\,\mathrm{T}$. The green cycle marks an anti-crossing and a ground state transition, see text.

6.4 Physical origin of the magnetic field induced coupling

The coupling of electrons to the stretching mode of a carbon nanotube depends on the position of the electronic quantum dot defined in the carbon nanotube, and the position of the vibron. This was briefly discussed in section 6.2 and theoretically predicted by [Mariani and von Oppen, 2009, Donarini et al., 2012]. In [Sapmaz et al., 2006a] it was already discussed, that the localization of electrons plays a role for the strength of the electron-vibron coupling. It seems plausible that the position of the vibron is fixed to the suspended part of the carbon nanotube. Since the length of the suspended part of the carbon nanotube and thus the size of the vibron is fixed, changes of the electronic confinement are expected.

In chapter 5 we could show that a parallel magnetic field affects the electronic wave function. Specifically, for high magnetic fields the electronic density is more and more located in the center of the quantum dot and thus transport through the carbon nanotube decreases. This is also visible in the high magnetic $B_{\parallel}$ measurement of figure 6.6.

The maximal current I_{max} (already introduced in the previous section) of the ground state observed in figure 6.6 is proportional to the electronic tunneling rate $\Gamma_{\mathrm{electron}}$. In figure 6.8 the current I_{max} is plotted as a function of the parallel magnetic field. Starting from low magnetic field, the maximum current I_{max}

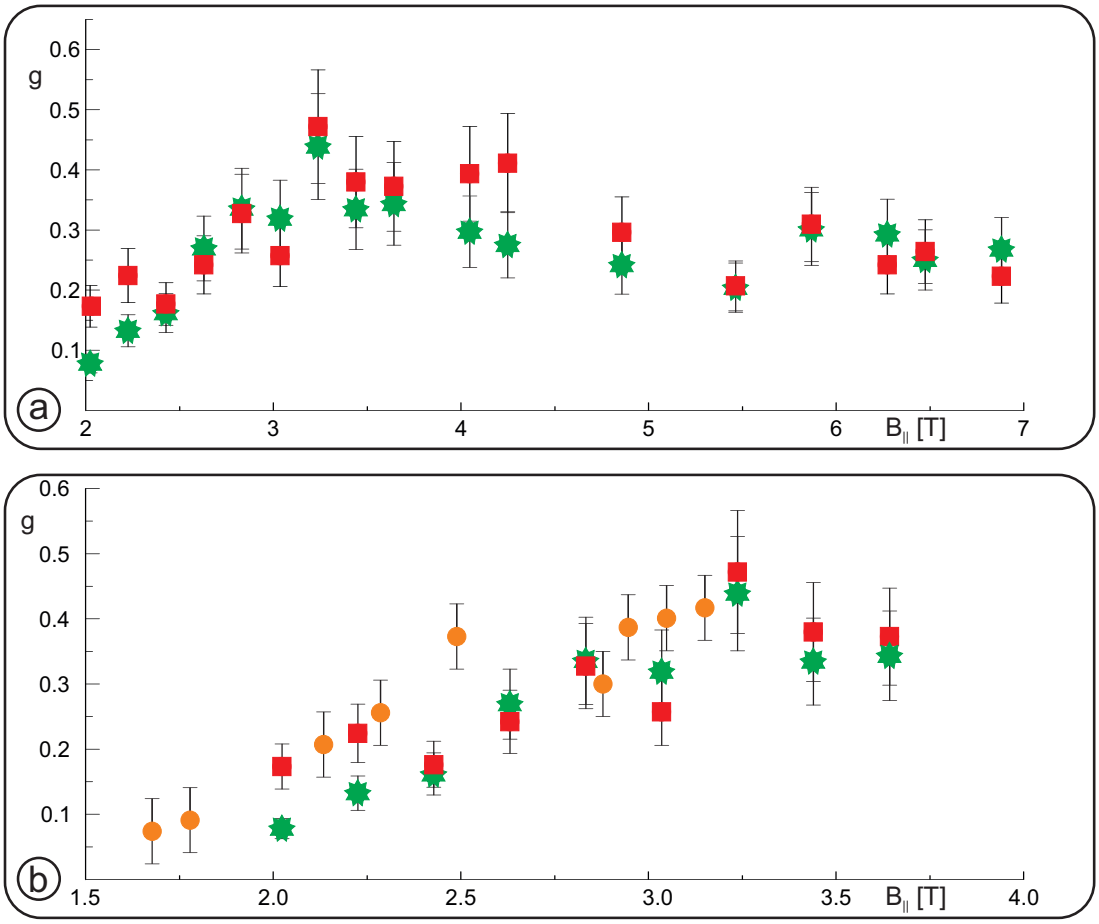

Figure 6.7: (a) Coupling parameter g extracted using the area under the differential conductance peaks obtained from the measurement depicted in figure 6.6. Red square correspond to ratio side peak 1 / main peak, and green stars to the ratio side peak 2/side peak 1, see text. In addition the coupling factor g (see figure 6.5) extracted from the $I\,(V_{\mathrm{bias}})$ curves (orange dots) is depicted (b). Both methods are in good agreement for the shown magnetic field range.

increases and has its maximum around $B_{\parallel} \approx 3.5\,\mathrm{T}$. For higher parallel magnetic fields the current $I_{\max}$ decreases again. The extracted coupling factors g exhibit also a maximum in the same range of the parallel magnetic field and a slow decrease is visible for higher magnetic field values. In figure 6.8 the ground state transition is marked green (see also figure 6.6), here the form of the electronic wave function changes. Interestingly the value $B_{\parallel} \approx 1.5\,\mathrm{T}$ nearly coincides with the starting point of the increasing electron-vibron coupling factor, see figure 6.7. This magnetic field induced shift of the electronic wave function may affect the coupling of electrons and vibrons resulting in the observed dependence of the coupling factor as a function of a parallel magnetic field.

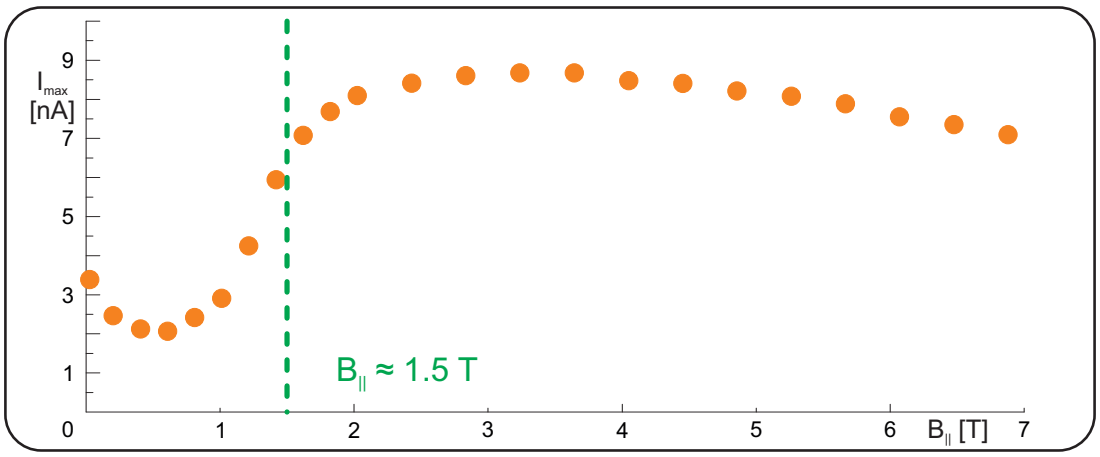

Figure 6.8: Maximal current $I_{\max}$ as a function of the parallel magnetic field. A maximum around $B_{\parallel} \approx 3.5\,\mathrm{T}$ is observed. For high magnetic field values the current $I_{\max}$ decreases slightly, see text. The green dotted line corresponds to the ground state transition observed in the measurement shown in figure 6.6.

CHAPTER 7

Negative frequency tuning of a carbon nanotube mechanical oscillator

In this chapter we present measurements on a suspended carbon nanotube device, observing mechanical resonance in transport measurements and also multiple higher harmonic mechanical resonance frequencies. First the basic theory of the flexural bending mode of a carbon nanotube is presented, resulting in a gate depended resonance frequency.
A positive frequency tuning of the bending mode was observed several times in carbon nanotube devices [Sazonova et al., 2004, Schmid et al., 2012, Moser et al., 2013, Poot et al., 2007]; an increasing gate voltage increases also the tension of the carbon nanotube due to higher electrostatic attraction of the global gate electrode and the carbon nanotube. This stiffens the carbon nanotube and leads to a higher resonance frequency of the bending mode.
Indeed a negative frequency tuning was observed in this device. We were able to decrease the mechanical resonance frequency to 75 % of its maximum value by an applied back gate voltage.
For the measurements of this chapter we employ a device of the ReMo type, see chapter 3.2. Unfortunately the gate finger was nonfunctional due to fabrication issues; the back gate was used to vary the electro-chemical potential within the carbon nanotube. The sample was cooled down in a ^{3}He evaporation cryostat. The measurement of this chapter were performed in cooperation with Sabine Kugler; the main results are published in [Kugler, 2013, Stiller et al., 2013].

7.1 Mechanical properties of suspended, doubly clamped carbon nanotubes

Carbon nanotubes yield excelling mechanical properties, in particular low mass ($\approx 10^{-21}\,\mathrm{kg}$) and extreme high Young's modulus ($\approx 1\,\mathrm{TPa}$) [Lu, 1997]. In addition carbon nanotube nano-electromechanical systems make it possible to probe both mechanical and electronic quantities on the nano-scale. Here a basic description of carbon nanotube mechanics is given to understand the measurements of this thesis; for a more detailed discussion see e.g. [Witkamp, 2009].
As discussed in literature [Postma et al., 2005, Witkamp et al., 2006, Poot et al., 2007, Poot and van der Zant, 2012] suspended, doubly clamped carbon nanotubes can be modeled using classical Euler-Bernoulli theory for a cylindric beam [Cleland, 2010]. For the deflection U, the following differential equation results:

$$\rho A\frac{\partial^2 U}{\partial t^2}+\eta\frac{\partial U}{\partial t}+EI\frac{\partial^4 U}{\partial z^4}-T_{\mathrm{mech}}\frac{\partial^2 U}{\partial z^2}=F_{\mathrm{ext}}. \tag{7.1}$$

Here, F_{ext} is an external force driving the mechanical motion of the carbon nanotube. The carbon nanotube cross section reads $A=\pi r^2$, and $I=\frac{\pi r^4}{4}$ is the momentum of inertia [Lefèvre et al., 2005]. The tension T_{mech} of a carbon nanotube can be written as

$$T_{\mathrm{mech}}=T_0+\frac{EA}{2L}\int_0^L\left(\frac{\partial U}{\partial t}\right)^2\mathrm{d}z, \tag{7.2}$$

where L is the width of the trench. Fabrication procedures lead to an intrinsic tension T_0; the second term results from the beam deflection.
The differential equation 7.1 can be solved by separating the deflection $U(z,t)$ in a time-independent part $U_{\mathrm{dc}}(z)$ and a time-dependent part $U_{\mathrm{ac}}(z,t)$;

$$U(z,t)=U_{\mathrm{dc}}(z)+U_{\mathrm{ac}}(z,t). \tag{7.3}$$

Using equation 7.1 and equation 7.3 one obtains the two equations:

$$EI\frac{\partial^4 U_{\mathrm{dc}}}{\partial z^4}-T_{\mathrm{dc}}\frac{\partial^2 U_{\mathrm{dc}}}{\partial z^2}=F_{\mathrm{dc}} \tag{7.4}$$

and

$$\rho A\frac{\partial^2 U_{\mathrm{ac}}}{\partial t^2}+\eta\frac{\partial U_{\mathrm{ac}}}{\partial t}+EI\frac{\partial^4 U_{\mathrm{ac}}}{\partial z^4}-T_{\mathrm{dc}}\frac{\partial^2 U_{\mathrm{ac}}}{\partial z^2}-T_{\mathrm{ac}}\frac{\partial^2 U_{\mathrm{dc}}}{\partial z^2}=F_{\mathrm{ac}}e^{iwt}, \tag{7.5}$$

with the separated tension terms

$$T_{\mathrm{dc}} = T_0 + \frac{EA}{2L}\int_0^L \left(\frac{\partial U_{\mathrm{dc}}}{\partial t}\right)^2 \mathrm{d}z, \tag{7.6}$$

and

$$T_{\mathrm{ac}} = \frac{EA}{L}\int_0^L \left(\frac{\partial U_{\mathrm{dc}}}{\partial t}\right)\left(\frac{\partial U_{\mathrm{ac}}}{\partial t}\right) \mathrm{d}z. \tag{7.7}$$

Solving these equations self-consistently results in expressions for the resonance frequency dependence of a carbon nanotube mechanical resonator. Different regimes arise depending on the dominance of the tension energy compared to the bending energy (terms 3 and 4 in equation 7.1); for low T_{mech} the carbon nanotube can be seen as a hanging chain, and for high T_{mech} as a string under tension. A detailed analysis is presented in [Poot and van der Zant, 2012].
The carbon nanotube can be actuated contact-free using a nearby radio frequency (RF) antenna. On the one hand the carbon nanotube interacts directly with the electromagnetic field of the antenna, on the other hand the electromagnetic field of the antenna couples into the substrate generating an a.c. gate voltage.

7.2 Gate tuning of mechanical resonance

The distance of the carbon nanotube from the back gate is defined by

$$h = h_0 - U_{\mathrm{dc}}(z), \tag{7.8}$$

with the equilibrium height h_0 and the time-independent deflection $U_{\mathrm{dc}}(z)$ of the carbon nanotube perpendicular to the carbon nanotube axis. As approximation, the carbon nanotube is taken as an infinite long cylinder; the resulting capacitance between ground plane and carbon nanotube is given by

$$\begin{aligned} C_{\mathrm{gate}} = \frac{2\pi\epsilon_0}{\ln\left(\frac{2h}{r}\right)} &\approx \frac{2\pi\epsilon_0}{\operatorname{arccosh}\left(\frac{h}{r}\right)} \\ &\approx \frac{2\pi\epsilon_0}{\operatorname{arccosh}\left(\frac{h_0}{r}\right)} + \frac{2\pi\epsilon_0}{\sqrt{h_0^2 - r^2\operatorname{arccosh}^2\left(\frac{h_0}{r}\right)}} U_{\mathrm{dc}}(z). \end{aligned} \tag{7.9}$$

This leads to a electrostatic force on the carbon nanotube [Witkamp et al., 2006]:

$$F_{\mathrm{dc}} = \frac{1}{2}\frac{\mathrm{d}C_{\mathrm{gate}}(z)}{\mathrm{d}U}V_{\mathrm{gate}}^2 = \frac{\pi\epsilon_0}{\sqrt{h_0^2 - r^2}\,\mathrm{arccosh}^2\left(\frac{h_0}{r}\right)}V_{\mathrm{gate}}^2. \tag{7.10}$$

As one can see this external force depends on the applied back gate voltage.

7.3 Measurement setup and detection technique

For the measurements of this chapter a ^{3}He evaporation cryostat was used to cool the device down to a base temperature of 280 mK. The basic elements of a ^{3}He evaporation cryostat are shown in figure 7.1(a). A charcoal sorb pumps the gas phase of the ^{3}He-pot, lowering the pressure of the gas above the liquid ^{3}He. Resulting evaporation cooling leads to a decrease of the temperature of liquid ^{3}He from 3.2 K to 280 mK. For recondensing of the ^{3}He the charcoal sorb is heated up and the 1K-pot condenses the gaseous ^{3}He.
In figure 7.1(b) the low temperature measurement and actuation setup is depicted. The bias voltage is applied using a voltage divider; the resulting current through the carbon nanotube device is amplified at room temperature and recorded by a multimeter. A second voltage source and a low pass filter are employed to vary the back gate voltage and thereby the electro-chemical potential within the carbon nanotube. The low pass filter at the back gate should reduce ac fluctuations of the gate voltage. The suspended carbon nanotube is actuated contact-free by the radio frequency (RF) radiation of an antenna installed near the sample holder, see figure 7.2.
The mechanical response of the oscillating carbon nanotube is detected in the d.c. current through the devices; for the details of the detection mechanism see [Hüttel et al., 2009a].

7.4 Electronic device characterization

First we give a short overview of the electronic device properties. Figure 7.3 shows a room temperature measurement of the carbon nanotube device; the gate voltage is varied from $0\,\mathrm{V} \leq V_{\mathrm{gate}} \leq 4\,\mathrm{V}$ while a bias voltage of $V_{\mathrm{bias}} = 10\,\mathrm{mV}$ is applied to the source electrode. At the drain electrode the d.c. current through the carbon nanotube is amplified and recorded. The resulting room temperature resistance R_{CNT} is in the range

$$R_{\mathrm{CNT}} \approx \frac{10\,\mathrm{mV}}{780\,\mathrm{pA}} \approx 12.85\,\mathrm{M\Omega}. \tag{7.11}$$

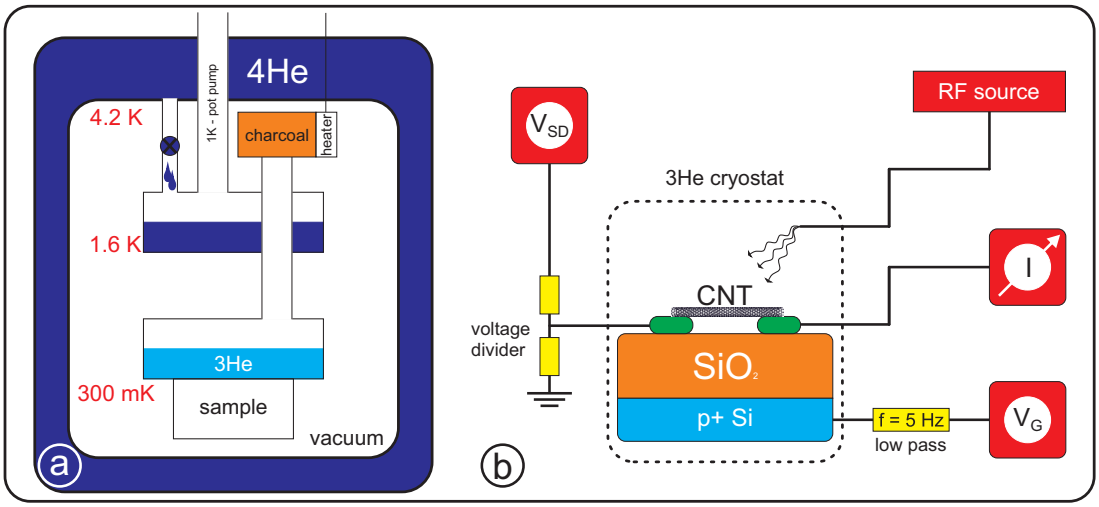

Figure 7.1: (a) Basic principle of a ^{3}He evaporation cryostat. ^{3}He is pumped by a charcoal and afterwards recondensed using a 1K-pot. (b) Low temperature measurement setup; a bias voltage is applied to the sample and the resulting current amplified and recorded by a multimeter. The carbon nanotube is driven contact-free by the RF fields emitted from an antenna. An applied gate voltage varies the electro-chemical potential of the carbon nanotube. (a) is adapted from [Enss and Hunklinger, 2005].

A low temperature measurements of the gate voltage dependence of the d.c. current is shown in figure 7.4. The gate voltage is varied from $0\,\mathrm{V} \leq V_{\mathrm{gate}} \leq 4\,\mathrm{V}$ at fixed bias voltage $V_{\mathrm{bias}} = 2\,\mathrm{mV}$. The resulting minimal low temperature resistance (near $V_{\mathrm{gate}} = 4\,\mathrm{V}$) reads

$$R_{\mathrm{CNT}} \approx \frac{2\,\mathrm{mV}}{30\,\mathrm{nA}} \approx 167\,\mathrm{k\Omega}. \tag{7.12}$$

The carbon nanotube device exhibits the typical different transport regimes of a small band gap carbon nanotube which are here not discussed in detail. On the hole conduction side a Fabry-Perot like oscillation of the current is visible for $V_{\mathrm{gate}} \leq 2.2\,\mathrm{V}$ [Liang et al., 2001], and the electron conduction side shows sharp peaks in the current trough the devices indicating Coulomb oscillations. For higher electron numbers Kondo effect is observed [Goldhaber-Gordon et al., 1998]; the low bias conductance in Coulomb blockade is enhanced for odd charging states of the carbon nanotube quantum dot due to the interaction of an unpaired spin on the quantum dot and the spins in the lead reservoirs.
By varying both the gate voltage V_{gate} and the bias voltage V_{bias} the well known Coulomb diamonds of differential conductance arise, as already discussed in chapter 4. Figure 7.5 shows such a measurement for the electron conduction side,

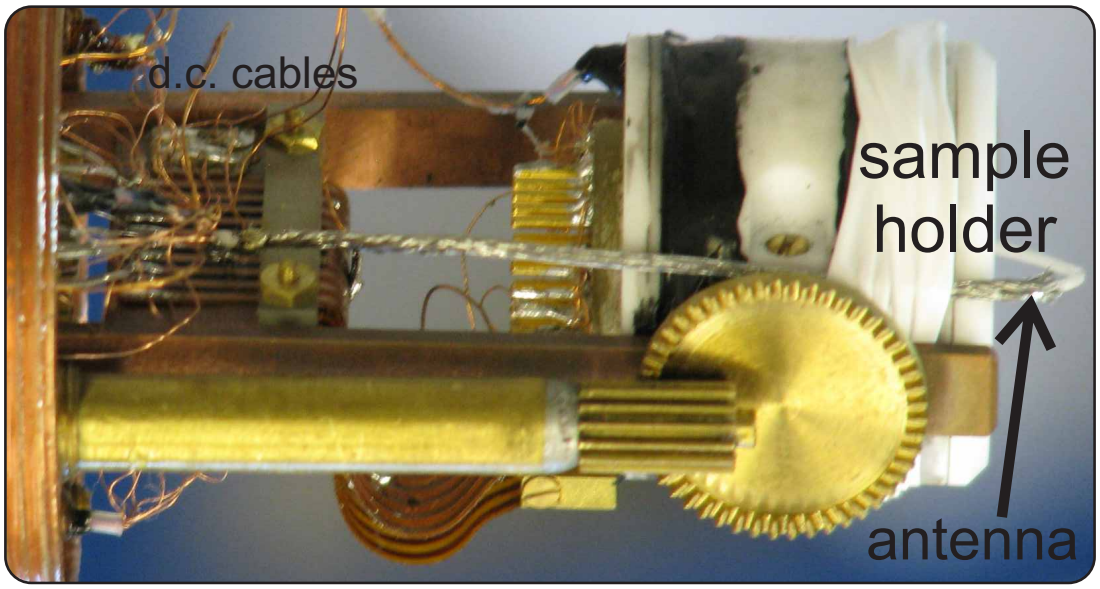

Figure 7.2: Sample stage of our ^{3}He evaporation cryostat. Visible is the sample holder, the cabling for d.c. measurements and the additional installed RF antenna for mechanical actuation of the transverse bending modes of a suspended carbon nanotube.

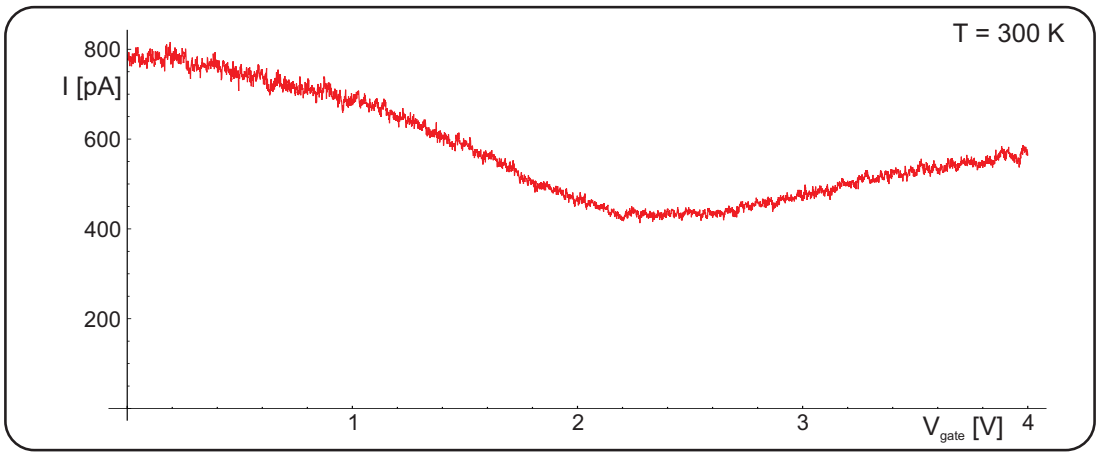

Figure 7.3: Room temperature measurement of the d.c. current through the device as function of the gate voltage, used for pre-characterization. The bias voltage is set to $V_{\mathrm{bias}} = 10\,\mathrm{mV}$. The gate voltage is varied from $0\,\mathrm{V} \leq V_{\mathrm{gate}} \leq 4\,\mathrm{V}$. The slight drop of the d.c. current around $V_{\mathrm{gate}} = 2.4\,\mathrm{V}$ indicates a small band gap behavior of the carbon nanotube.

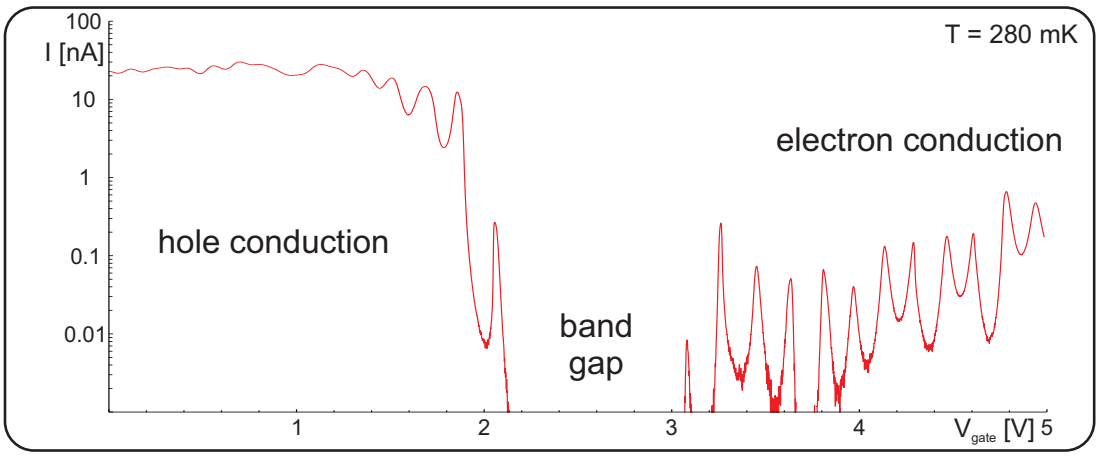

Figure 7.4: Low temperature measurement of the gate voltage dependence of the d.c. current while a constant bias voltage $V_{\mathrm{bias}} = 2\,\mathrm{mV}$ is applied between source and drain contact. The gate voltage is varied from $0\,\mathrm{V} \leq V_{\mathrm{gate}} \leq 5\,\mathrm{V}$. The resulting d.c. current through the carbon nanotube exhibits different transport regimes, see text.

in the gate region $2.815\,\mathrm{V} \leq V_{\mathrm{gate}} \leq 3.91\,\mathrm{V}$. The bias voltage is varied as $-10\,\mathrm{mV} \leq V_{\mathrm{bias}} \leq 10\,\mathrm{mV}$. Clearly visible are the Coulomb diamonds, i.e. regions of Coulomb blockade. For higher bias voltages they are smeared out and many additional in-elastic co-tunneling lines arise [De Franceschi et al., 2001], marked "a" in figure 7.5. Also gate dependent in-elastic co-tunneling lines arise (marked "b" in figure 7.5); a more complex potential structure with more than a single minimum along the carbon nanotube may cause this gate dependence [Goß et al., 2011].
A more interesting feature in terms of mechanical observations in carbon nanotubes are the sharp spikes at the Coulomb diamond edges marked "c" in figure 7.5. For high mechanical quality factors and low temperatures the carbon nanotube mechanical motion can be driven solely due to single electron tunneling through the embedded carbon nanotube quantum dot [Usmani et al., 2007, Schmid et al., 2012]. Note that up to now no external alternating force is applied to the carbon nanotube.

7.5 Driven mechanical resonator

Now the carbon nanotube is driven by applying an RF signal to the antenna. In resonance this leads to an oscillation of the transverse bending mode of the carbon nanotube. Figure 7.6(a) shows such a measurement; the bias voltage is set to $V_{\mathrm{bias}} = 2\,\mathrm{mV}$, the gate voltage to $V_{\mathrm{gate}} = 3.234\,\mathrm{V}$ and the nominal output power of the RF generator to $P = 2\,\mathrm{dBm}$. The frequency of the radio signal

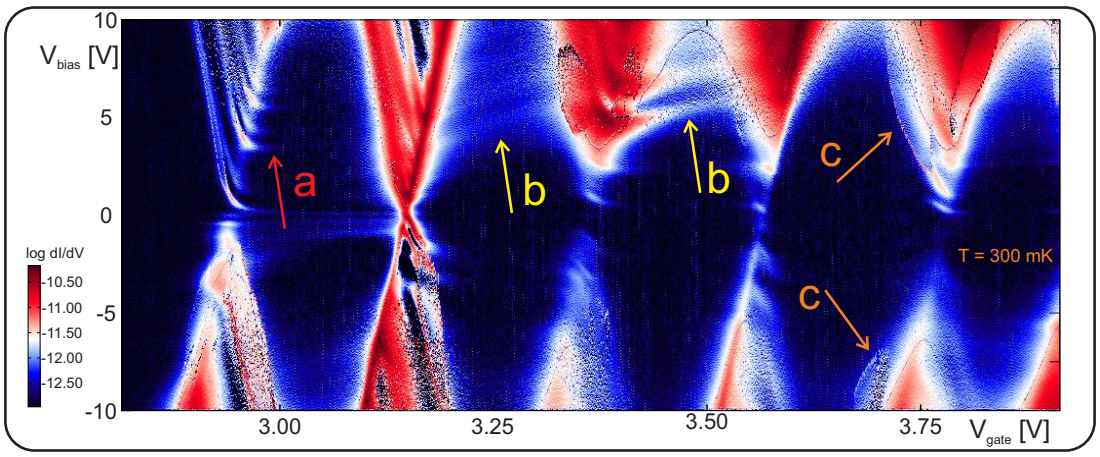

Figure 7.5: Plotted is the numerically derived conductance $|\mathrm{d}I/\mathrm{d}V|$ as a function of both gate voltage and bias voltage; $2.815\,\mathrm{V} \leq V_{\mathrm{gate}} \leq 3.91\,\mathrm{V}$ and $-10\,\mathrm{mV} \leq V_{\mathrm{bias}} \leq 10\,\mathrm{mV}$. Clear Coulomb diamonds and additional co-tunneling lines arise (red arrows, a) and also gate depended transport lines within the Coulomb diamonds (yellow arrows, b). The orange arrows (c) mark vibrational self-oscillation effects seen in the electronic transport measurements, see text.

is varied from 100 MHz to 600 MHz. Recorded is the d.c. current through the carbon nanotube. Many resonance features arise, as indicated by cyan arrows in figure 7.6(a). In figure 7.6(b) the resonance frequencies are extracted and labeled with mode numbers. A linear fit of the harmonics results in

$$f_n = n \cdot (71.4 \pm 0.4)\ \mathrm{MHz}, \tag{7.13}$$

yielding a quite good agreement with our data points. The additional features in figure 7.6(a) are labeled with their resonance frequency. Although the peaks show a response of the same type as a mechanical mode a clear explanation can not be given so far.

7.6 Negative frequency tuning

Figure 7.7 shows a measurement of the numerical derived current as a function of both gate voltage V_{gate} and applied RF signal. The range of the RF signal is adjusted to observe the first harmonic frequency of figure 7.6(a). The gate voltages is varied from $-12\,\mathrm{V} \leq V_{\mathrm{gate}} \leq 10\,\mathrm{V}$, the applied bias voltage is set to $V_{\mathrm{bias}} = 2\,\mathrm{mV}$ and a driving power of $P = 2\,\mathrm{dBm}$ is applied. As explained before the mechanical resonance frequency is expected to increase due to the applied gate voltage. Nevertheless we observe in this device a completely different gate dependence: the resonance frequency is lowered from its maximum value

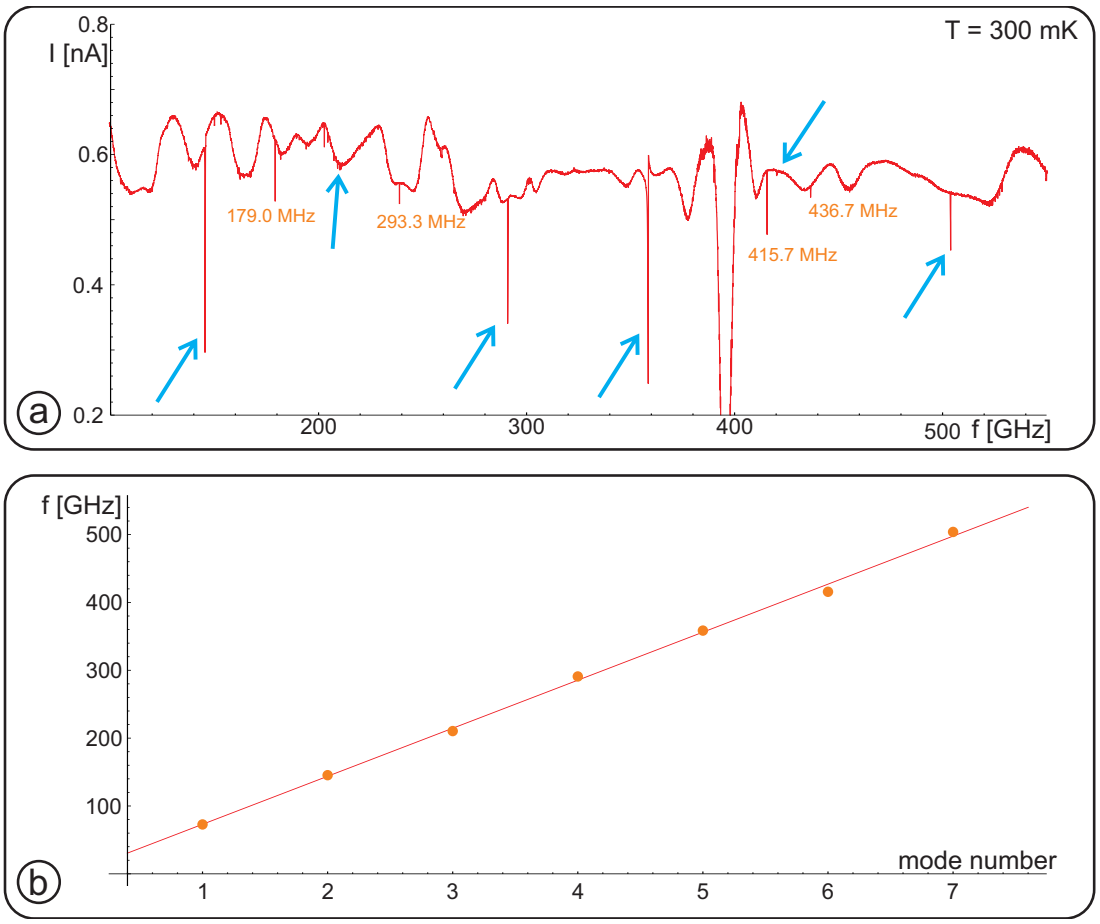

Figure 7.6: (a) Typical characterization measurement for a carbon nanotube mechanical oscillator. Bias voltage $V_{\mathrm{bias}} = 2\,\mathrm{mV}$ and gate voltage $V_{\mathrm{gate}} = 3.234\,\mathrm{V}$ are kept constant. The frequency of the applied RF signal is varied from 100 MHz to 600 MHz; plotted is the resulting d.c. current through the device. Resonance features listed in (b) are marked with cyan arrows. Additional features similar to mechanical resonances are labeled with their resonance frequency. (b) linear fit (red curve) of the extracted frequencies from (a) versus mode number (orange points), yielding $f_n = n \cdot (71.4 \pm 0.4)$ MHz.

of about 146 MHz to about 110 MHz at a gate voltage of $V_{\text{gate}} = -12\,\text{V}$. The maximum frequency can be found at a gate voltage $V_{\text{gate}} \approx 1.4\,\text{V}$. Similar effects have already been observed in carbon nanotubes using a dual gate setup for a weakly tensioned carbon nanotube. The gate dependence can be explained by electrostatic softening, an effective electrodynamic contribution to the carbon nanotube spring constant [Wu and Zhong, 2011].

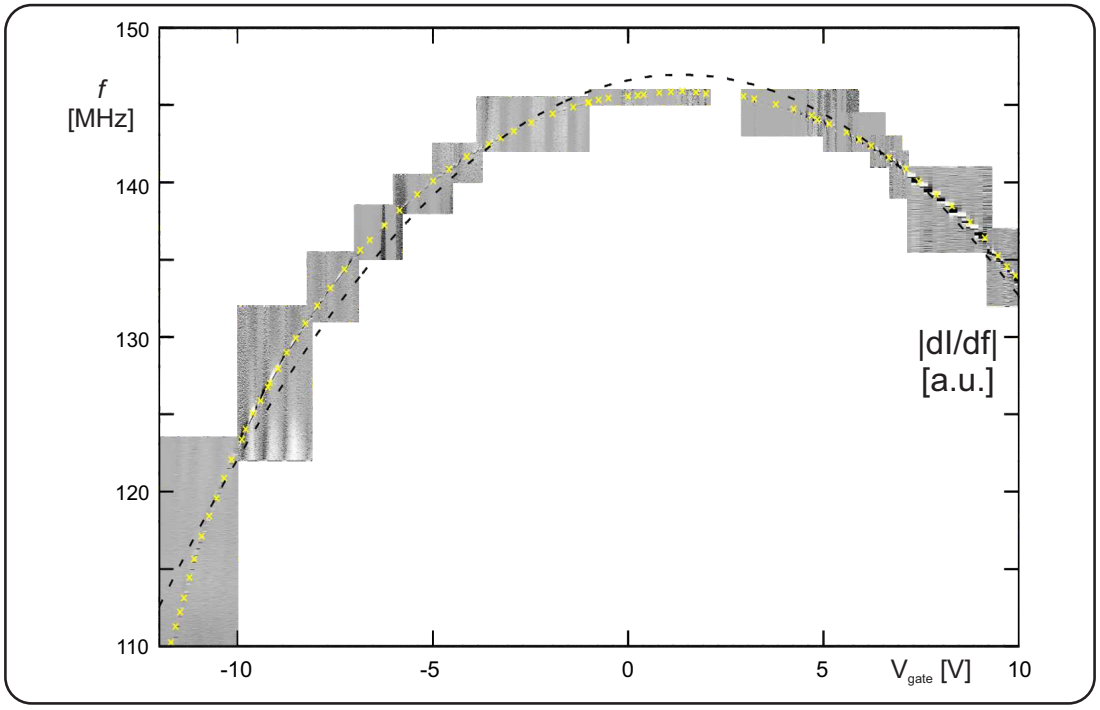

Figure 7.7: Plotted is the numerical derivative $|\mathrm{d}I/\mathrm{d}f|$ of the measured d.c. current with respect to the frequency of the driving signal. The bias voltage is set to $V_{\text{bias}} = 2\,\text{mV}$ and the RF output power to $P = 2\,\text{dBm}$. Yellow crosses mark the extracted resonance frequencies. The black curve represents a parabolic fit using equation 7.16. Taken from [Stiller et al., 2013] and modified.

For an oscillating carbon nanotube the distance h between gate and carbon nanotube is varying. By changing the distance h also the derivative of the capacitance between carbon nanotube and gate changes during one oscillation period. As mentioned in section 7.1, the electrostatic force on the carbon nanotube is given by

$$F_{\text{ext}} \propto \frac{\mathrm{d}C}{\mathrm{d}U}(z)\,. \tag{7.14}$$

Considering a small deflection δh the electrostatic force modulation δF_{ext} due to changes in the gate capacitance can be described via an effective spring constant contribution as

$$\delta F_{\text{ext}} \propto \delta h \frac{\mathrm{d}C^2}{\mathrm{d}^2 U}(z)\,. \tag{7.15}$$

We assume the mechanical tension of the carbon nanotube to be constant for low gate voltages. This is the tension of the carbon nanotube caused by the fabrication process. The resonance frequency of the carbon nanotube resonator reads now

$$f\left(V_{\text{gate}}\right) = f_{\max} - \beta\left(V_{\text{gate}} - V_{\text{gate},0}\right)^2, \tag{7.16}$$

with

$$f_{\max} = 0.5\sqrt{\frac{T_0}{mL}} \tag{7.17}$$

and

$$\beta = \frac{\mathrm{d}C^2}{\mathrm{d}^2 U}\frac{L f_{\max}}{4\pi^2 T_0}, \tag{7.18}$$

The black line in figure 7.7 shows the fitting of our data with equation 7.16; we can extracted $f_{\max} = 146.9\,\text{MHz}$, $V_{\text{gate},0} = 1.4\,\text{V}$ and $\beta = 0.192\,\text{MHzV}^{-2}$. Using the length $L = 500\,\text{nm}$ and assuming a mass of the carbon nanotube $m = 0.17 \cdot 10^{-21}\,\text{kg}$ we obtain for the tension $T_0 = 7.3\,\text{pN}$ and for the second derivative of the capacitance a value of $C'' = 7.5 \cdot 10^{-7}\,\text{Fm}^{-2}$.
For a rather simple model equation 7.16 gives a qualitative fit of our measurement. Not accounted are charge neutrality within the carbon nanotube band gap and a tension T_{mech} varying with the gate voltage.
For a cross check we model the carbon nanotube as a fine beam over a conducting plate, see section 7.2. From the geometrical values of the carbon nanotube device: mass m, gate distance h, estimated carbon nanotube radius r, and the width of the trenches L we can calculate a theoretical value of β. Using the value for the tension $T_0 = 7.3\,\text{pN}$ we obtain

$$\beta_{\text{theo}} = 0.521\,\text{MHzV}^{-2}. \tag{7.19}$$

Due to the simple model and all assumptions made, this is in good agreement with the experimental value of $\beta_{\text{exp}} = 0.192\,\text{MHzV}^{-2}$. A detailed calculation of β_{theo} can be found in appendix B.

CHAPTER 8

Coplanar waveguide resonators for carbon nanotube integrated circuits

As already mentioned in the introduction, carbon nanotubes are potential candidates for defining charge or spin qubits. The previous chapters presented measurements on clean, suspended carbon nanotubes. As a further step towards combining carbon nanotubes and coplanar waveguide (CPW) resonators, a reliable fabrication process and measurement setup for CPW resonators is necessary. We achieved niobium (Nb) quarter wavelength resonators with internal quality factors up to $2.4 \cdot 10^5$ with a silicon substrate and a post-grown Al_2O_3 layer. This additional isolation layer is necessary for future experiments with carbon nanotubes since we have to avoid contact between the ground plane of the CPW and the carbon nanotube electrode geometry. First of all a short description of our sample fabrication is given, details see appendix A.2. Afterwards the cryogenic setup is explained.
The behavior of the resonance frequency and the internal quality factor of a CPW resonator as function of temperature can be described by Matthis-Bardeen theory [Mattis and Bardeen, 1958]. Here, the resonance frequency is influenced by changes in the kinetic induction fraction. In the low-temperature limit, the loss due to two-level systems in the substrate material dominates the internal quality factor and the resonance frequency of the CPW resonator. Both models are briefly described. At the end of this chapter the potential combination of carbon nanotubes and CPWs in one device is discussed.

8.1 Device fabrication

Compared to carbon nanotube device fabrication, the challenges are different. Essentially one optical lithography step is required; after wafer cleaning metallic layers are deposited onto the substrate by sputtering in an UHV system. The CPW structure is defined by optical lithography, and the redundant metal is removed by reactive ion etching. Finally the resist is removed upside down in an acetone bath using sonication.
An SEM picture of a CPW resonator device can be seen in figure 8.1. The picture has been taken after measurement, as recognizable from the remaining bond wires at the edges and on both bond pads of the feedline, and from contaminations by water condensation. Many bond wires are used to achieve grounding of both sides of the ground plane. Three quarter wavelength resonators are coupled capacitively to the feedline differing only in the total length.
Potential devices are checked with an optical microscope for lithography errors, and the feedline is tested in a probe station whether it has unwanted electric contact to the ground planes. Further characterization is done employing a 4K dip stick.
For first CPW structures we employed Nb, a common material for superconducting transmission lines due to its high critical temperature. Figure 8.2 shows the measurement of the critical temperature for a 135 nm thick Nb layer; a critical temperature of $T_c = 8.925\,\mathrm{K}$ was achieved.
The width of the feedline is $w = 20\,\mu\mathrm{m}$, it is separated from the ground planes on both sides by $s = 12\,\mu\mathrm{m}$. The metallic layer for the CPW resonator is 135 nm thick. The values are chosen to achieve a $50\,\Omega$ matching of the feedline. The resonance frequency of a quarter wavelength resonator is defined by its length l_{cpw} and the properties of the substrate using

$$f_{\mathrm{design}} = \frac{c}{4 l_{\mathrm{cpw}} \sqrt{\epsilon_{\mathrm{eff}}}}; \tag{8.1}$$

where c is the speed of light and ϵ_{eff} the effective dielectric constant of the used substrate material. The three meandering resonators of figure 8.1 yield three different resonance frequencies due to their different lengths. For the Nb resonator we can calculate $\epsilon_{\mathrm{eff}} = 4.88$ [Chen and Chou, 1997]; it also turns out that the 10 nm thick Al_2O_3 layer can be neglected for calculating ϵ_{eff}. The details for this calculation are given in appendix D. Table 8.1 lists the lengths of the different resonators and the resulting resonance frequencies using equation 8.1. The design frequencies are chosen to fit to the experimental setup.

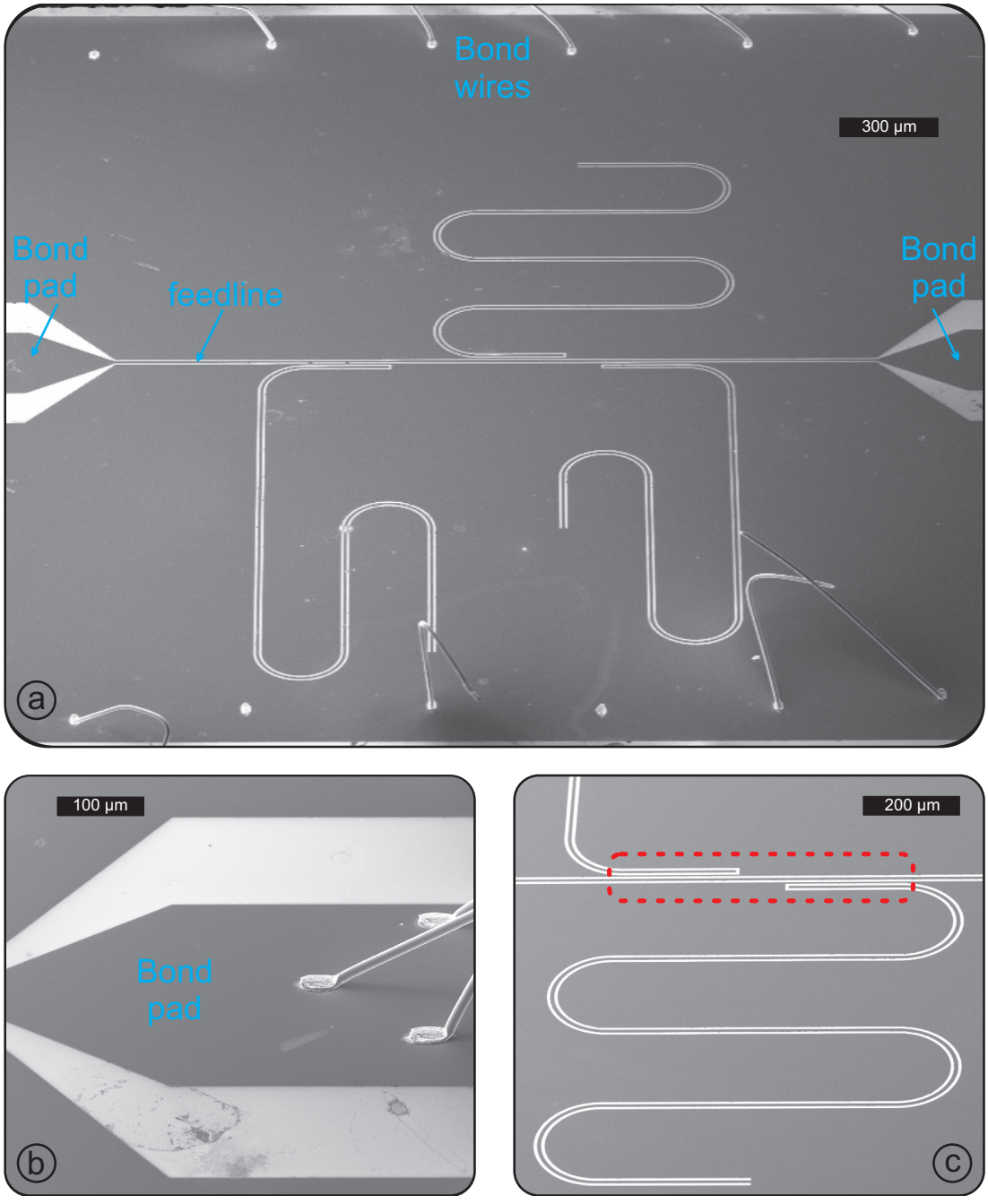

Figure 8.1: (a) SEM picture of an 8×8 mm substrate with a feedline connected to two bond pads and three superconducting CPW resonators. (b) shows a bond pad of the feedline. Three bond wires are used to achieve a good contact. In (c) a zoom of one meandering resonator is depicted. The region marked with red is responsible for the capacitive coupling of feedline and resonator(s).

	resonator length l_{cpw}	design frequency f_{design}
resonator 1	$l_{\mathrm{cpw}} = 6.604\,\mathrm{mm}$	$5.139\,\mathrm{GHz}$
resonator 2	$l_{\mathrm{cpw}} = 7.473\,\mathrm{mm}$	$4.541\,\mathrm{GHz}$
resonator 3	$l_{\mathrm{cpw}} = 8.062\,\mathrm{mm}$	$4.209\,\mathrm{GHz}$

Table 8.1: Lengths l_{cpw} of the meandering resonators and the resulting design frequencies f_{design} using equation 8.1 and a calculated value $\epsilon_{\mathrm{eff}} = 4.88$.

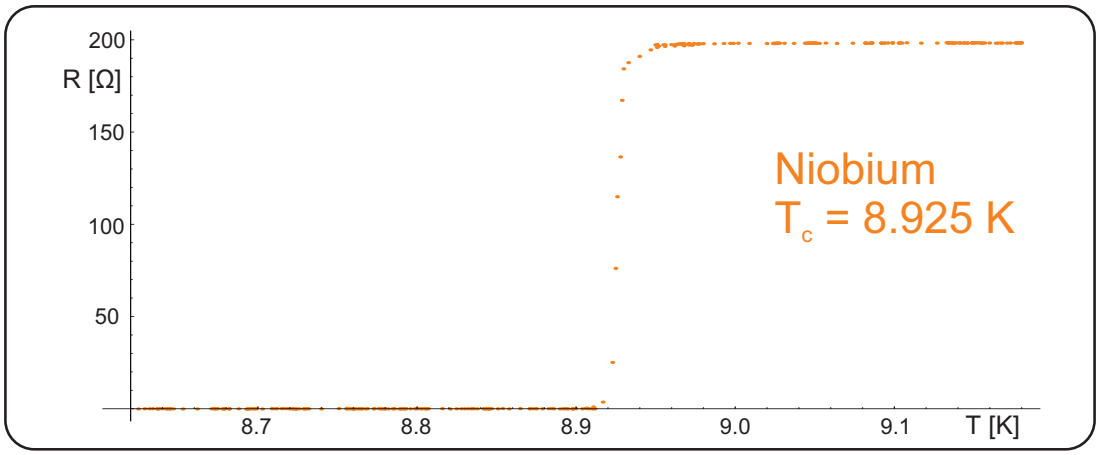

Figure 8.2: Four terminal measurement of Nb hall bar test structures. Recorded is the resistance as function of the temperature. The Nb test structure was etched in the ground plane of a 135 nm thick Nb resonator structure, after the resonator measurements. Nb shows a critical temperature $T_c = 8.925\,\mathrm{K}$. The measurement was done in cooperation with Thomas Huber.

8.2 Microwave frequency measurement setup

For the low temperature measurements the samples are mounted in a special sample holder, see figure 8.3. On the bottom of the mixing chamber of a dilution refrigerator a silver cold finger is attached. At the end of this finger the sample holder is placed.
In figure 8.4(a) a photo of our dilution system is depicted; the fundamental cooling process was already presented in chapter 3. For high frequency (HF) measurements an ingoing and an outgoing HF coaxial cable is installed within the cryostat. The high frequency setup is sketched in figure 8.4(b). For cooling of the ingoing cable several attenuators are installed and thermally coupled to the different temperature stages, adding up to an input attenuation of 53 dB. In the output signal cable instead a high electron mobility transistor (HEMT) amplifier of type Caltech CITCRYO1-12A is installed working at the 1 K stage, see figure 8.5. For a proper thermal contact a copper strip links the HEMT amplifier to the 1K-plate. The amplifier is battery driven and has a gain of 29 dB. Also shown in figure 8.5 is a circulator mounted at the mixing chamber plate. It is used to prevent heating from the direction of the HEMT amplifier and reduces noise.
Measurements were done using on the one hand a vector network analyzer and on the other hand a combination of a signal generator and a spectrum analyzer.

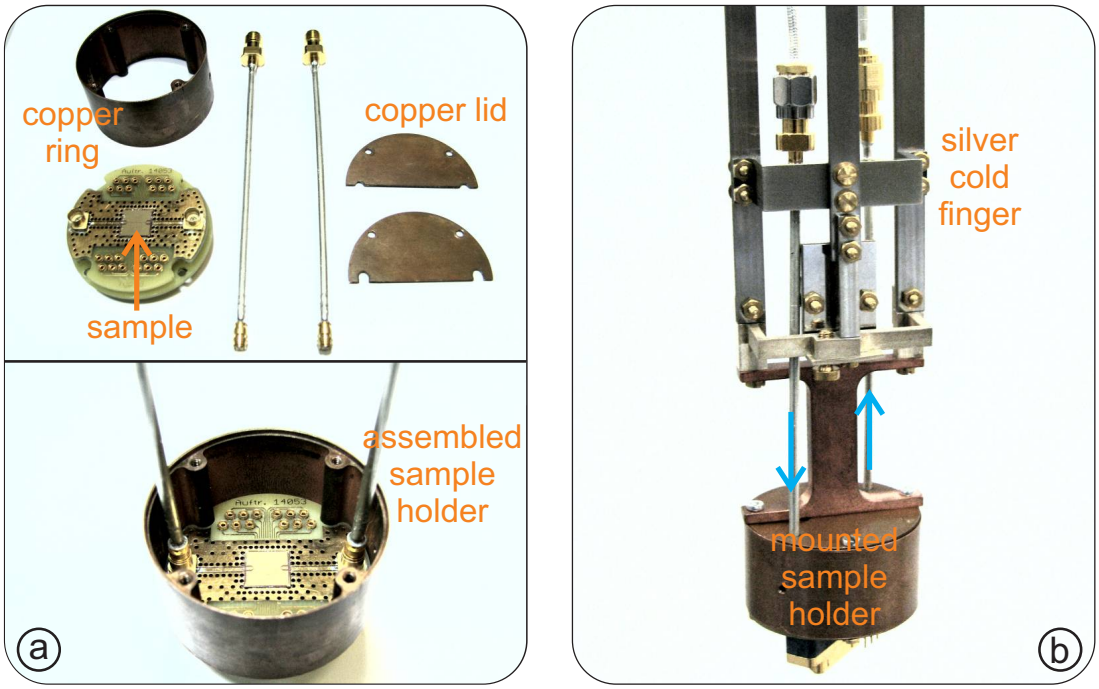

Figure 8.3: (a) shows the single parts of the sample holder, (b) the assembled and mounted sample holder at the end of the cold finger.

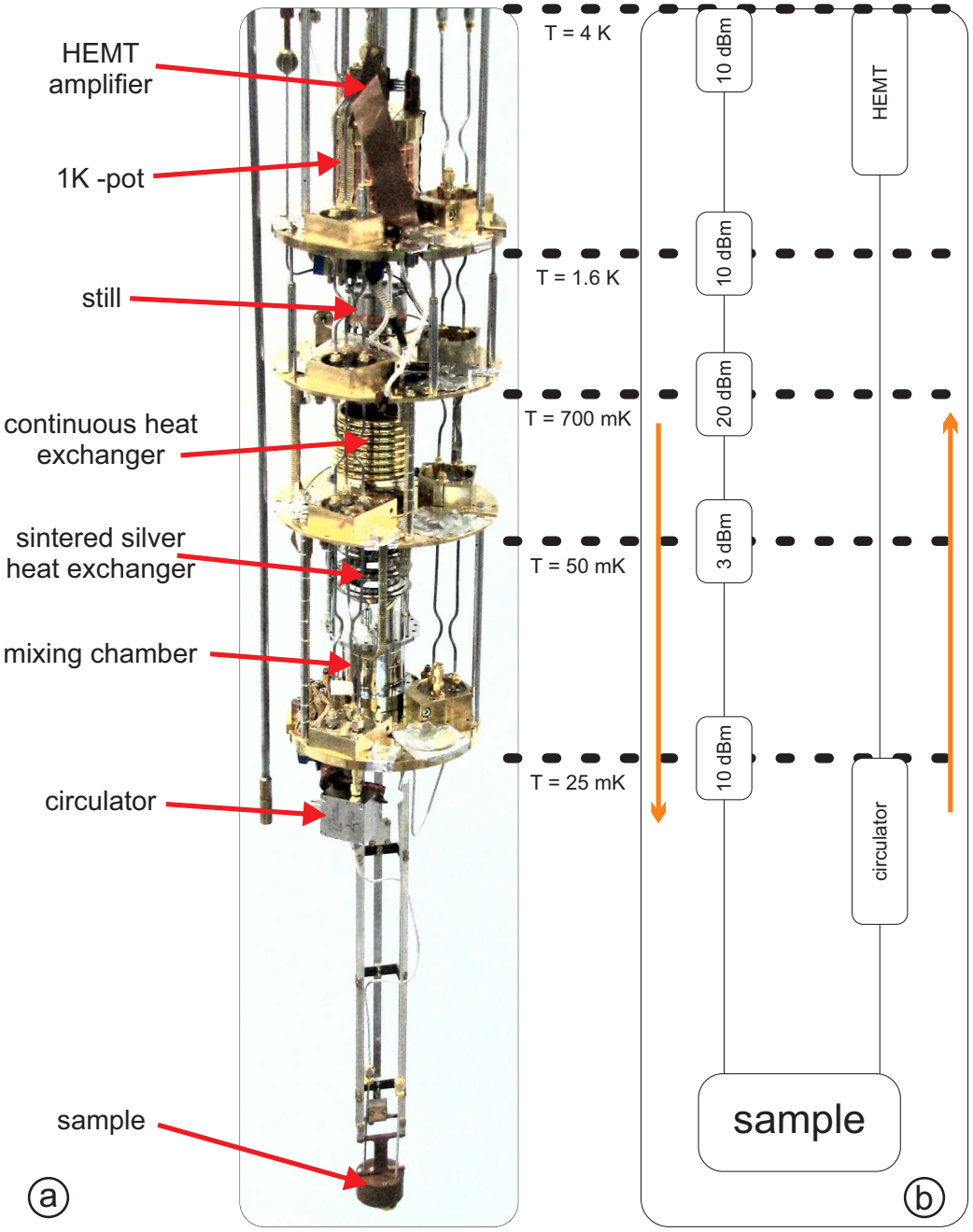

Figure 8.4: (a) Photo of our dilution system; marked are the parts responsible for the cooling process. The sample is mounted at the end of a cold finger assembly. (b) Microwave cabling installed in the cryostat for RF transmission measurements. On the input side the coaxial cable is thermalized using impedance matched attenuators; the total attenuation is 53 dB. On the output side a circulator is mounted at the mixing chamber plate and the HEMT pre-amplifier near the 1K-pot with a gain of 29 dB.

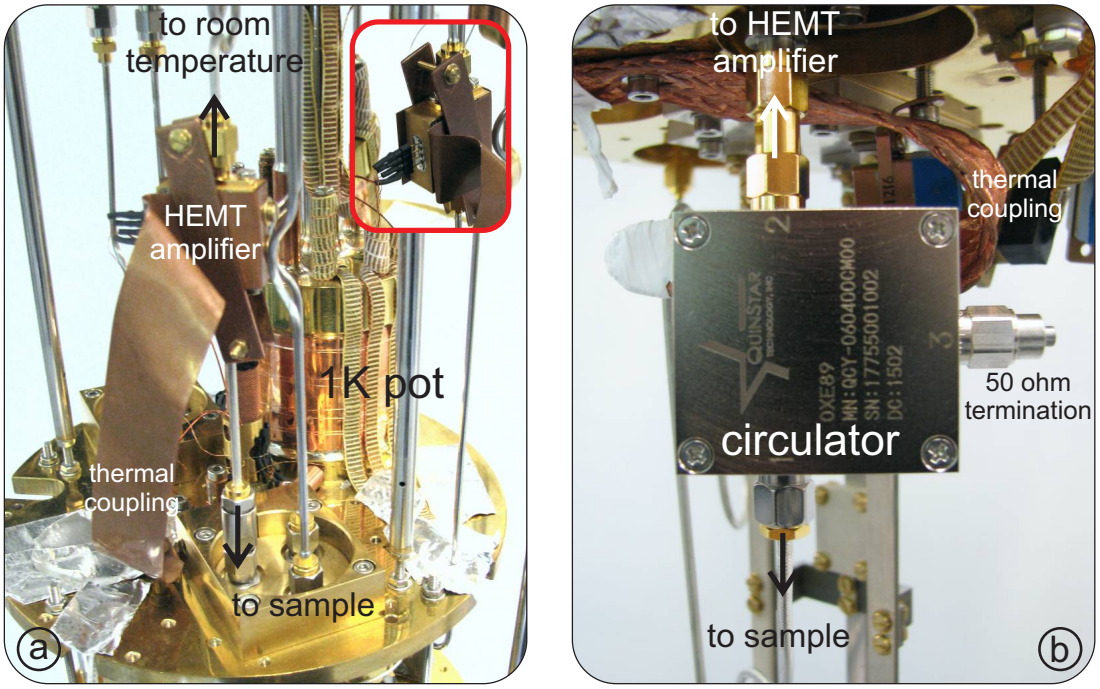

Figure 8.5: (a) shows the attached and thermally coupled HEMT amplifier. It is located at the 1K-plate; the small insert shows the power supply cables of the HEMT amplifier. The circulator at the mixing chamber is shown in (b).

8.3 Quality factor evaluation

For CPW devices it is convenient to use the scattering matrix formalism to describe the transmission through the feedline of a quarter wavelength resonator [Pozar, 2012]; amplitude and phase angle of the outgoing wave are measured with respect to the incident microwave. For a two-port device we have the scattering matrix

$$\begin{pmatrix} V_1^{\text{out}} \\ V_2^{\text{out}} \end{pmatrix} = \begin{pmatrix} S_{11} & S_{21} \\ S_{21} & S_{22} \end{pmatrix} \cdot \begin{pmatrix} V_1^{\text{in}} \\ V_2^{\text{in}} \end{pmatrix}, \tag{8.2}$$

where the parameter S_{21} is of main interest. $V_i^{\text{out}}/V_i^{\text{in}}$ describe the voltage output and input at port i; S_{ij} is the scattering matrix element from port j to port i. Sweeping the frequency we expect a dip at a certain frequency since in resonance case an amount of power is coupled out to the resonant quarter wavelength structure. The combination of meandering resonators and the feedline can be treated as parallel lumped element RLC circuits [Pozar, 2012]. Following [Khalil et al., 2012, Bruno et al., 2015] the frequency dependence of S_{21} near resonance can be described by

$$S_{21} = 1 - \frac{e^{i\theta} Q_l}{|Q_e| \left(1 + 2i\delta \mathrm{f} Q_l\right)}, \tag{8.3}$$

with

$$\delta \mathrm{f} = \frac{f - f_0}{f_0}, \tag{8.4}$$

where Q_l is the loaded quality factor, Q_e the external quality factor and the angle θ is introduced to model an asymmetric line shape of the resonance feature; for details see [Khalil, 2013].
Using equation 8.3 for fitting our measurement data it turns out that we have to add an additional linear equation to compensate the asymmetric line shape of S_{21}. Note that the angle θ accounts for an asymmetric line shape only near resonance; the linear equation results in an overall tilt of the whole measured frequency range.
Figure 8.6 shows an example measurement of the transmission $|S_{21}|^2$ as a function of the applied microwave frequency at base temperature of the dilution system. A clear dip around $f_{\mathrm{res}} = 4.2159\,\mathrm{GHz}$ arises due to the resonant coupling of the meandering resonator structure and the feedline. The orange dots represent the measured data, and the blue curve represents the fit, yielding a loaded quality factor $Q_l = 9424.55$ and an external quality factor $|Q_e| = 9798.16$. Using the definition for the coupling quality factor

$$Q_c^{-1} = Re\left(Q_e^{-1}\right), \tag{8.5}$$

we obtain $Q_c = 9796.68$ and so one can derive the internal quality factor of the quarter wavelength resonator, which describes the intrinsic loss of the resonator:

$$Q_i = \frac{1}{\frac{1}{Q_l} - \frac{1}{Q_c}}. \tag{8.6}$$

For this device we found an internal quality factor $Q_i = 2.42 \cdot 10^5$; compared to literature this internal quality factor is in the same order of magnitude: in [Baselmans et al., 2005] a 100 nm thick Nb quarter wavelength resonator is employed achieving internal quality factors ranging from $Q_i = 3.4 \cdot 10^4$ to $Q_i = 2.7 \cdot 10^5$. In a more recent experiment by [Macha et al., 2010] internal quality factors of $Q_i = 5.7 \cdot 10^5$ for a Nb half wavelength resonator were presented. In the following we present additional measurements and evaluation of the resonance frequency and internal quality factor of our Nb CPW resonator.

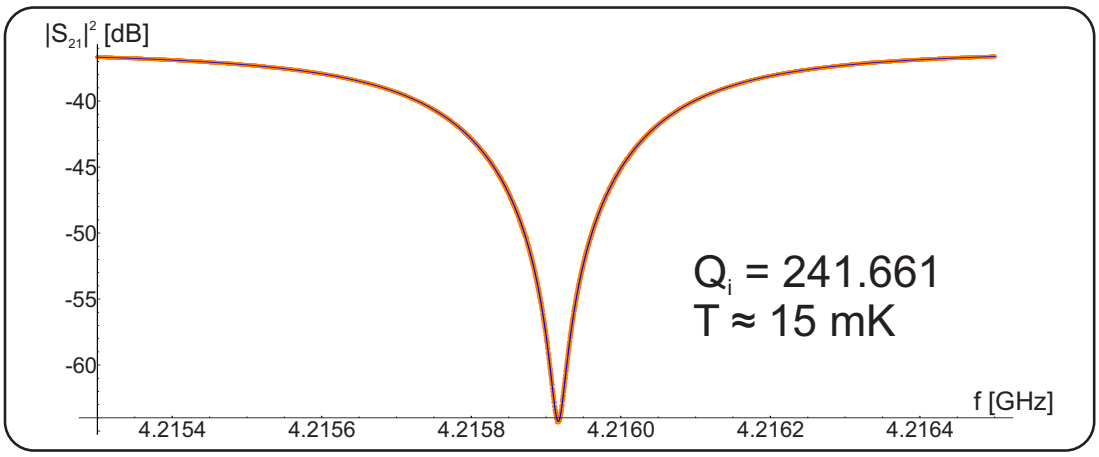

Figure 8.6: $|S_{21}|^2$ transmission matrix element as a function of the applied microwave frequency. A dip around $f_{\mathrm{res}} = 4.2159\,\mathrm{GHz}$ arises, using equation 8.6 (solid curve) we obtain an internal quality factor of $Q_i = 2.42 \cdot 10^5$. This measurement was done at base temperature of the dilution system.

8.4 Characterization of niobium quarter wavelength resonators

For a first characterization we measured the device at 4 K in a ^{4}He transport vessel; it is surrounded by liquid helium. In figure 8.7 the transmission $|S_{21}|^2$ is plotted as a function of the applied microwave frequency, at an input power $P_{\mathrm{generator}} = -20\,\mathrm{dBm}$. Three minima of different magnitude arise; slow, periodic oscillations in the transmission can be attributed to intrinsic resonances due to the cables.
Table 8.2 lists the measured resonance frequencies and the design frequencies for this CPW. A systematic deviation of about 7.5 % arises. In equation 8.1 the resonance frequency is assumed to be temperature independent; tentatively assuming that this deviation is due to a kinetic inductance of the superconducting metal. The details of the temperature dependence will be discussed later.

Subsequently the device was cooled down using our dilution system, see section 8.2. For further examination, the resonance feature at 4.21 GHz was chosen. A first measurement at base temperature was already shown in figure 8.6. This has been repeated at several temperatures; the internal quality factors Q_i and resonance frequencies f_{res} were extracted using equation 8.3 and equation 8.6. The generator power was set to $P_{\mathrm{generator}} = 0\,\mathrm{dB}$, leading to a effective power arriving at the sample of $P_{\mathrm{in}} = P_{\mathrm{generator}} - 53\,\mathrm{dB}$.
In figure 8.8 several measurements of the transmission $|S_{21}|^2$ are compared for temperatures ranging from 18 mK to 3.63 K. The resonance frequency decreases for increasing temperatures. One also sees that the resonance peaks broaden and

	design frequency f_{design}	resonance frequency f_{res}	deviation
resonator 1	5.139 GHz	4.748 GHz	7.61 %
resonator 2	4.541 GHz	4.203 GHz	7.44 %
resonator 3	4.209 GHz	3.905 GHz	7.22 %

Table 8.2: Listed are the different resonance frequencies f_{res} extracted from figure 8.7 and design frequencies f_{design}. A systematic deviation of about 7.5 % is observed, see text.

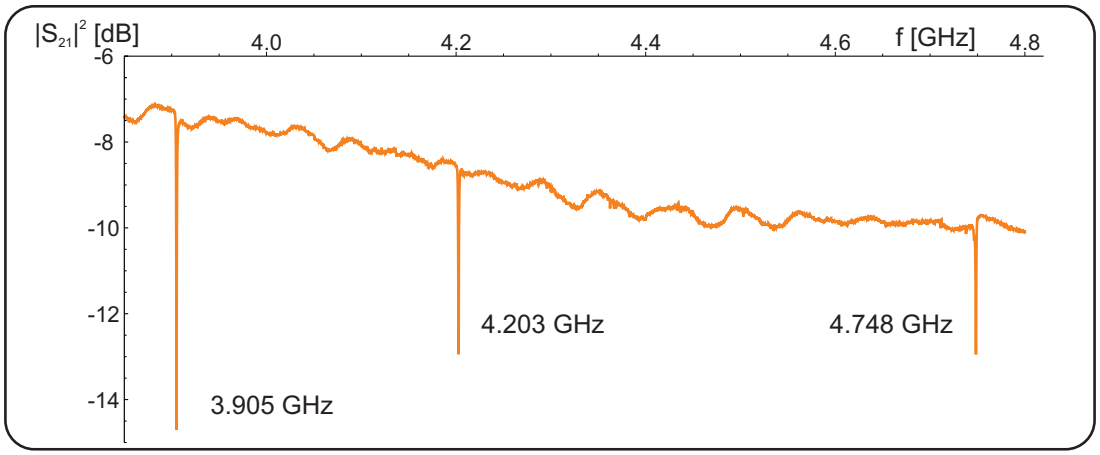

Figure 8.7: Transmission matrix element $|S_{21}|^2$ as a function of the frequency varied from 3.85 GHz to 4.8 GHz. The input power was set to $P_{\text{generator}} = -20$ dB. The resonance features are clearly visible. Three dips at 3.905 GHz, 4.203 GHz and 4.748 GHz arise. The measurement was done in cooperation with Thomas Huber at liquid helium temperature employing a 4K dipstick.

the depth of the peaks decreases from about 28 dB for 18 mK to about 8 dB for 3.63 K.
Figures 8.9 and 8.10 display the evaluation results of the temperature dependence of Q_i and f_{res}, respectively. As can be seen in figure 8.9, the internal quality factor of our Nb resonator slightly increases up to 300 mK. Above $T = 300$ mK the internal quality factor decreases to a value of Q_i=7868.88 at 4.4 K.
In figure 8.10(a) we observe a slight increase of the resonance frequency f_{res} up to 1.5 K. For further increasing temperatures the resonance frequency drops, compare figure 8.10(b).
In literature, the low temperature behavior of Q_i and f_{res} is attributed to the loss due to two-level systems (TLS) in the substrate. Tunnel systems in the substrate interact with the electro-magnetic field of the CPW resonator. The effect for low temperatures is small compared to the decrease at higher temperatures. There, the cooper-pair density of the superconducting material decreases and the kinetic inductance rises, leading to the strong drop of the resonance frequency for temperatures above $T = 2.5$ K. The corresponding models will be discussed in detail in the following sections.

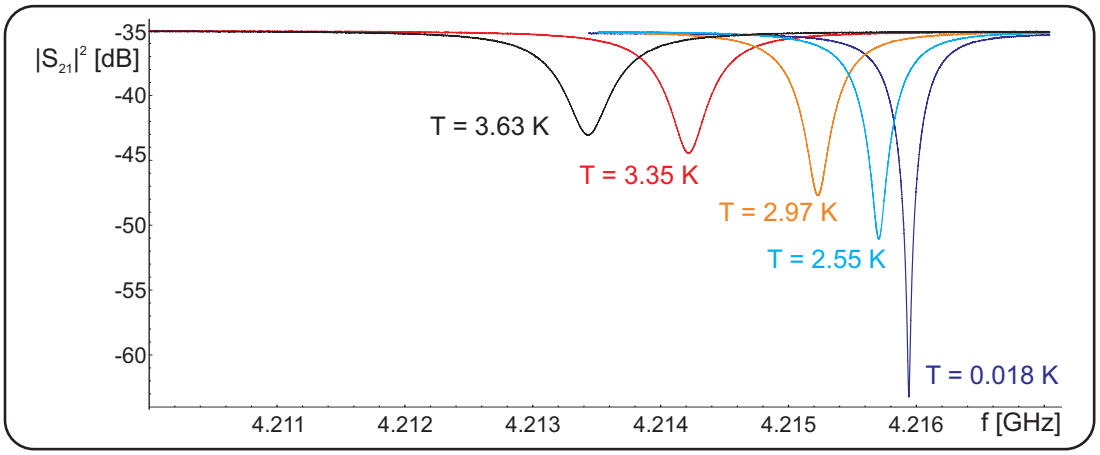

Figure 8.8: Plotted are the $|S_{21}|^2$ transmission measurements for different temperatures of a Nb resonator. The resonance features shift to lower frequencies; the magnitude decreases for higher temperatures.

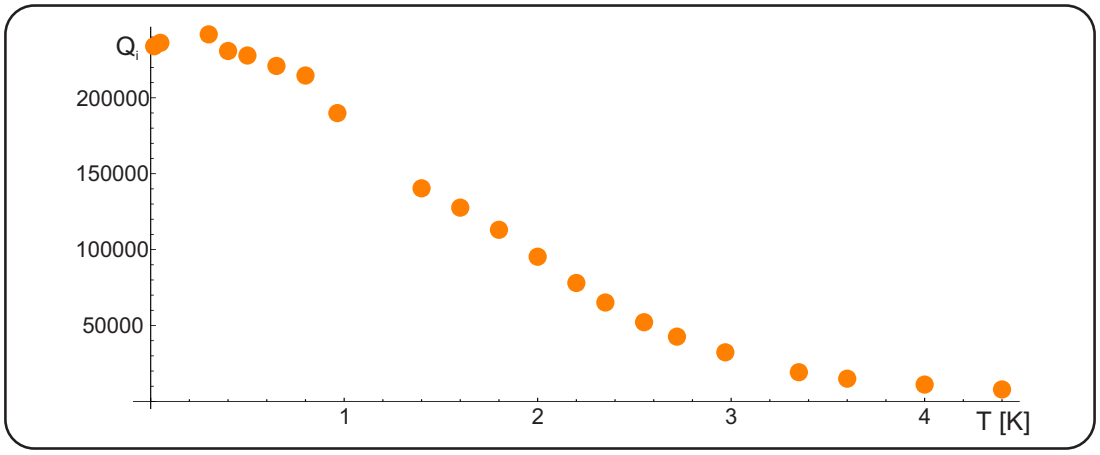

Figure 8.9: Internal quality factor Q_i as a function of the temperature for our Nb resonator. For each data point a $|S_{21}|^2$ measurement is performed and equation 8.6 is used to provide the fit parameters.

8.5 Two-level system loss in coplanar waveguides

Model

The low temperature behavior of superconducting CPWs shown in the last section can be modeled using a two-level system (TLS) model. A first discussion of TLS in amorphous solids is given in [Anderson et al., 1972, Phillips, 1972] trying to explain the experimental distinctions between crystalline and amorphous solids at low temperatures. The basic idea is atoms being present in the amorphous solid having multiple potential minima.
TLS in solids give rise to an extremely wide field of low temperature physics; e.g. the specific heat or the thermal conductivity are strongly influenced by TLS in amorphous dielectrica and even crystalline materials. A detailed discussion can be found in [Phillips, 1987] and [Enss and Hunklinger, 2005]. Tunneling states of atoms in disordered solids cause dipole moments which, in our case couple to the electro-magnetic field of the CPW resonator. For a detailed formalism transformed from the original amorphous solids to CPW resonators it is referred to [Gao, 2008]; here only a short overview is given.
The two-level system is modeled as a double potential well using the Hamiltonian

$$H_0 = \frac{1}{2} \cdot \begin{pmatrix} -\Delta_{\mathrm{TLS}} & \Delta_0 \\ \Delta_0 & \Delta_{\mathrm{TLS}} \end{pmatrix}, \tag{8.7}$$

with the TLS asymmetry Δ_{TLS} and the tunnel splitting Δ_0.

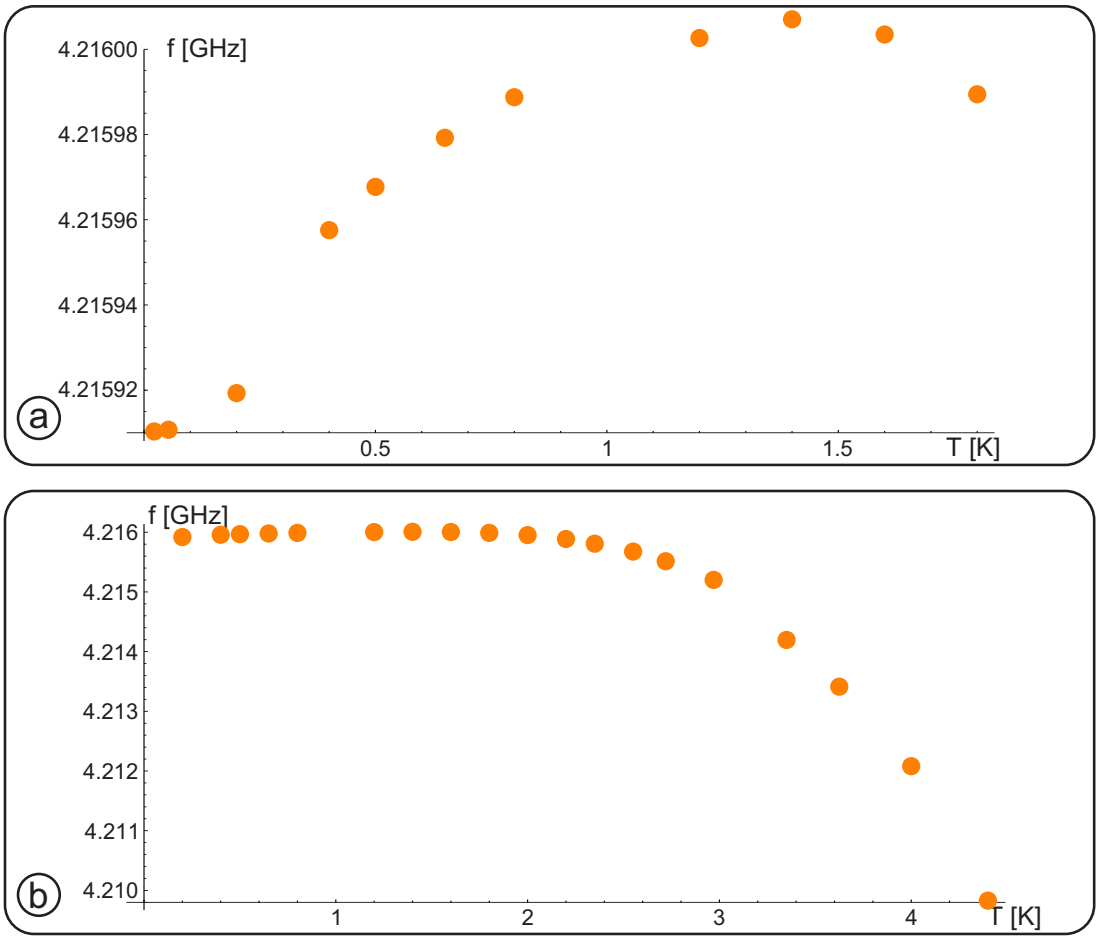

Figure 8.10: Extracted resonance frequencies as a function of the temperature of the Nb quarter wavelength resonator. For each data point a $|S_{21}|^2$ measurement is done and equation 8.3 is used to extracted the resonance frequency. (a) Details of the low temperature region ($T < 2\,\mathrm{K}$); an increasing resonance frequency for increasing temperature is visible below $T = 1.3\,\mathrm{K}$.

The eigenenergies of this Hamiltonian read

$$\epsilon = \pm \frac{\sqrt{\Delta^2 + \Delta_0^2}}{2}. \tag{8.8}$$

The interaction of the TLS with the electromagnetic field of the superconducting microwave resonator is included by an additional term H_i in the Hamiltonian:

$$H = H_o + H_i = \frac{1}{2}\epsilon\sigma_z + \left[\frac{\Delta_{\mathrm{TLS}}}{\epsilon}\sigma_z + \frac{\Delta_0}{\epsilon}\sigma_x\right]\vec{d_0}\cdot\vec{E}, \tag{8.9}$$

where σ_i are the Pauli matrices and $\vec{d_0}$ is the maximum transition dipole moment for a corresponding energy ϵ. The first term of the interaction Hamiltonian including the TLS asymmetry Δ_{TLS} is responsible for a relaxation response in the electro-magnetic field of the CPW resonator. The tunnel splitting Δ_0 gives rise for a resonant response; second term in equation 8.9. One can define a resonant and relaxation tensor for the susceptibility connecting the dipole moment of the TLS and the electro-magnetic field of the CPW resonator:

$$\vec{d} = \xi_{\mathrm{res,rel}}\cdot\vec{E}, \tag{8.10}$$

for the complete expressions see appendix D. For microwave frequencies it turns out that the relaxation contribution has not to be taken into account. So one obtains for the dielectric function

$$\epsilon_{\mathrm{TLS}}(\omega) = \int\int\int\left[(\vec{e}\cdot\xi_{res}\cdot\vec{e})\frac{P_{\mathrm{TLS}}}{\Delta_0}\right]\mathrm{d}\Delta_{\mathrm{TLS}}\mathrm{d}\Delta_0\mathrm{d}\widehat{d} = \epsilon'_{\mathrm{TLS}}(\omega) - i\cdot\epsilon''_{\mathrm{TLS}}(\omega), \tag{8.11}$$

where P_{TLS} is the density of states of the TLS. The integration is done over the tunnel asymmetry Δ_{TLS}, the tunnel splitting Δ_0, and the dipole orientation $\widehat{d}$. Within the tunneling model it is assumed that Δ_{TLS} and Δ_0 are independent of each other and their distribution is uniform [Enss and Hunklinger, 2005]. A detailed analysis of ϵ_{TLS} is given in [Gao, 2008]. Following [Pozar, 2012] one can calculate the shift of the resonance frequency and the internal quality factor caused by TLS; the results are

$$\frac{f(T)-f_0}{f_0} = -\frac{\int_{V_h}\epsilon'_{\mathrm{TLS}}|\vec{E}|^2\mathrm{d}\vec{r}}{2\int_V\epsilon_{\mathrm{eff}}|\vec{E}|^2\mathrm{d}\vec{r}} = \frac{F\delta_{\mathrm{TLS}}}{\pi}\left[Re\Psi\left(\frac{1}{2}-\frac{hf_0}{2i\pi k_BT}\right) - \mathrm{Log}\left(\frac{hf_0}{2\pi k_BT}\right)\right] \tag{8.12}$$

and

$$\frac{1}{Q_i} = -\frac{\int_{V_h} \epsilon''_{\mathrm{TLS}} |\vec{E}|^2 \mathrm{d}\vec{r}}{2 \int_V \epsilon_{\mathrm{eff}} |\vec{E}|^2 \mathrm{d}\vec{r}} = F\delta_{\mathrm{TLS}} \tanh\left(\frac{hf(T)}{2k_B T}\right). \tag{8.13}$$

The only free parameters are $F\delta_{\mathrm{TLS}}$ and f_0; Ψ is the complex digamma function, see appendix D. The integration in the numerator is done over the volume V_h of the TLS host material; the integration in the denominator is done over the volume of the electro-magnetic field V. δ_{TLS} represents the loss tangent caused by the TLS and f_0 is the resonance frequency for a temperature $T = 0\,\mathrm{K}$. F is given by the ratio of the stored energy in TLS host material and the total stored energy of the microwave resonator. The total internal quality factor for low temperatures and a strongly driven signal reads:

$$\frac{1}{Q_i} = F\delta^*_{\mathrm{TLS}} \tanh\left(\frac{hf(T)}{2k_B T}\right) + \frac{1}{Q_{\mathrm{other}}}. \tag{8.14}$$

with an effective, reduced loss tangent $F\delta^*_{\mathrm{TLS}}$ due to partial saturation of TLS [Singh et al., 2014, Götz et al., 2015]. The first term of equation 8.14 is referred to a TLS-dominated internal quality factor; an additional term Q_{other} is added to account for dissipation that is not connected to TLS [Bruno et al., 2015].

Temperature dependence

The cyan curve in figure 8.11(a) represents the fit using equation 8.12; for temperatures above 1 K the increase of the resonance frequency is weaker than predicted by the TLS model. For temperatures above 1.5 K the model fails since the resonance frequency now decreases for increasing temperature; this is an effect of the lower cooper-pair density, see section 8.6. For temperatures below 100 mK the model curve also exhibits an again increasing resonance frequency. The curve of equation 8.12 fits well to our data points. We can extract $F\delta_{\mathrm{TLS}} = 4.189 \cdot 10^{-5}$ and a value $f_0 = 4.216\,\mathrm{GHz}$.
Placing this into perspective, in [Sage et al., 2011] measurements on half wavelength CPW resonators are presented; different metallic layers and substrate systems are used to study the loss mechanism in CPWs. They also tested an 200 nm Nb/SiO^2/Si resonator obtaining a value $F\delta_{\mathrm{TLS}} = 2.4 \cdot 10^{-5}$, this is nearly the same value we could extract from our Nb quarter wavelength resonator. In a more recent publication, a value $F\delta_{\mathrm{TLS}} = 1.15 \cdot 10^{-5}$ for a 160 nm Nb quarter wavelength resonator on a high resistive silicon substrate was presented [Wang et al., 2013]. In table 8.3 our results are compared to the literature.
The fit curve for the internal quality factor is marked cyan in figure 8.11(b), we

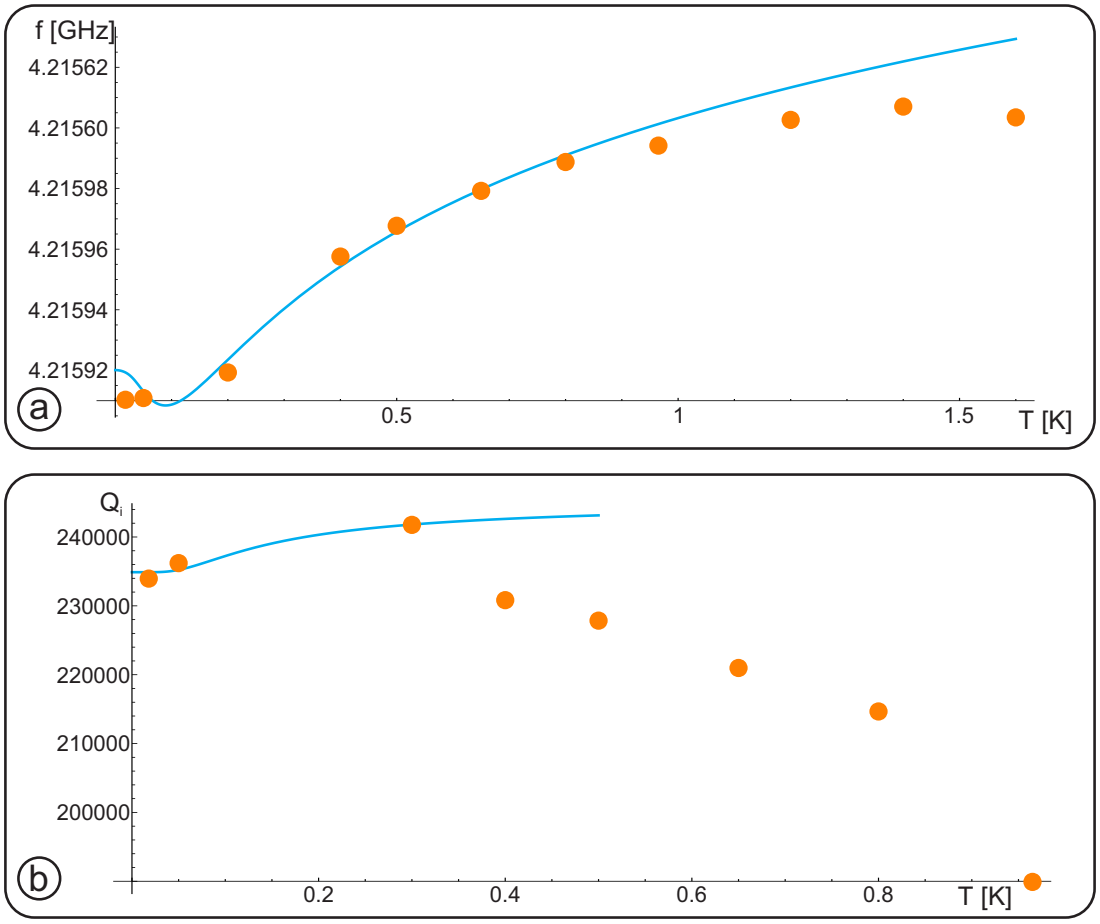

Figure 8.11: Data points: extracted resonance frequency (a) and internal quality factor (b) as a function of temperature for the Nb resonator, same as in figure 8.9 and figure 8.10. The cyan curves represent fits using equation 8.12 for (a) and equation 8.14 for (b). Both equations achieve a quite good agreement with our data, although we have only few data points for low temperature.

can extract $k^* = F\delta^*_{\mathrm{TLS}} = 1.806 \cdot 10^{-7}$, which is about 100 times smaller than $k = F\delta_{\mathrm{TLS}}$ and $Q_{\mathrm{other}} = 245293$.

Power dependence

We have measured the power dependence of the TLS loss $F\delta_{\mathrm{TLS}}$ in a second Nb CPW device, fabricated identically to the first one. In figure 8.12 the resonance frequency is measured as a function of the temperature for four different nominal input powers $P_{\mathrm{in}} = P_{\mathrm{generator}} - 53\,\mathrm{dB}$. $F\delta_{\mathrm{TLS}}$ is obtained using equation 8.12 for each input power P_{in}. For low input powers ($P_{\mathrm{in}} = -63\,\mathrm{dB}$ and $P_{\mathrm{in}} = -53\,\mathrm{dB}$) the TLS loss is nearly constant; $F\delta_{\mathrm{TLS}} = 4.46 \cdot 10^{-5}$ and $F\delta_{\mathrm{TLS}} = 4.45 \cdot 10^{-5}$. Increasing the input power decreases the TLS loss; $F\delta_{\mathrm{TLS}} = 4.19 \cdot 10^{-5}$ for

	Our device	[Sage et al., 2011]	[Sage et al., 2011]	[Wang et al., 2013]
CPW type	$\lambda/4$ CPW	$\lambda/2$ CPW	$\lambda/2$ CPW	$\lambda/4$ CPW
CPW material	135 nm niobium	200 nm niobium	200 nm niobium	160 nm niobium
substrate	550 nm SiO_2 (dry grown)	500 nm SiO_2 (wet grown)	high-ρ Si	500 µm high-ρ Si
	500 µm high-ρ Si	high-ρ Si		
$F\delta_{\mathrm{TLS}}$	$4.189 \cdot 10^{-5}$	$2.4 \cdot 10^{-5}$	$1.5 \cdot 10^{-5}$	$1.15 \cdot 10^{-5}$

Table 8.3: Listed are our results obtained from the low temperature dependence of the resonance frequency. In addition the experiments mentioned in the text are shown.

$P_{\text{in}} = -43\,\text{dB}$ and $F\delta_{\text{TLS}} = 3.42 \cdot 10^{-5}$ for $P_{\text{in}} = -33\,\text{dB}$. The TLS get saturated at higher electro-magnetic fields in the CPW resonators; thus the absorption becomes less and the TLS loss decreases. The temperature dependence of the resonance frequency (below $T = 200\,\text{mK}$) changes with increased input power P_{in}. For $P_{\text{in}} = -63\,\text{dB}$ the resonance frequency increases below 100 mK (marked green in figure 8.12), this increase is weaker for a input power $P_{\text{in}} = -53\,\text{dB}$. For $P_{\text{in}} > -43\,\text{dB}$ the increase of the resonance frequency below 100 mK can not be observed.

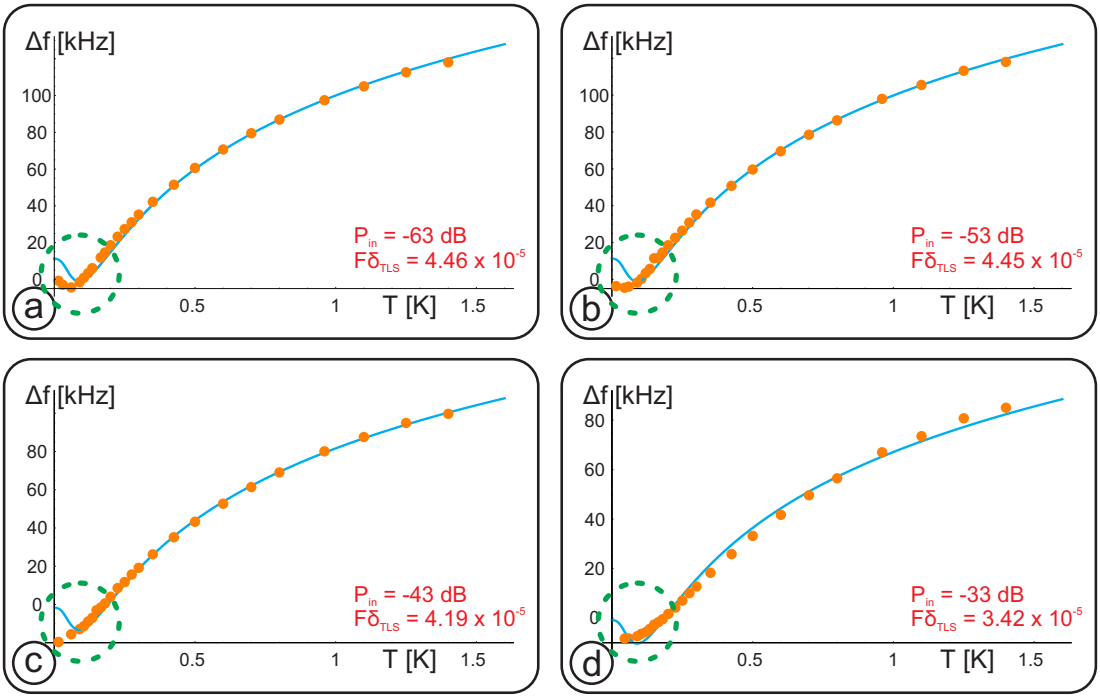

Figure 8.12: Temperature dependence of resonance frequency for a second Nb CPW resonator. Plotted is the shift of the frequency $f - f_0$ as a function of the temperature. The measurements are taken for four different nominal input powers P_{in} ranging from -63 dB to -33 dB. The extracted values for the TLS loss $F\delta_{\text{TLS}}$ are labeled for each nominal input power. The frequency behavior for temperatures below 100 mK changes due to the increasing nominal input power (green cycles), see text.

8.6 Matthis Bardeen theory for coplanar waveguides

The temperature dependence of the resonance frequency below $T = 1\,\mathrm{K}$ is well described by the TLS model of the previous section. For higher temperature T the decrease of the resonance frequency can be attributed to a decrease in the superfluid density of the superconducting metal [Singh et al., 2014, Götz et al., 2015]. The resonance frequency then reads:

$$\frac{f(T) - f_0}{f_0} = \frac{\alpha\delta\sigma_2}{2\sigma_2}, \tag{8.15}$$

where σ_2 is the imaginary part of the complex conductivity σ and α is the kinetic inductance fraction. The BCS energy gap Δ_{BCS} can be calculated [Hinken, 1988]:

$$\Delta_{\mathrm{BCS}} = \Delta_{T=0}\sqrt{\cos\left(\frac{\pi T^2}{2T_c^2}\right)}; \tag{8.16}$$

with an expression for $\Delta_{T=0}$ [Tinkham, 2004]:

$$\Delta_{T=0} = 1.764 k_B T_c. \tag{8.17}$$

For $hf << \Delta_{T=0}$ and $k_B T << \Delta_{T=0}$ one obtains for σ_2 [Gao et al., 2008]:

$$\frac{\sigma_2}{\sigma_n} = \frac{\pi\Delta_{\mathrm{BCS}}}{hf_0}\left[1 - 2e^{-\frac{\Delta_{\mathrm{BCS}}}{k_B T}} e^{-\frac{hf_0}{2k_B T}} I_0\left(\frac{hf_0}{2k_B T}\right)\right]; \tag{8.18}$$

I_0 is the modified Bessel function of the first kind and σ_n is the normal state conductivity. For the internal quality factor we obtain:

$$\delta\left(\frac{1}{Q_i}\right) = \frac{\alpha\delta\sigma_1}{\sigma_2}, \tag{8.19}$$

where σ_1 is the real part of the complex conductivity σ [Gao et al., 2008]:

$$\frac{\sigma_1}{\sigma_n} = \frac{4\Delta_{\mathrm{BCS}}}{hf_0} e^{-\frac{\Delta_{\mathrm{BCS}}}{k_B T}} \sinh\left(\frac{hf_0}{2k_B T}\right) K_0\left(\frac{hf_0}{2k_B T}\right); \tag{8.20}$$

with K_0 as a modified Bessel function of the second kind. In figure 8.13 the cyan curves represent the fits using equations 8.15 and 8.19. Here α is used as a free fit parameter. Fitting the temperature dependence of the resonance frequency yields a value of $\alpha_{\mathrm{exp}} = 0.0291$. Our data points are in good agreement with the fit obtained form equation 8.15. The value $\alpha_{\mathrm{exp}} = 0.0291$ is now used to plot the temperature dependence of the internal quality factor Q_i. Figure 8.13(b) shows $Q_i(T)$, using equation 8.19 and $Q_0 = 2.35 \cdot 10^5$, the value obtained for Q_i at base temperature of the dilution system. Above $T = 2.5\,\mathrm{K}$ and below $T = 0.5\,\mathrm{K}$ the fitting curve can reproduce the experimentally obtained temperature dependence of the internal quality factor. At 0.8 K the internal quality factor Q_i decreases with increasing temperature, although an exponential drop of the internal quality factor Q_i is predicted only at about 1.6 K by the theoretical curve.

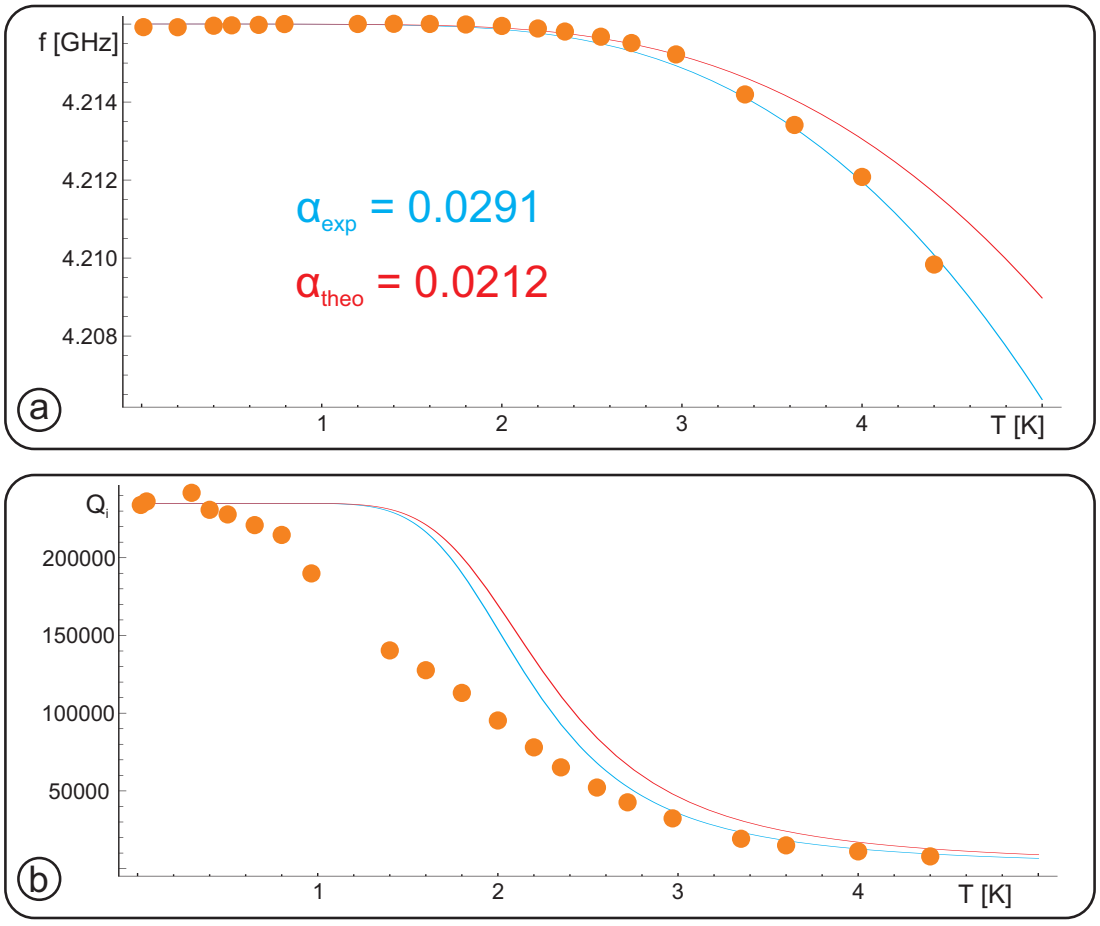

Figure 8.13: (a) Fit of the temperature dependence of the resonance frequency using equation 8.15 obtaining a value $\alpha_{\mathrm{exp}} = 0.0291$ (cyan curve). The red curve represents the theoretical curve using $\alpha_{\mathrm{theo}} = 0.0212$, see text. The curve of the temperature dependence of the internal quality factor Q_i is plotted for both α_{exp} (cyan curve) and α_{theo} (red curve) (b).

8.7 Calculating the kinetic inductance fraction

In the previous section, the kinetic induction fraction α_{exp} was obtained by fitting our experimental data. A theoretical value of the kinetic inductance can be calculated employing the properties of the geometry of the CPW resonator and the superconducting metal film. The kinetic inductance fraction can be written as [Watanabe et al., 1994]:

$$\alpha = \frac{L_k}{L_k + L_m}, \tag{8.21}$$

where L_k is the kinetic inductance per unit length and L_m the magnetic inductance per unit length of the superconducting CPW resonator film. The magnetic inductance is defined as [Collin, 1992]

$$L_m = \frac{\mu_0 K(k')}{4K(k)}, \tag{8.22}$$

where $K(x)$ is complete elliptic integral of the first kind. The kinetic inductance reads

$$L_k = L_s \left(g_{\mathrm{g}} + g_{\mathrm{f}}\right), \tag{8.23}$$

where L_s is the surface inductance and g_{g} and g_{f} are geometrical factors for ground plane and feedline. These depend on the size of feedline w, gap between feedline and ground plane s, and on the thickness z of the superconducting film:

$$g_{\mathrm{g}} = \frac{k}{4w\left(1-k^2\right)K(k)^2}\left[\pi + \ln\left(\frac{4\pi\left(w+2s\right)}{z}\right) - \frac{1}{k}\ln\left(\frac{1+k}{1-k}\right)\right], \tag{8.24}$$

$$g_{\mathrm{f}} = \frac{1}{4w\left(1-k^2\right)K(k)^2}\left[\pi + \ln\left(\frac{4\pi w}{z}\right) - k\ln\left(\frac{1+k}{1-k}\right)\right]. \tag{8.25}$$

A complete derivation of the geometrical factors using a conformal mapping technique is given in [Collin, 1992]. The surface inductance L_s reads [Gao, 2008]

$$L_s = \frac{1}{\sigma_2 \omega z}; \tag{8.26}$$

using equation 8.18 and assuming $T = 0$ the surface inductance can be written as

$$L_s = \frac{h}{\sigma_n 2\pi^2 \Delta_{T=0} z}. \tag{8.27}$$

The critical temperature $T_c = 8.925\,\mathrm{K}$ and the normal state conductivity $\sigma_n = 1.535 \cdot 10^7\,\Omega^{-1}m^{-1}$ lead to a kinetic inductance fraction $\alpha_{\mathrm{theo}} = 0.0212$. Compared to the value obtained by fitting our experimental data $\alpha_{\mathrm{exp}} = 0.0291$, this is in good agreement. Deviations arise due to the uncertainty in the geometrical values of the CPW resonator and the measured values of the critical temperature, and normal state conductivity.
In figure 8.13 the red curve represents the obtained theoretical curve using α. For high temperatures the predicted decrease of the resonance frequency is smaller than observed in the experiment. The temperature dependence of the internal quality factor Q_i using both values of α coincides for up to $T = 1.4\,\mathrm{K}$; the exponential decrease of the internal quality factor Q_i is than weaker for α_{theo}.
In literature the deviations are assumed to be due to disorder in the superconducting resonator material [Driessen et al., 2012, Coumou et al., 2013]; a generalized Mattis-Bardeen theory employing a broadened quasi-particle density of states with an effective pair-breaking is used. In [de Visser et al., 2014] the effects on internal quality factor and resonance frequency is explained with a non-thermal quasi-particle distribution. In a recent publication a two-channel model based on the Mattis-Bardeen theory was employed to fit the experimental data obtaining quantitative agreement between experiment and theory [Žemlička et al., 2015]. The deviations in our device for the temperature range $0.5\,\mathrm{K} < T < 3\,\mathrm{K}$ are still unclear.

8.8 Combining carbon nanotubes and coplanar waveguide resonators

In literature the dipole coupling of carbon nanotube double quantum dots and CPW resonators was already reported [Viennot et al., 2014]. Regarding the device geometry, the coupling was there achieved by a hammer-like coupler; this hammer is capacitively coupled to a half wavelength CPW resonator and extended to one of the two quantum dots defined within the carbon nanotube. A charge-photon coupling factor of a few MHz was observed. This is comparable to existing experiments based on two-dimensional electron gases [Frey et al., 2012, Toida et al., 2013] and on indium arsenide nanowires [Peterson et al., 2012]. Important quantities are the decoherence rate of the qubit and the decay rate of the resonator; in table 8.4 both rates and the coupling factors are listed for different experiments. The cavity decay rate describes the time the CPW resonators needs to return to its equilibrium. For qubit devices the coherence time has to be long enough to enable manipulation and read-out of the qubit. Strong coupling is

achieved if the qubit-photon coupling exceeds the decoherence and cavity decay rate; comparing the experiments listed in table 8.4 signs of strong coupling was observed in different material systems. Achieving a strong coupling regime is still challenging and for future qubit devices still improvements are necessary.
For carbon nanotube devices two different ways to combine carbon nanotubes and CPW resonators are conceivable:

Coplanar waveguide resonator processed onto carbon nanotubes

The carbon nanotube is grown by CVD and contacted by metallic electrodes. Afterwards the carbon nanotube and its contacts are isolated by an additional oxide layer. In the end the CPW resonator is fabricated; here Nb is used as superconducting material. In figure 8.14 a room temperature characterization measurement of such a carbon nanotube device attached to a CPW resonator is shown; the minimal room temperature resistance is about 66 MΩ. Figure 8.15 shows such a device. The coupling between the resonator and the quantum dot is achieved by the gate finger of the carbon nanotube, which is coupled capacitively to the meandering resonator structure. As first attempt the coupling of a single quantum dot defined in a carbon nanotube and a CPW resonator should be achieved. The design was adapted from recent publications [Viennot et al., 2014].
An advantage of this fabrication procedure would be that we can use Nb quarter wavelength CPW resonators for the fabrication. A big problem is the number of fabrication steps; achieving regular, clean carbon nanotubes is more complicated. Unfortunately the CPW resonator of this device did not display resonance features at liquid helium temperature; the substrate treatment might affect the properties of the CPW resonator.

Overgrown carbon nanotube and coplanar waveguide resonator

A second possible design combines a pre-defined CPW resonator and a subsequent overgrowth of the carbon nanotube over a pre-defined electrode and coupling geometry, as it was done for our measurements on suspended carbon nanotube nano-electromechanical oscillators. For this, rhenium-molybdenum CPW resonators were developed and tested under CVD growth conditions. First working quarter wavelength ReMo resonators show internal quality factors up to $2.3 \cdot 10^4$ before CVD and up to 4200 after the CVD growth [Götz et al., 2015].

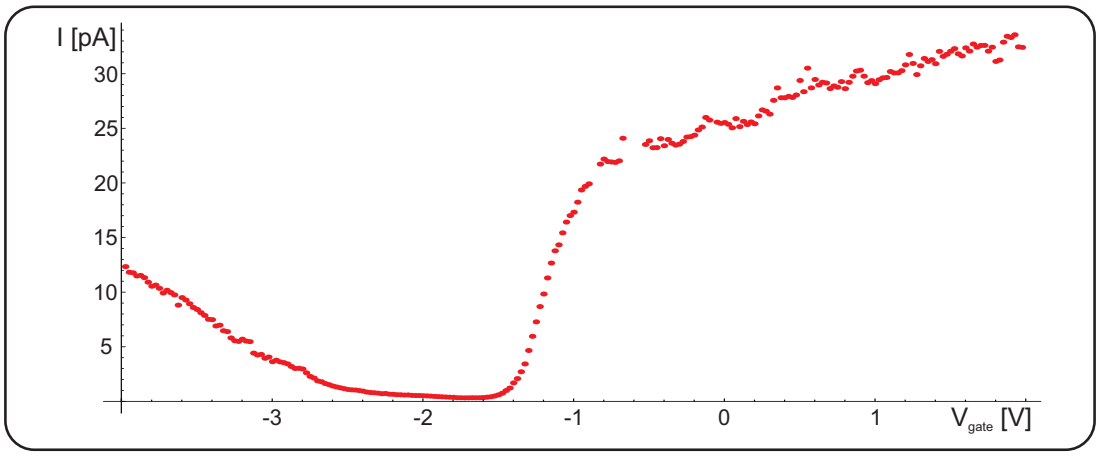

Figure 8.14: Current through a carbon nanotube at room temperature as a function of applied gate voltage. The bias voltage was set to $V_{\text{bias}} = -2\,\text{mV}$. A band gap of the carbon nanotube becomes visible. The measurement was done at room temperature and after the growth of a 150 nm thick Al_2O_3 layer on top of the device.

	coupling	cavity decay rate	decoherence rate
[Wallraff et al., 2004]	$g_c = 2\pi \cdot 6\,\text{MHz}$ cooper pair box GaAs 2DEG	$\kappa = 2\pi \cdot 0.8\,\text{MHz}$	$\gamma = 2\pi \cdot 0.7\,\text{MHz}$
[Toida et al., 2013] [Wallraff et al., 2013]	$g_c \approx 25\,\text{MHz}$ charge qubit GaAs 2DEG	$\kappa = 8\,\text{MHz}$	$\gamma = 300\,\text{MHz}$
[Viennot et al., 2015]	$g_s = 2\pi \cdot 1.3\,\text{MHz}$ spin qubit carbon nanotube	$\kappa = 2\pi \cdot 0.8\,\text{MHz}$	$\gamma \approx 2\pi \cdot 2.5\,\text{MHz}$
[Frey et al., 2012]	$g_c = 2\pi \cdot 50\,\text{MHz}$ charge qubit GaAs 2DEG	$\kappa = 2\pi \cdot 2.6\,\text{MHz}$	$\gamma \approx 2\pi \cdot 3.1\,\text{GHz}$
[Viennot et al., 2014]	$g_c = 2\pi \cdot 3.3\,\text{MHz}$ charge qubit carbon nanotube		$\gamma = 550\,\text{MHz}$

Table 8.4: Listed are different experiments observing a qubit-photon coupling in carbon nanotube devices and two-dimensional electron gases, see text.

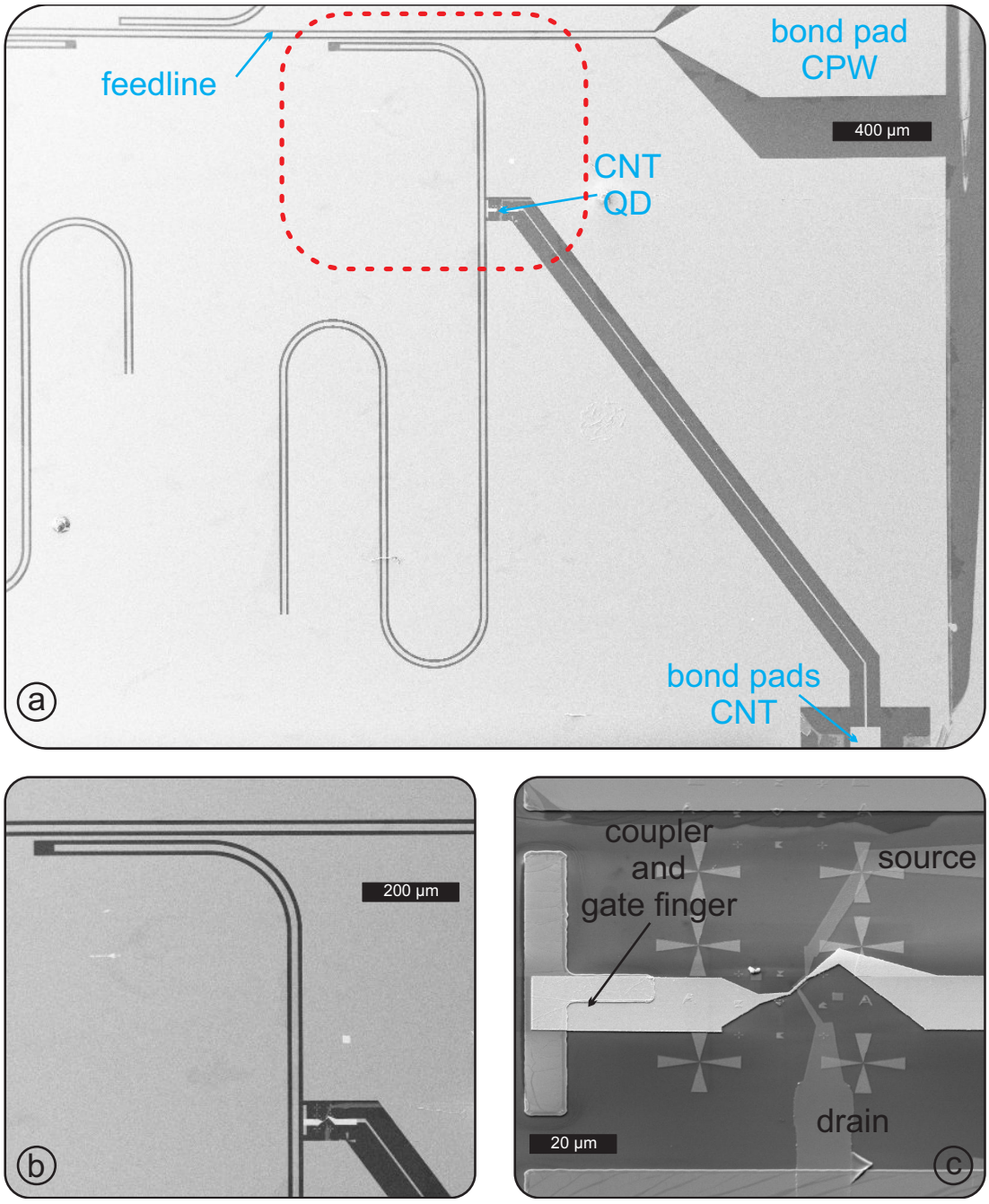

Figure 8.15: (a) CPW resonator coupled to a carbon nanotube single quantum dot structure. The carbon nanotube is placed near one of the meandering resonators (b). The coupling is achieved capacitively by a hammer like structure, which is also used as a gate finger to tune the electro-chemical potential within the carbon nanotube (c). Note that between the carbon nanotube (and its contacts) and the metal layer defining the resonator an oxide layer is deposited for isolation.

CHAPTER 9

Conclusions and outlook

The investigation of nano-electromechanical properties of carbon nanotubes, the preparation of a reliable fabrication process and measurement setup for coplanar waveguides, and work towards a combination of both systems was the scope of this thesis. First two different suspended carbon nanotube quantum dot devices were measured; both with a slightly different electrode geometry. Numerical transmission calculations were performed for various kinds of (n, m) carbon nanotubes in a parallel magnetic field to obtain a more detailed understanding of the experiment. For future HF measurements a dilution system was built up; first quarter wavelength CPW resonators could be tested at millikelvin temperature. Next step would be the combination of carbon nanotube quantum dots and superconducting CPW resonators.

We shifted the growth of the carbon nanotubes to the very last fabrication step to avoid contaminations due to further processing; in principle clean, and defect-free carbon nanotubes can be grown this way. Electronic transport measurements in a parallel magnetic field for one device showed the single particle spectrum of the carbon nanotube and a four-fold shell filling. A Dirac point crossing around $B_{\parallel} \approx 6\,\mathrm{T}$ is observed, numerical transmission calculations are employed trying to identify the chiral indices (n, m) of the measured carbon nanotube. The Dirac point crossing of the single particle spectrum crucially depends on a parallel magnetic field, and the physical properties of the carbon nanotube, i.e. the chiral indices (n, m) and the length of the carbon nanotube. In addition we could show together with the theory group of Prof. Milena Grifoni, that a magnetic field dependent $k_{\parallel}$ improves analytic modeling of carbon nanotubes significantly.

The interplay of electronic and mechanical degrees of freedom in suspended carbon nanotubes is scope of many different research groups. The interaction of single electron tunneling through a carbon nanotube quantum dot and the mechanical oscillation of suspended carbon nanotubes can be observed in the carbon nanotube bending mode. Coupling the longitudinal stretching mode of a carbon nanotube and electronic transport leads to Franck-Condon physics in suspended carbon nanotubes.

We observe a coupling of electrons and vibrons of the longitudinal stretching mode in a suspended carbon nanotube device. A magnetic field dependent Franck-Condon coupling factor was observed. In the theory group of Prof. Milena Grifoni it was theoretically shown that the electron-vibron coupling crucially depends on the size and the relative position of the embedded carbon nanotube quantum dot and the vibron [Donarini et al., 2012]. It seems plausible that the size of the vibron is fixed to the length of the suspended part of the carbon nanotube; the parallel magnetic field changes than size and position of the embedded carbon nanotube quantum dot. A decrease of the measured, numerically derived conductance for increasing magnetic field was observed in the experiment. This is connected to a more and more located electronic density at the center of the carbon nanotube for high magnetic fields.

In a second suspended carbon nanotube device we observed a negative frequency tuning of the mechanical bending mode of a clean, suspended carbon nanotube. We were able to decrease the mechanical resonance frequency about 75 % from its maximum value by applying a back gate voltage [Stiller et al., 2013]. An electrostatic softening leads to an additional effective contribution to the spring constant of the carbon nanotube. In addition single-electron tunneling in the few charge carrier limit was observed, and self-oscillation effects of the mechanical motion driven by single-electron tunneling through the embedded carbon nanotube quantum dot [Usmani et al., 2007, Schmid et al., 2012]. Furthermore, it could be shown in our research group that this self-oscillation effects can be damped by placing the carbon nanotube in a viscous mixture of ^{3}He/^{4}He in a top-loading dilution refrigerator [Schmid et al., 2015b].

First measurements of niobium superconducting quarter wavelength resonators were presented; we achieved internal quality factors up to $2.4 \cdot 10^5$ employing a dilution refrigerator designed for high frequency measurements. The system is ready to measure both d.c. and HF samples at the same time; further improvements of cabling and filters will be installed in the near future. The low temperature behavior of the resonance frequency and the internal quality factor were both well described by changes in the kinetic inductance fraction and the loss due to two-level systems present in the substrate material. Different geometries for half/quarter wavelength resonators are to be tested; also different materials for

the superconducting resonator are under investigation [Singh et al., 2014, Götz et al., 2015].

Future experiments will target the combination of superconducting resonators and carbon nanotubes. Two different kinds of experiments are imaginable: The dispersive coupling of carbon nanotube quantum dots and quarter/half wavelength resonators as discussed in section 8.8, and the dissipative coupling of an impedance-matching stub tuner circuit and a carbon nanotube [Ranjan et al., 2015]. Both methods will be addressed in Regensburg.
A new fabrication technique employing carbon nanotube stamping [Pei et al., 2012, Gramich et al., 2015] is under investigation in Regensburg to combine carbon nanotubes and pre-defined metallic contacts. Stamping will improve the combination with superconducting resonators due to the fact that the carbon nanotube can be transferred to superconducting structures consisting of materials, e.g. niobium, which would otherwise not survive the carbon nanotube growth process. Carbon nanotubes are grown by CVD on SiO_2 stamps and transferred to a device with pre-defined metallic contacts; first attempts of stamped carbon nanotube device were already measured. The stamped carbon nanotubes are assumed to be more regular and defect-free compared to on-chip grown and further processed carbon nanotubes since after the stamping less fabrication steps take place; also contaminations of the substrate due to the CVD growth are avoided.

APPENDIX A

Fabrication details and recipes

A.1 Carbon nanotube quantum dot devices

Here the complete and detailed sample fabrication for Re and ReMo samples of chapter 3 is listed. Processing of both samples is quite similar for many fabrication steps. If necessary deviations are explained, else the given parameters are accurate for both devices.

Wafer material

A highly positive doped silicon ⟨100⟩ wafer (resistance: 0.01-0.02 Ωcm) is used as substrate material. The thermally grown (dry grown) silicon dioxide layer on top is 500 nm thick. To ensure a faster processing the wafer was only broken in pieces of 16×16 mm size. During the sample fabrication the wafer piece is further cut; final devices have a size of 4×4 mm.

Fabrication equipment

- ultra sonic bath: Elma Transsonic 310
- oxygen plasma oven: Plasmatic Systems, Inc. Plasma-Preen I
- mask aligner system: Karl Suss MJB3
- electron beam lithography system: Zeiss LeoSupra35 SEM
- reactive ion etching: Oxford Instruments PlasmaLab80 Plus system

- CVD growth oven: Lindberg/Blue M Tube Furnace oven

Substrate cleaning

1. acetone ultra-sonic bath for 3 min
2. rinse with iso-propanol and blow dry with nitrogen
3. oxygen plasma for 5 min at 1.8 mbar oxygen pressure and an electric power of 50 %
4. acetone ultra-sonic bath for 5 min
5. rinse with iso-propanol and blow dry with nitrogen

Optical lithography

1. spin coat Shipley 1805 photo resist onto sample
   30 sec (4500 rpm)
2. bake out resist for 2 min on a 90 °C hot plate
3. expose with mask aligner for 33 sec
4. development 40 sec in a mixture of three volume parts H_2O and one volume part NaOH
5. rinse 30 sec with water to stop development

Electron beam lithography (electrodes and gate finger)

1. spin coat 200K 3.5 % PMMA resist onto sample
   5 sec (3000 rpm) and 30 sec (8000 rpm)
2. bake out resist for 6 min on a 150 °C hot plate
3. expose with acceleration voltage 25 kV, area dose 195 $\mu C/cm^2$; current 330 pA
4. development 2 min in a mixture of three volume parts iso-propanol and one volume part MIBK
5. rinse 30 sec with iso-propanol

Electron beam lithography (catalyst point)

1. spin coat 200K 7 % PMMA resist onto sample
   5 sec (3000 rpm) and 30 sec (8000 rpm)
2. bake out resist for 6 min on a 150 °C hot plate
3. spin coat 950K 2 % PMMA resist onto sample
   5 sec (3000 rpm) and 30 sec (8000 rpm)
4. bake out resist for 6 min on a 150 °C hot plate
5. expose with acceleration voltage 25 kV, area dose 300 $\mu C/cm^2$; current 330 pA
6. development 2 min in a mixture of three volume parts iso-propanol and one volume part MIBK
7. rinse 30 sec with iso-propanol

Reactive ion etching

1. 50 sccm CHF_3 with a pressure of 55 mTorr at 150 W
   Time: 11 min; rate: 22 nm/min
2. 40 sccm Ar with a pressure of 40 mTorr at 150 W
   Time: 30 sec; rate: 8 nm/min

Metallic contacts

For Re a dc-sputter source is used. The pressure in the UHV chamber is adjusted to about 5×10^{-3} mbar and power of the dc source is regulated to 100 W; resulting deposition rate is about 1.68 Å/s. Sputter gas is argon 6.0.
For ReMo a ac-sputter source is additionally used for the Mo target. Mo is sputtered at a power of 75 W, this results in a deposition rate of 0.5 Å/s and Re is sputtered at a power of 95 W, with a resulting rate of 1.5 Å/s. Again the pressure is adjusted to 5×10^{-3} mbar.

Carbon nanotube catalyst suspension

- 40.0 mg $Fe(NO_3)_3 \cdot 9H_2O$ (Fluka Chemie AG)
- 30.0 mg Al_2O_3 nanoparticles (Degussa GMBH)
- 10.0 mg $[CH_3COCH{=}C(O\text{-})CH_3]_2MoO_3$ (Sigma-Aldrich Chemie GMBH)
- 30 ml methanol

Deposition of catalyst suspension

1. sonicate catalyst solution for 30 min
2. clean pipette with iso-propanol and methanol
3. fill acetone in a tall beaker glass and put it on a 60°C hot plate
4. drop catalyst solution onto sample
5. blow dry with nitrogen softly and at a small angle (between sample and gas flow)
6. bake out on a 150 °C hot plate for 6 min
7. check amount of deposited catalyst using an optical microscope
8. scratch sample as preparation for breaking into 4×4 mm pieces (without breaking)
9. shake sample upside down for 4 min in the tall beaker glass
10. rinse sample with acetone
11. rinse sample 30 sec with iso-propanol and blow dry with nitrogen
12. check in an optical microscope, if necessary repeat lift-off process
13. break the sample in 4×4 mm pieces

Carbon nanotube growth process

1. place sample in 1" quartz tube beside the thermometer
2. close quartz tube clamps firmly
3. open gas bottles of methane, argon and hydrogen
4. flush quartz tube; open all gas flow meters to their maximum for 2 min
5. stop methane and hydrogen gas flow
6. set argon gas flow to 1500 sccm
7. heat furnace up to 900°C
8. adjust hydrogen flow to 700 sccm
9. stop argon gas flow

10. carbon nanotube growth: adjust methane flow to 760 sccm for 15 min
11. stop methane gas flow
12. set argon gas flow to 1500 sccm
13. open furnace to switch it off; wait for cool down to 600°C
14. stop hydrogen gas flow
15. further cool down to 150°C
16. stop argon gas flow
17. open quartz tube and take out sample

This was the original growth recipe for the Re sample. For ReMo slight changes were made; newly installed mass flow controller were used; the temperature is reduced and the gas flow much lower. Changes in the growth process are underlined.

1. place sample in quartz tube beside the thermometer
2. close quartz tube clamps firmly
3. open gas bottles of methane, argon and hydrogen
4. flush quartz tube; open all gas flow meters to their maximum for 2 min
5. stop methane and hydrogen gas flow
6. set argon gas flow to 1500 sccm
7. heat furnace up to 850°C
8. adjust hydrogen flow to 20 sccm
9. stop argon gas flow
10. wait 10 min
11. carbon nanotube growth: adjust methane flow to 10 sccm for 60 min
12. stop methane gas flow
13. stop hydrogen gas flow
14. set argon gas flow to 1500 sccm
15. stop furnace; cool down to 120°C
16. stop argon gas flow
17. open quartz tube and take out sample

A.2 Coplanar waveguide fabrication

Now the complete and detailed sample fabrication for the Nb CPW resonators of chapter 8 is listed.

Wafer material

A compensation doped silicon ⟨100⟩ wafer (resistance: >10 kΩcm) is used as substrate material. The silicon dioxide layer on top is 500 nm thick. The wafers are pre-cut in pieces of 8×8 mm size. Used devices for fabrication are already listed in appendix A.1.

Cleaning

1. remove cover foil
2. acetone ultra-sonic bath for 5 min
3. rinse with iso-propanol and blow dry with nitrogen
4. oxygen plasma for 5 min at 1.8 mbar oxygen pressure and an electric power of 50 %
5. acetone ultra-sonic bath for 5 min
6. rinse with iso-propanol and blow dry with nitrogen

Optical lithography

1. spin coat AZ5214e photo resist onto sample
   60 sec by 4500 rpm
2. bake out resist for 50 sec on a 105 °C hot plate
3. expose with mask aligner for 25 sec
4. development 2 min in a mixture of four volume parts H_2O and one volume part AZ351B
5. rinse 30 sec with water to stop development

Reactive ion etching

- 20 sccm SF_6 and 15 sccm Ar with a pressure of 15 mTorr at 100 W
  Time: 2 min 30 sec

Niobium

For niobium a dc-sputter source is used. The pressure in the UHV chamber is adjusted to about 2-5$\times 10^{-3}$ mbar. Sputter gas is argon 6.0. Power of the dc source is regulated to 100 W. Thickness of the metal layer is about 135 nm using a deposition time of 30 min.

APPENDIX B

Calculating a theoretical value β

In section 7.2 the capacitance between carbon nanotube and ground plane was given by:

$$C_{\text{gate}} = \frac{2\pi\epsilon_0}{\ln\left(\frac{2h_0}{r}\right)}. \tag{B.1}$$

We take the second derivative:

$$C''_{\text{gate}} = \frac{2L\pi\epsilon_0\left[2+\ln\left(\frac{2h_0}{r}\right)\right]}{h^2\ln\left(\frac{2h_0}{r}\right)^3}. \tag{B.2}$$

The length of the suspended carbon nanotube segment is $L = 500\,\text{nm}$; we estimate a radius of the carbon nanotube $r = 1\,\text{nm}$. The distance between the global gate electrode and the carbon nanotube is $h_0 = 590\,\text{nm}$; 550 nm thickness of the oxide layer and 40 nm thickness of the metallic electrodes. Here the distance between global gate and carbon nanotube is assumed to be constant ($h = h_0$). This way we obtain for C''_{gate}:

$$C''_{\text{gate}} = 2.04875 \times 10^{-6}\,\frac{\text{F}}{\text{m}^2}. \tag{B.3}$$

Using the value of $T_0 = 7.3\,\text{pN}$ obtained from the experimental fit and equation 7.17, and an estimated mass of the carbon nanotube $m = 0.17 \cdot 10^{-21}\,\text{kg}$, we can calculate a theoretical value for β:

$$\beta_{\text{theo}} = \frac{C''_{\text{gate}}}{8\pi^2}\sqrt{\frac{L}{mT_0}} = 0.521\,\text{MHzV}^{-2}. \tag{B.4}$$

In figure B.1 the second derivative C''_{gate} is plotted as a function of the equilibrium height h_0.

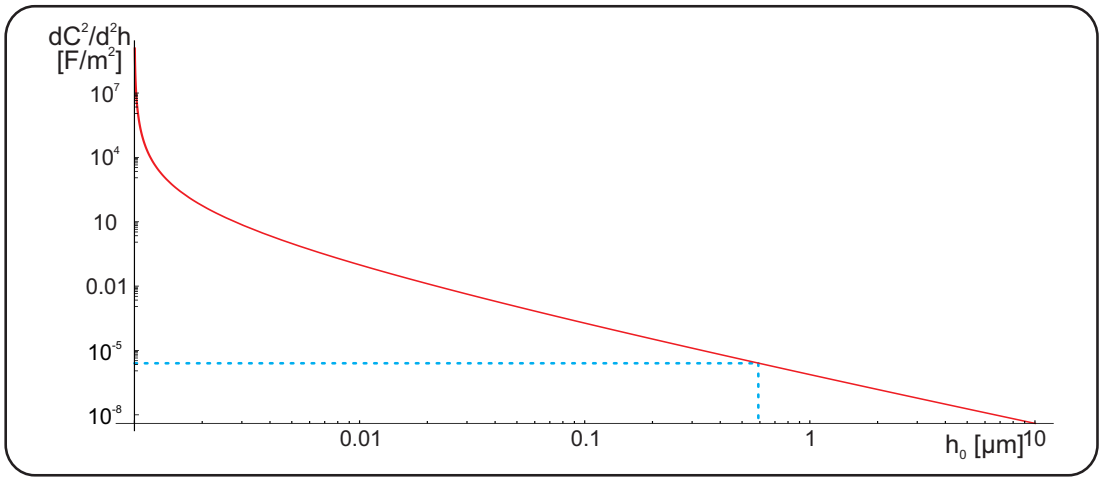

Figure B.1: Second derivative C''_{gate} as a function of the equilibrium height h_0. For a distance of 590 nm we obtain a value $C''_{\text{gate}} = 2.04875 \cdot 10^{-6}\,\frac{\text{F}}{\text{m}^2}$.

APPENDIX C

Numerical transmission calculations of carbon nanotubes

C.1 Hopping integrals

Here the hopping integrals necessary for the numerical transmission calculations are listed; they were calculated by M. Marganska following [Ando, 2000, del Valle et al., 2011]. In figure C.1 the relevant coordinates of the carbon atoms are sketched. The spin conserving hopping integrals read:

$$\begin{aligned}
\langle z_i \uparrow |V| z_j \uparrow \rangle &= V_{\mathrm{pp}}^{\pi} \cos\left(\Theta_i - \Theta_j\right) - \left(V_{\mathrm{pp}}^{\sigma} - V_{\mathrm{pp}}^{\pi}\right) \frac{r^2}{a^2} \left[1 - \cos\left(\Theta_i - \Theta_j\right)\right]^2 \\
+2i\delta &\left[V_{\mathrm{pp}}^{\pi} \sin\left(\Theta_i - \Theta_j\right) + \left(V_{\mathrm{pp}}^{\sigma} - V_{\mathrm{pp}}^{\pi}\right) \frac{r^2}{a^2} \sin\left(\Theta_i - \Theta_j\right) \left[1 - \cos\left(\Theta_i - \Theta_j\right)\right] \right] \\
\langle z_i \downarrow |V| z_j \downarrow \rangle &= V_{\mathrm{pp}}^{\pi} \cos\left(\Theta_i - \Theta_j\right) - \left(V_{\mathrm{pp}}^{\sigma} - V_{\mathrm{pp}}^{\pi}\right) \frac{r^2}{a^2} \left[1 - \cos\left(\Theta_i - \Theta_j\right)\right]^2 \\
-2i\delta &\left[V_{\mathrm{pp}}^{\pi} \sin\left(\Theta_i - \Theta_j\right) + \left(V_{\mathrm{pp}}^{\sigma} - V_{\mathrm{pp}}^{\pi}\right) \frac{r^2}{a^2} \sin\left(\Theta_i - \Theta_j\right) \left[1 - \cos\left(\Theta_i - \Theta_j\right)\right] \right],
\end{aligned}$$

where r is the carbon nanotube radius and a the lattice constant. The spin flipping hopping integrals read:

$$\begin{aligned}
\langle z_i \uparrow |V| z_j \downarrow \rangle &= -\delta \left(V_{\mathrm{pp}}^{\sigma} - V_{\mathrm{pp}}^{\pi}\right) \frac{r\left(Y_i - Y_j\right)}{a^2} \left[1 - \cos\left(\Theta_i - \Theta_j\right)\right] \left(e^{-i\Theta_i} - e^{-i\Theta_j}\right) \\
\langle z_i \downarrow |V| z_j \uparrow \rangle &= \delta \left(V_{\mathrm{pp}}^{\sigma} - V_{\mathrm{pp}}^{\pi}\right) \frac{r\left(Y_i - Y_j\right)}{a^2} \left[1 - \cos\left(\Theta_i - \Theta_j\right)\right] \left(e^{i\Theta_i} - e^{i\Theta_j}\right).
\end{aligned}$$

The interatomic potential V can be split into V_{pp}^{π} and V_{pp}^{σ} since the hopping between two orbitals occurs through a π-bond or through a σ-bond, the label

pp arises due to the hopping between neighboring p_z orbitals. The values V_{pp}^{π} and V_{pp}^{σ} are obtained by ab-initio calculations [Tománek and Louie, 1988, Bulaev et al., 2008]; we use $V_{\mathrm{pp}}^{\pi} = -2.66\,\mathrm{eV}$ and $V_{\mathrm{pp}}^{\sigma} = 6.38\,\mathrm{eV}$. The Hamiltonian for the spin-orbit coupling reads [Sakurai and Napolitano, 2011]:

$$H_{\mathrm{SO}} = \frac{1}{2m_e^2c^2}\left(\frac{\mathrm{d}V}{r\mathrm{d}r}\right) = \Delta\vec{L}\cdot\vec{s}, \tag{C.1}$$

the coupling constant Δ can be estimated as $\Delta = 0.9\cdot 10^{29}\,\frac{1}{\mathrm{eVs}^2}$. The coupling constant δ introduced for this calculation reads [Ando, 2000]:

$$\delta = \frac{\hbar^2\Delta}{2\epsilon_{\pi\sigma}}. \tag{C.2}$$

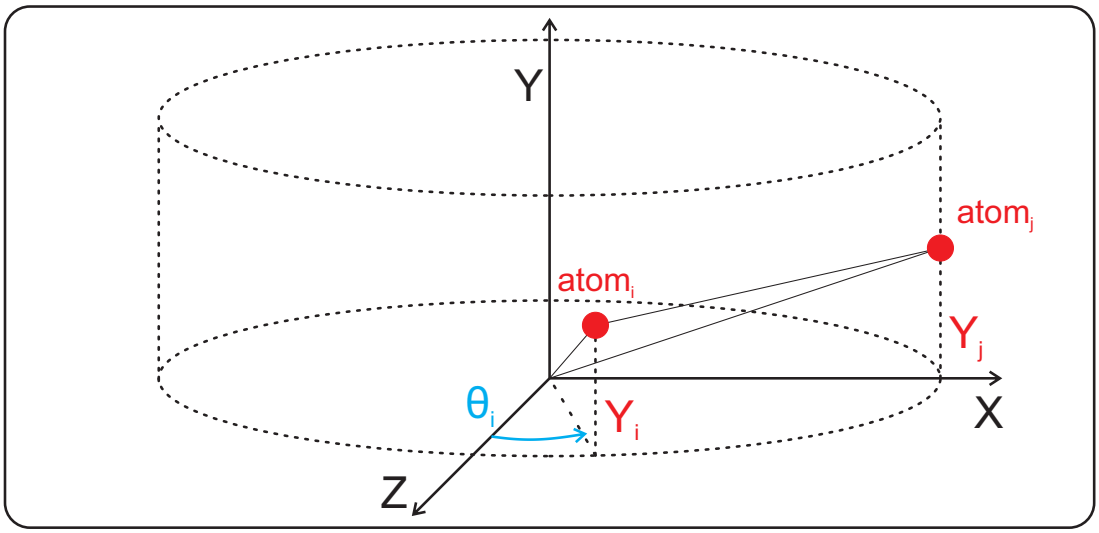

Figure C.1: Coordinate system for the hopping integrals; shown are the angle Θ_i and position $Y_{i,j}$ for the initial and final carbon atoms.

C.2 Additional transmission calculations

The calculated transmission as a function of both energy and parallel magnetic field is shown in figure C.2 for different lengths of a $(14, 11)$ carbon nanotube, this was used in section 5.3 for the length dependence of the Dirac point crossing. In table 5.2 the magnetic field value B_{min} corresponding to the Dirac point crossing for several carbon nanotubes is shown. The calculated transmissions as function of both energy and parallel magnetic field are depicted in figure C.3.

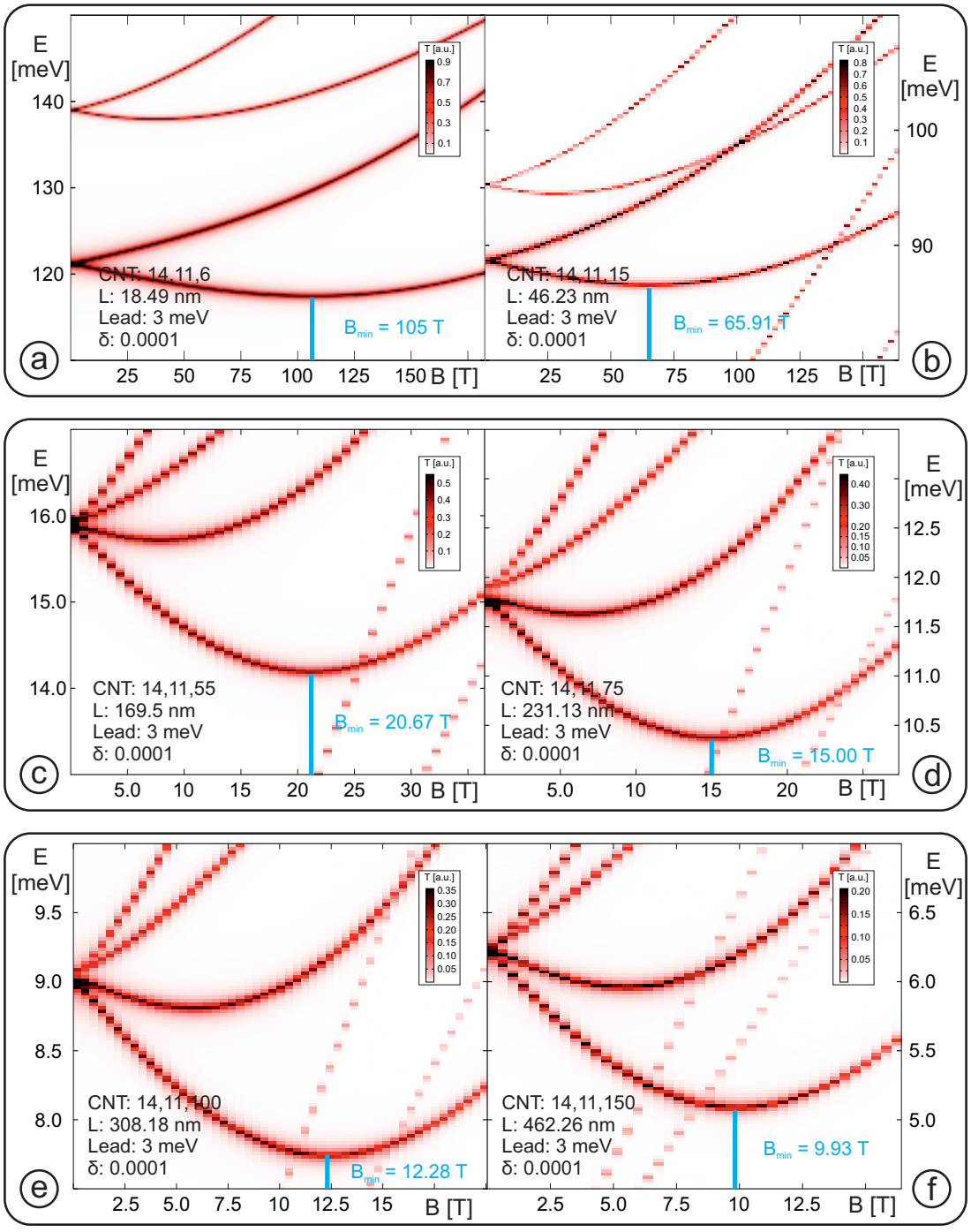

Figure C.2: Calculated transmission as a function both energy and parallel magnetic field for a $(14, 11)$ carbon nanotube with different length. The lead coupling $d = 3\,\text{meV}$ and the spin-orbit coupling parameter $\delta = 0.0001$ are kept constant. The Dirac point crossing shifts to lower values in magnetic field for increasing lengths. The evaluation is done in section 5.3, see figure 5.7.

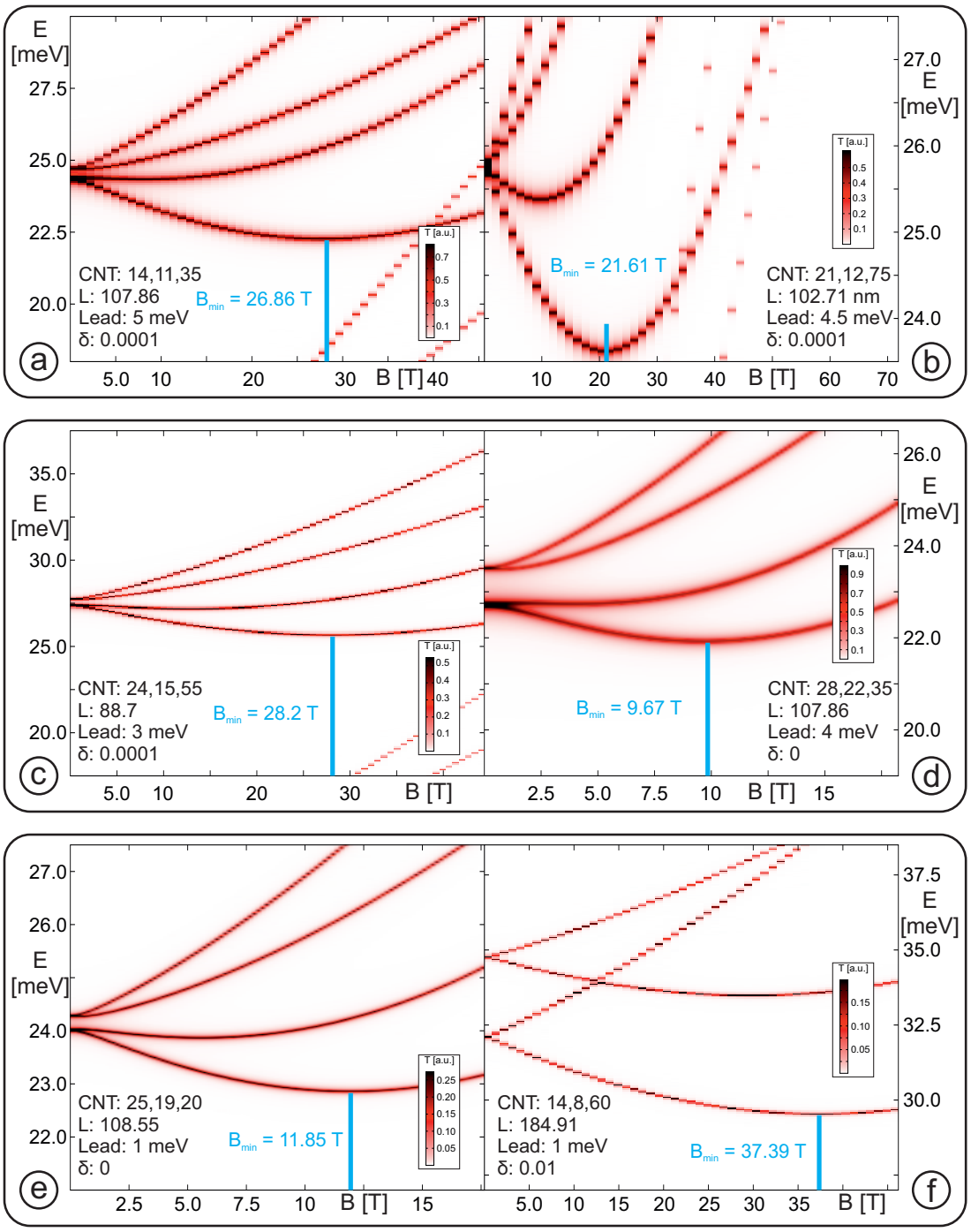

Figure C.3: Depicted is the calculated transmission as a function of both energy and parallel magnetic field for six different (n, m) carbon nanotubes. The extracted values and the evaluation of $B_{\min}$ are shown in section 5.3, see table 5.2.

APPENDIX D

Coplanar waveguide parameters

D.1 Calculation of the effective permittivity

We calculate the effective permittivity for our substrate and waveguide design following [Chen and Chou, 1997]. It turns out that the effect of the 10 nm thick layer of Al_2O_3 on the effective dielectric constant can be neglected since it is so thin compared to the silicon and silicon dioxide layer. Figure D.1 shows the necessary values used in the following calculation. With the same formalism also the phase velocity and the characteristic impedance can be calculated. The effective permittivity is given by

$$\epsilon_{\text{eff}} = 1 + \frac{\epsilon_{\text{r,Si}} - 1}{2} \cdot \frac{K(k_0)K(k_1')}{K(k_0')K(k_1)} + \frac{\epsilon_{\text{r,SiO}_2} - 1}{2} \cdot \frac{K(k_0)K(k_2')}{K(k_0')K(k_2)}, \tag{D.1}$$

where

$$k_i = \frac{\sinh\left(\frac{\pi c_3}{2h_i}\right)}{\sinh\left(\frac{\pi c_2}{2h_i}\right)} \sqrt{\frac{\sinh^2\left(\frac{\pi c_2}{2h_i}\right) - \sinh^2\left(\frac{\pi c_1}{2h_i}\right)}{\sinh^2\left(\frac{\pi c_3}{2h_i}\right) - \sinh^2\left(\frac{\pi c_1}{2h_i}\right)}}, \tag{D.2}$$

and

$$k_i' = \sqrt{1 - k_i^2}. \tag{D.3}$$

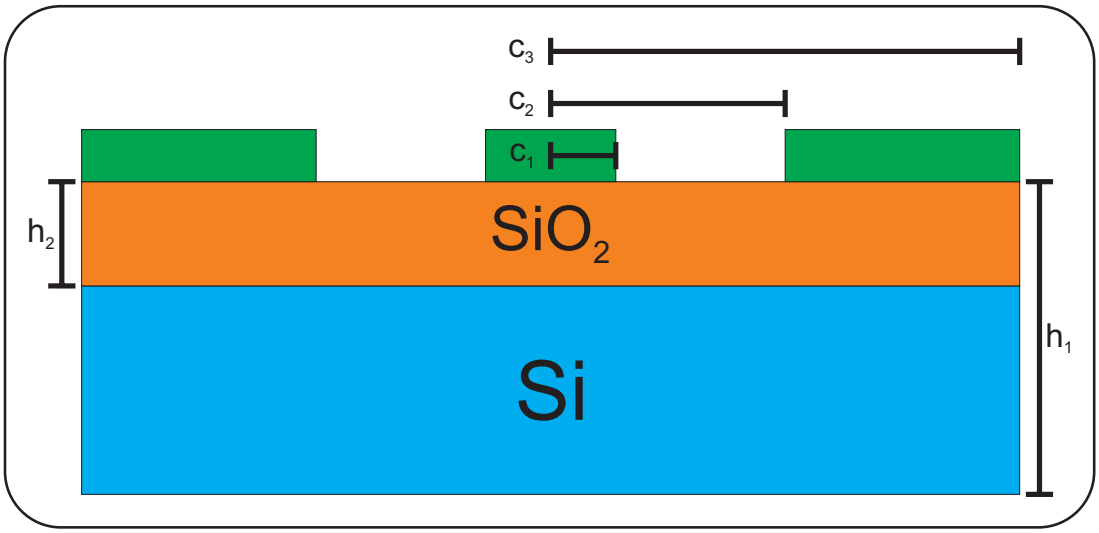

Figure D.1: Sketch of the layer structure for the used CPWs. Quantities for calculating the effective permittivity are marked.

For k_0 and k_0' one obtains:

$$k_0 = \frac{c_3}{c_2}\sqrt{\frac{c_2^2 - c_1^2}{c_3^2 - c_1^2}}, \tag{D.4}$$

and

$$k_0' = \sqrt{1 - k_0^2}. \tag{D.5}$$

$K(x)$ is the complete elliptical integral of the first kind:

$$K(k) = \int_0^{\frac{\pi}{2}} \frac{\mathrm{d}x}{\sqrt{(1 - x^2)\,(1 - k^2 x^2)}}. \tag{D.6}$$

For our devices we have $c_1 = 10 \cdot 10^{-6}\,\mathrm{m}$, $c_2 = 22 \cdot 10^{-6}\,\mathrm{m}$ and $c_3 = 3.8 \cdot 10^{-3}\,\mathrm{m}$. Note that c_3 is given by the width of one ground plane. The permittivities $\epsilon_{\mathrm{Si}} = 11.6$ and $\epsilon_{\mathrm{SiO_2}} = 3.78$ are taken from literature. Using these values and equation D.2 we obtain:

$$\epsilon_{\mathrm{eff}} = 4.87732, \tag{D.7}$$

for the effective permittivity.

From this value we can calculate the phase velocity

$$\nu_{\text{phase}} = \frac{c}{\epsilon_{\text{eff}}} = 1.3575 \cdot 10^8 \, \frac{\text{m}}{\text{s}}. \tag{D.8}$$

Using

$$Z_0 = \frac{30\pi}{\epsilon_{\text{eff}}} \cdot \frac{K(k)}{K(k')} \tag{D.9}$$

we can calculate the characteristic impedance $Z_0 = 47.29\,\Omega$.

D.2 Resonant and relaxation susceptibility tensors

The tensors ξ_{rel} and ξ_{res} are introduced in section 8.5 and connect the dipole moment of the TLS and the electro-magnetic field of the CPW resonator. They read [Gao, 2008]:

$$\xi_{rel} = -\frac{\mathrm{d}\sigma_z^1}{\mathrm{d}\epsilon} \cdot \frac{1 - i\omega T_1}{1 + \omega^2 T_1^2} \cdot \vec{d}_{\text{rel}} \tag{D.10}$$

and

$$\xi_{res} = -\frac{\sigma_z^0}{\hbar} \left[\frac{1}{\frac{\epsilon}{\hbar} - \omega + iT_2^{-1}} - \frac{1}{\frac{\epsilon}{\hbar} + \omega - iT_2^{-1}} \right] \cdot \vec{d}_{\text{res}}, \tag{D.11}$$

with

$$\sigma_z^1 = \frac{1 + \left(\frac{\epsilon}{\hbar} - \omega\right)^2 T_2^2}{1 + \Omega^2 T_1 T_2 + \left(\frac{\epsilon}{\hbar} - \omega\right)^2 T_2^2} \cdot \sigma_z^0 \tag{D.12}$$

and

$$\sigma_z^0 = -\tanh\left(\frac{\epsilon}{2k_B T}\right), \tag{D.13}$$

where Ω is the Rabi frequency. T_1 describes the interaction of the TLS and the phonon bath and gives the relaxation rate into the equilibrium from non-equilibrium population. T_2 is called the dephasing time; details see [Phillips,

1987].
For completeness, the complex digamma function used in section 8.5 is defined as

$$\Psi(x) = \frac{\mathrm{d}}{\mathrm{d}x} \cdot \ln[\Gamma(x)] = \frac{\Gamma'(x)}{\Gamma(x)}, \tag{D.14}$$

with

$$\Gamma(x) = \int_0^\infty t^{x-1} e^{-t} \mathrm{d}t. \tag{D.15}$$

APPENDIX E

HF measurement technology

Here a complete list of measurement devices and high frequency components is given.

Measurement devices

- Signal generator: Rhode und Schwarz SMB 100 A; 9 kHz - 6 GHz
- Signal Analyzer: Rhode und Schwarz FSV; 10 Hz - 7 GHz
- Vector Network Analyzer: Rhode und Schwarz ZNB20; 100 kHz - 20 GHz

High frequency components

- 3 dB attenuator: Rosenberger 32AS102-K03S3
- 10 dB attenuator: Rosenberger 32AS102-K10S3
- 20 dB attenuator: Rosenberger 32AS102-K03S3
- circulator: Quinstar QXE89
- High electron mobility transistor: Caltech CITCRYO1-12A

Pre-amplifier

The HEMT pre-amplifier is mounted at the 1K-plate of the dilution system. Bias voltage is set to $V_{sd} = 1.34\,V$ and the gate voltages to $V_{g1} = 1.85\,V$ and $V_{g2} = 1.20\,V$. The resulting current reads $I = 14.2\,mA$.

Dilution system

- Oxford Kelvinox 400HA
- Cooling Power: $400\,\mu W$ at $100\,mK$
- Base temperature (nominal): $7.5\,mK$
- Mixture: 85 liter
- ^3He: 15 liter
- Dewar: 102.5 liter

Bibliography

[Ajiki and Ando, 1993] Ajiki, H. and Ando, T. (1993). Electronic States of Carbon Nanotubes. *Journal of the Physical Society of Japan*, 62(4):1255–1266. (Cited on page 33)

[Anderson et al., 1972] Anderson, P. W., Halperin, B. I., and Varma, C. M. (1972). Anomalous low-temperature thermal properties of glasses and spin glasses. *Philosophical Magazine*, 25(1):1–9. (Cited on page 88)

[Ando, 2000] Ando, T. (2000). Spin-Orbit Interaction in Carbon Nanotubes. *Journal of the Physical Society of Japan*, 69(6):1757–1763. (Cited on pages 116 and 117)

[Baselmans et al., 2005] Baselmans, J., Barends, R., Hovenier, J., Gao, J. R., Hoevers, H., de Korte, P., and Klapwijk, T. (2005). High Q Niobium superconducting resonators for use as Kinetic Inductance sensing elements. *Bulletin de la Société Royale des Sciences de Liège*, 74(5-6):491–497. (Cited on page 84)

[Bethune et al., 1993] Bethune, D. S., Klang, C. H., de Vries, M. S., Gorman, G., Savoy, R., Vazquez, J., and Beyers, R. (1993). Cobalt-catalysed growth of carbon nanotubes with single-atomic-layer walls. *Nature*, 363(6430):605–607. (Cited on page 1)

[Biercuk et al., 2005] Biercuk, M. J., Garaj, S., Mason, N., Chow, J. M., and Marcus, C. M. (2005). Gate-Defined Quantum Dots on Carbon Nanotubes. *Nano Letters*, 5(7):1267–1271. PMID: 16178222. (Cited on page 24)

[Blais et al., 2004] Blais, A., Huang, R.-S., Wallraff, A., Girvin, S. M., and Schoelkopf, R. J. (2004). Cavity quantum electrodynamics for superconducting

electrical circuits: An architecture for quantum computation. *Phys. Rev. A*, 69:062320. (Cited on page 2)

[Bockrath et al., 1999] Bockrath, M., Cobden, D. H., Lu, J., Rinzler, A. G., Smalley, R. E., Balents, L., and McEuen, P. L. (1999). Luttinger-liquid behaviour in carbon nanotubes. *Nature*, 397(6720):598–601. (Cited on page 1)

[Braig and Flensberg, 2003] Braig, S. and Flensberg, K. (2003). Vibrational sidebands and dissipative tunneling in molecular transistors. *Phys. Rev. B*, 68:205324. (Cited on pages 53 and 56)

[Breit and Wigner, 1936] Breit, G. and Wigner, E. (1936). Capture of Slow Neutrons. *Phys. Rev.*, 49:519–531. (Cited on page 40)

[Bruno et al., 2015] Bruno, A., de Lange, G., Asaad, S., van der Enden, K. L., Langford, N. K., and DiCarlo, L. (2015). Reducing intrinsic loss in superconducting resonators by surface treatment and deep etching of silicon substrates. *Applied Physics Letters*, 106(18):–. (Cited on pages 83 and 91)

[Bulaev et al., 2008] Bulaev, D. V., Trauzettel, B., and Loss, D. (2008). Spin-orbit interaction and anomalous spin relaxation in carbon nanotube quantum dots. *Phys. Rev. B*, 77:235301. (Cited on page 117)

[Cao et al., 2005] Cao, J., Wang, Q., and Dai, H. (2005). Electron transport in very clean, as-grown suspended carbon nanotubes. *Nature Materials*, 4(10):745–749. (Cited on pages 1 and 13)

[Cavaliere et al., 2010] Cavaliere, F., Mariani, E., Leturcq, R., Stampfer, C., and Sassetti, M. (2010). Asymmetric Franck-Condon factors in suspended carbon nanotube quantum dots. *Phys. Rev. B*, 81:201303. (Cited on page 57)

[Chen and Chou, 1997] Chen, E. and Chou, S. (1997). Characteristics of coplanar transmission lines on multilayer substrates: modeling and experiments. *Microwave Theory and Techniques, IEEE Transactions on*, 45(6):939–945. (Cited on pages 78 and 120)

[Childress et al., 2004] Childress, L., Sørensen, A. S., and Lukin, M. D. (2004). Mesoscopic cavity quantum electrodynamics with quantum dots. *Phys. Rev. A*, 69:042302. (Cited on page 2)

[Cleland, 2010] Cleland, A. N. (2010). *Foundations of Nanomechanics*. Springer. (Cited on page 66)

[Collin, 1992] Collin, R. E. (1992). *Foundations for microwave engineering*. McGraw-Hill, Inc. (Cited on page 97)

[Condon, 1926] Condon, E. (1926). A Theory of Intensity Distribution in Band Systems. *Phys. Rev.*, 28:1182–1201. (Cited on page 53)

[Coumou et al., 2013] Coumou, P., Zuiddam, M., Driessen, E., de Visser, P., Baselmans, J., and Klapwijk, T. (2013). Microwave Properties of Superconducting Atomic-Layer Deposited TiN Films. *Applied Superconductivity, IEEE Transactions on*, 23(3):7500404–7500404. (Cited on pages 98 and 145)

[Craig and Lester, 2004] Craig, N. and Lester, T. (2004). Hitchhiker's Guide to the Dilution Refrigerator. (Cited on page 21)

[Datta, 1995] Datta, S. (1995). *Electronic transport in mesoscopic systems*. Cambridge University Press. (Cited on pages 23 and 33)

[Day et al., 2003] Day, P. K., LeDuc, H. G., Mazin, B. A., Vayonakis, A., and Zmuidzinas, J. (2003). A broadband superconducting detector suitable for use in large arrays. *Nature*, 425(6960):817–821. (Cited on page 2)

[De Franceschi et al., 2001] De Franceschi, S., Sasaki, S., Elzerman, J. M., van der Wiel, W. G., Tarucha, S., and Kouwenhoven, L. P. (2001). Electron Cotunneling in a Semiconductor Quantum Dot. *Phys. Rev. Lett.*, 86:878–881. (Cited on page 71)

[de Visser et al., 2014] de Visser, P. J., Goldie, D. J., Diener, P., Withington, S., Baselmans, J. J. A., and Klapwijk, T. M. (2014). Evidence of a Nonequilibrium Distribution of Quasiparticles in the Microwave Response of a Superconducting Aluminum Resonator. *Phys. Rev. Lett.*, 112:047004. (Cited on page 98)

[del Valle et al., 2011] del Valle, M., Margańska, M., and Grifoni, M. (2011). Signatures of spin-orbit interaction in transport properties of finite carbon nanotubes in a parallel magnetic field. *Phys. Rev. B*, 84:165427. (Cited on pages 40, 48 and 116)

[Delbecq et al., 2011] Delbecq, M. R., Schmitt, V., Parmentier, F. D., Roch, N., Viennot, J. J., Fève, G., Huard, B., Mora, C., Cottet, A., and Kontos, T. (2011). Coupling a Quantum Dot, Fermionic Leads, and a Microwave Cavity on a Chip. *Phys. Rev. Lett.*, 107:256804. (Cited on page 2)

[Donarini et al., 2012] Donarini, A., Yar, A., and Grifoni, M. (2012). Spectrum and Franck-Condon factors of interacting suspended single-wall carbon nanotubes. *New Journal of Physics*, 14(2):023045. (Cited on pages 57, 62 and 104)

[Dresselhaus and Eklund, 2010] Dresselhaus, M. S. and Eklund, P. C. (2010). Phonons in ccarbon nanotubes. *Advances in Physics*, 49(6):705–814. (Cited on page 54)

[Driessen et al., 2012] Driessen, E. F. C., Coumou, P. C. J. J., Tromp, R. R., de Visser, P. J., and Klapwijk, T. M. (2012). Strongly Disordered TiN and NbTiN *s*-Wave Superconductors Probed by Microwave Electrodynamics. *Phys. Rev. Lett.*, 109:107003. (Cited on pages 98 and 145)

[Enss and Hunklinger, 2005] Enss, C. and Hunklinger, S. (2005). *Low temperature physics*. Springer. (Cited on pages 20, 69, 88 and 90)

[Fischer et al., 2009] Fischer, J., Trauzettel, B., and Loss, D. (2009). Hyperfine interaction and electron-spin decoherence in graphene and carbon nanotube quantum dots. *Phys. Rev. B*, 80:155401. (Cited on page 2)

[Flensberg, 2006] Flensberg, K. (2006). Electron-vibron coupling in suspended nanotubes. *New Journal of Physics*, 8(1):5. (Cited on page 57)

[Franck and Dymond, 1926] Franck, J. and Dymond, E. G. (1926). Elementary processes of photochemical reactions. *Trans. Faraday Soc.*, 21:536–542. (Cited on page 53)

[Frey et al., 2012] Frey, T., Leek, P. J., Beck, M., Blais, A., Ihn, T., Ensslin, K., and Wallraff, A. (2012). Dipole Coupling of a Double Quantum Dot to a Microwave Resonator. *Phys. Rev. Lett.*, 108:046807. (Cited on pages 98 and 100)

[Gao, 2008] Gao, J. (2008). *The physics of Superconducting Microwave Resonators*. PhD thesis, California Institute of Technology. (Cited on pages 88, 90, 97 and 122)

[Gao et al., 2008] Gao, J., Zmuidzinas, J., Vayonakis, A., Day, P., Mazin, B., and Leduc, H. (2008). Equivalence of the Effects on the Complex Conductivity of Superconductor due to Temperature Change and External Pair Breaking. *Journal of Low Temperature Physics*, 151(1-2):557–563. (Cited on page 95)

[Gaudreau et al., 2012] Gaudreau, L., Granger, G., Kam, A., Aers, G. C., Studenikin, S. A., Zawadzki, P., Pioro-Ladriere, M., Wasilewski, Z. R., and Sachrajda, A. S. (2012). Coherent control of three-spin states in a triple quantum dot. *Nat Phys*, 8(1):54–58. (Cited on page 24)

[Goldhaber-Gordon et al., 1998] Goldhaber-Gordon, D., Shtrikman, H., Mahalu, D., Abusch-Magder, D., Meirav, U., and Kastner, M. A. (1998). Kondo effect in a single-electron transistor. *Nature*, 391(6663):156–159. (Cited on pages 29 and 69)

[Goß et al., 2011] Goß, K., Smerat, S., Leijnse, M., Wegewijs, M. R., Schneider, C. M., and Meyer, C. (2011). Spin-dependent electronic hybridization in a rope of carbon nanotubes. *Phys. Rev. B*, 83:201403. (Cited on page 71)

[Gramich et al., 2015] Gramich, J., Baumgartner, A., Muoth, M., Hierold, C., and Schönenberger, C. (2015). Fork stamping of pristine carbon nanotubes onto ferromagnetic contacts for spin-valve devices. *physica status solidi (b)*, 252(11):2496–2502. (Cited on page 105)

[Götz et al., 2015] Götz, K. J. G., Blien, S., Stiller, P. L., Vavra, O., Mayer, T., Huber, T., Meier, T. N. G., Kronseder, M., Strunk, C., and Hüttel, A. K. (2015). Co-sputtered MoRe thin films for carbon nanotube growth-compatible super gigahertz electronics. *arXiv:1510.00278*. (Cited on pages 91, 95, 99 and 105)

[Hinken, 1988] Hinken, J. H. (1988). *Superconductor electronics: Fundamentals and microwave applications*. Springer Verlag Berlin Heidelberg New York. (Cited on page 95)

[Hüttel et al., 2008] Hüttel, A. K., Poot, M., Witkamp, B., and van der Zant, H. S. J. (2008). Nanoelectromechanics of suspended carbon nanotubes. *New Journal of Physics*, 10(9):095003. (Cited on pages 55 and 56)

[Hüttel et al., 2009a] Hüttel, A. K., Steele, G. A., Witkamp, B., Poot, M., Kouwenhoven, L. P., and van der Zant, H. S. J. (2009a). Carbon Nanotubes as Ultrahigh Quality Factor Mechanical Resonators. *Nano Letters*, 9(7):2547–2552. (Cited on pages 1, 2 and 68)

[Hüttel et al., 2009b] Hüttel, A. K., Witkamp, B., Leijnse, M., Wegewijs, M. R., and van der Zant, H. S. J. (2009b). Pumping of Vibrational Excitations in the Coulomb-Blockade Regime in a Suspended Carbon Nanotube. *Phys. Rev. Lett.*, 102:225501. (Cited on page 55)

[Žemlička et al., 2015] Žemlička, M., Neilinger, P., Trgala, M., Rehák, M., Manca, D., Grajcar, M., Szabó, P., Samuely, P., Gaži, i. c. v., Hübner, U., Vinokur, V. M., and Il'ichev, E. (2015). Finite quasiparticle lifetime in disordered superconductors. *Phys. Rev. B*, 92:224506. (Cited on page 98)

[Iijima and Ichihashi, 1993] Iijima, S. and Ichihashi, T. (1993). Single-shell carbon nanotubes of 1-nm diameter. *Nature*, 363(6430):603–605. (Cited on page 1)

[Island et al., 2012] Island, J. O., Tayari, V., McRae, A. C., and Champagne, A. R. (2012). Few-Hundred GHz Carbon Nanotube Nanoelectromechanical Systems (NEMS). *Nano Letters*, 12(9):4564–4569. PMID: 22888989. (Cited on pages 54 and 55)

[Izumida et al., 2009] Izumida, W., Sato, K., and Saito, R. (2009). Spin-Orbit Interaction in Single Wall Carbon Nanotubes: Symmetry Adapted Tight-Binding

Calculation and Effective Model Analysis. *Journal of the Physical Society of Japan*, 78(7):074707. (Cited on page 34)

[Jarillo-Herrero et al., 2004] Jarillo-Herrero, P., Sapmaz, S., Dekker, C., Kouwenhoven, L. P., and van der Zant, H. S. J. (2004). Electron-hole symmetry in a semiconducting carbon nanotube quantum dot. *Nature*, 429(6990):389–392. (Cited on page 24)

[Javey et al., 2003] Javey, A., Guo, J., Wang, Q., Lundstrom, M., and Dai, H. (2003). Ballistic carbon nanotube field-effect transistors. *Nature*, 424(6949):654–657. (Cited on page 23)

[Jaynes and Cummings, 1963] Jaynes, E. and Cummings, F. (1963). Comparison of quantum and semiclassical radiation theories with application to the beam maser. *Proceedings of the IEEE*, 51(1):89–109. (Cited on page 2)

[Jensen et al., 2005] Jensen, A., Hauptmann, J. R., Nygård, J., and Lindelof, P. E. (2005). Magnetoresistance in ferromagnetically contacted single-wall carbon nanotubes. *Phys. Rev. B*, 72:035419. (Cited on page 1)

[Jhang et al., 2010] Jhang, S. H., Marganska, M., Skourski, Y., Preusche, D., Witkamp, B., Grifoni, M., van der Zant, H., Wosnitza, J., and Strunk, C. (2010). Spin-orbit interaction in chiral carbon nanotubes probed in pulsed magnetic fields. *Phys. Rev. B*, 82:041404. (Cited on page 40)

[Jin et al., 2007] Jin, Z., Chu, H., Wang, J., Hong, J., Tan, W., and Li, Y. (2007). Ultralow Feeding Gas Flow Guiding Growth of Large-Scale Horizontally Aligned Single-Walled Carbon Nanotube Arrays. *Nano Letters*, 7(7):2073–2079. (Cited on page 16)

[Jung et al., 2013] Jung, M., Schindele, J., Nau, S., Weiss, M., Baumgartner, A., and Schönenberger, C. (2013). Ultraclean Single, Double, and Triple Carbon Nanotube Quantum Dots with Recessed Re Bottom Gates. *Nano Letters*, 13(9):4522–4526. PMID: 23962122. (Cited on page 24)

[Khalil, 2013] Khalil, M. (2013). *A study of two-level system defects in dielectric films using superconducting resonators*. PhD thesis, University of Maryland. (Cited on page 84)

[Khalil et al., 2012] Khalil, M. S., Stoutimore, M. J. A., Wellstood, F. C., and Osborn, K. D. (2012). An analysis method for asymmetric resonator transmission applied to superconducting devices. *Journal of Applied Physics*, 111(5):–. (Cited on page 83)

[Kong et al., 1998] Kong, J., Soh, H. T., Cassell, A. M., Quate, C. F., and Dai, H. (1998). Synthesis of individual single-walled carbon nanotubes on patterned silicon wafers. *Nature*, 395(6705):878–881. (Cited on page 13)

[Kouwenhoven et al., 1991] Kouwenhoven, L., van der Vaart, N., Johnson, A., Kool, W., Harmans, C., Williamson, J., Staring, A., and Foxon, C. (1991). Single electron charging effects in semiconductor quantum dots. *Zeitschrift für Physik B Condensed Matter*, 85(3):367–373. (Cited on page 27)

[Kouwenhoven et al., 1997] Kouwenhoven, L. P., Marcus, C. M., McEuen, P. L., Tarucha, S., Westervelt, R. M., and Wingreen, N. S. (1997). Electron transport in quantum dots. *Proceedings of the MATO Advanced Study Institute on Mesoscopic Electron Transport*, pages 105–214. (Cited on pages 24 and 26)

[Kuemmeth et al., 2008] Kuemmeth, F., Ilani, S., Ralph, D. C., and McEuen, P. L. (2008). Coupling of spin and orbital motion of electrons in carbon nanotubes. *Nature*, 452(7186):448–452. (Cited on page 34)

[Kugler, 2013] Kugler, S. (2013). Kohlenstoff-nanoröhrchen mit supraleitenden kontakten als nanomechanische resonatoren. Masterarbeit, Universität Regensburg. (Cited on page 65)

[Landau and Lifschitz, 1989] Landau, L. D. and Lifschitz, E. (1989). *Elastizitätstheorie*. Akademie-Verlag Berlin. (Cited on page 54)

[Lassagne et al., 2008] Lassagne, B., Garcia-Sanchez, D., Aguasca, A., and Bachtold, A. (2008). Ultrasensitive Mass Sensing with a Nanotube Electromechanical Resonator. *Nano Letters*, 8(11):3735–3738. (Cited on page 2)

[Lefèvre et al., 2005] Lefèvre, R., Goffman, M. F., Derycke, V., Miko, C., Forró, L., Bourgoin, J. P., and Hesto, P. (2005). Scaling Law in Carbon Nanotube Electromechanical Devices. *Phys. Rev. Lett.*, 95(18):185504. (Cited on page 66)

[LeRoy et al., 2004] LeRoy, B. J., Lemay, S. G., Kong, J., and Dekker, C. (2004). Electrical generation and absorption of phonons in carbon nanotubes. *Nature*, 432(7015):371–374. (Cited on page 54)

[Leturcq et al., 2009] Leturcq, R., Stampfer, C., Inderbitzin, K., Durrer, L., Hierold, C., Mariani, E., Schultz, M. G., von Oppen, F., and Ensslin, K. (2009). Franck-Condon blockade in suspended carbon nanotube quantum dots. *Nature Physics*, 5(5):327–331. (Cited on pages 53, 55 and 57)

[Liang et al., 2001] Liang, W., Bockrath, M., Bozovic, D., Hafner, J. H., Tinkham, M., and Park, H. (2001). Fabry - Perot interference in a nanotube electron waveguide. *Nature*, 411(6838):665–669. (Cited on pages 1 and 69)

[Lu, 1997] Lu, J. P. (1997). Elastic Properties of Carbon Nanotubes and Nanoropes. *Phys. Rev. Lett.*, 79:1297–1300. (Cited on pages 1 and 66)

[Macha et al., 2010] Macha, P., van der Ploeg, S. H. W., Oelsner, G., Il'ichev, E., Meyer, H.-G., Wünsch, S., and Siegel, M. (2010). Losses in coplanar waveguide resonators at millikelvin temperatures. *Applied Physics Letters*, 96(6):–. (Cited on page 84)

[Marganska et al., 2015] Marganska, M., Chudzinski, P., and Grifoni, M. (2015). The two classes of low-energy spectra in finite carbon nanotubes. *Phys. Rev. B*, 92:075433. (Cited on page 34)

[Marganska et al., 2011] Marganska, M., del Valle, M., Jhang, S. H., Strunk, C., and Grifoni, M. (2011). Localization induced by magentic fields in carbon nanotubes. *Physical Review B*. (Cited on pages 47 and 48)

[Mariani and von Oppen, 2009] Mariani, E. and von Oppen, F. (2009). Electron-vibron coupling in suspended carbon nanotube quantum dots. *Phys. Rev. B*, 80:155411. (Cited on pages 54, 57 and 62)

[Mattis and Bardeen, 1958] Mattis, D. C. and Bardeen, J. (1958). Theory of the Anomalous Skin Effect in Normal and Superconducting Metals. *Phys. Rev.*, 111:412–417. (Cited on page 77)

[Morpurgo et al., 1999] Morpurgo, A. F., Kong, J., Marcus, C. M., and Dai, H. (1999). Gate-Controlled Superconducting Proximity Effect in Carbon Nanotubes. *Science*, 286(5438):263–265. (Cited on page 1)

[Moser et al., 2014] Moser, J., Eichler, A., Guttinger, J., Dykman, M., and Bachtold, A. (2014). Nanotube mechanical resonators with quality factors of up to 5 million. *Nat Nano*, 9(12):1007–1011. (Cited on page 2)

[Moser et al., 2013] Moser, J., Guttinger, J., Eichler, A., Esplandiu, M., D., L., Dykman, M., and Bachtold, A. (2013). Ultrasensitive force detection with a nanotube mechanical resonator. *Nat Nano*, 8(7):493–496. (Cited on page 65)

[Nemec, 2007] Nemec, N. (2007). *Quantum Transport in Carbon-based Nanostructures*. PhD thesis, Universität Regensburg. (Cited on pages 33 and 39)

[Novoselov et al., 2004] Novoselov, K. S., Geim, A. K., Morozov, S. V., Jiang, D., Zhang, Y., Dubonos, S. V., Grigorieva, I. V., and Firsov, A. A. (2004). Electric Field Effect in Atomically Thin Carbon Films. *Science*, 306(5696):666–669. (Cited on page 5)

[Park et al., 2000] Park, H., Park, J., Lim, A. K. L., Anderson, E. H., Alivisatos, A. P., and McEuen, P. L. (2000). Nanomechanical oscillations in a single-C60 transistor. *Nature*, 407(6800):57–60. (Cited on page 53)

[Pei et al., 2012] Pei, F., Laird, E., Steele, G., and Kouwenhove, L. P. (2012). Valley-spin blockade and spin resonance in carbon nanotubes. *Nat Nano*, 7:630–634. (Cited on page 105)

[Peterson et al., 2012] Peterson, K. D., McFaul, L. W., Schroer, M. D., Jung, M., Taylor, J. M., Houck, A. A., and Petta, J. R. (2012). Circuit quantum electrodynamics with a spin qubit. *Nature*, 490:380–383. (Cited on page 98)

[Phillips, 1972] Phillips, W. (1972). Tunneling states in amorphous solids. *Journal of Low Temperature Physics*, 7(3-4):351–360. (Cited on page 88)

[Phillips, 1987] Phillips, W. A. (1987). Two-level states in glasses. *Reports on Progress in Physics*, 50(12):1657. (Cited on pages 88 and 123)

[Pobell, 2007] Pobell, F. (2007). *Matter and methods at low temperatures*. Springer. (Cited on page 20)

[Poot and van der Zant, 2012] Poot, M. and van der Zant, H. S. (2012). Mechanical systems in the quantum regime. *Physics Reports*, 511(5):273 – 335. (Cited on pages 66 and 67)

[Poot et al., 2007] Poot, M., Witkamp, B., Otte, M. A., and van der Zant, H. S. J. (2007). Modelling suspended carbon nanotube resonators. *physica status solidi (b)*, 244:4252–4256. (Cited on pages 65 and 66)

[Postma et al., 2005] Postma, H. W. C., Kozinsky, I., Husain, A., and Roukes, M. L. (2005). Dynamic range of nanotube- and nanowire-based electromechanical systems. *Applied Physics Letters*, 86(22):223105. (Cited on page 66)

[Postma et al., 2001] Postma, H. W. C., Teepen, T., Yao, Z., Grifoni, M., and Dekker, C. (2001). Carbon Nanotube Single-Electron Transistors at Room Temperature. *Science*, 293(5527):76–79. (Cited on page 1)

[Pothier et al., 1992] Pothier, H., Lafarge, P., Urbina, C., Esteve, D., and Devoret, M. H. (1992). Single-Electron Pump Based on Charging Effects. *EPL (Europhysics Letters)*, 17(3):249. (Cited on page 24)

[Pozar, 2012] Pozar, D. M. (2012). *Microwave enineering*. Wiley. (Cited on pages 83 and 90)

[Purewal et al., 2007] Purewal, M. S., Hong, B. H., Ravi, A., Chandra, B., Hone, J., and Kim, P. (2007). Scaling of Resistance and Electron Mean Free Path of Single-Walled Carbon Nanotubes. *Phys. Rev. Lett.*, 98:186808. (Cited on page 23)

[Radushkevich and Luk'yanovich, 1952] Radushkevich, L. V. and Luk'yanovich, V. M. (1952). The structure of carbon forming in thermal decomposition of carbon monoxide on an iron catalyst (in russian). *Soviet Journal of Chemical Physics*, 26:88–95. (Cited on page 1)

[Ranjan et al., 2015] Ranjan, V., Puebla-Hellmann, G., Jung, M., Hasler, T., Nunnenkamp, A., Muoth, M., Hierold, C., Wallraff, A., and Schonenberger, C. (2015). Clean carbon nanotubes coupled to superconducting impedance-matching circuits. *Nat Commun*, 6:–. (Cited on page 105)

[Sage et al., 2011] Sage, J. M., Bolkhovsky, V., Oliver, W. D., Turek, B., and Welander, P. B. (2011). Study of loss in superconducting coplanar waveguide resonators. *Journal of Applied Physics*, 109(063915). (Cited on pages 91 and 93)

[Saito et al., 1998] Saito, R., Dresselhaus, G., and Dresselhaus, M. S. (1998). *Physical Properties of Carbon Nanotubes*. Imperial College Press. (Cited on page 7)

[Sakurai and Napolitano, 2011] Sakurai, J. J. and Napolitano, J. (2011). *Modern Quantum Mechanics*. Jim Smith. (Cited on page 117)

[Sapmaz et al., 2006a] Sapmaz, S., Jarillo-Herrero, P., Blanter, Y. M., Dekker, C., and van der Zant, H. S. J. (2006a). Tunneling in Suspended Carbon Nanotubes Assisted by Longitudinal Phonons. *Phys. Rev. Lett.*, 96:026801. (Cited on pages 53, 54, 55, 57 and 62)

[Sapmaz et al., 2005] Sapmaz, S., Jarillo-Herrero, P., Kong, J., Dekker, C., Kouwenhoven, L. P., and van der Zant, H. S. J. (2005). Electronic excitation spectrum of metallic carbon nanotubes. *Phys. Rev. B*, 71:153402. (Cited on page 55)

[Sapmaz et al., 2006b] Sapmaz, S., Meyer, C., Beliczynski, P., Jarillo-Herrero, P., and Kouwenhoven, L. P. (2006b). Excited State Spectroscopy in Carbon Nanotube Double Quantum Dots. *Nano Letters*, 6(7):1350–1355. PMID: 16834409. (Cited on page 24)

[Sazonova et al., 2004] Sazonova, V., Yaish, Y., Ustunel, H., Roundy, D., Arias, T. A., and McEuen, P. L. (2004). A tunable carbon nanotube electromechanical oscillator. *Nature*, 431(7006):284–287. (Cited on pages 1 and 65)

[Schmid, 2014] Schmid, D. R. (2014). *Suspended carbon nanotubes as electronical and nano-electro-mechanical hybrid systems in the quantum limit*. PhD thesis, Universität Regensburg. (Cited on pages 23 and 34)

[Schmid et al., 2015a] Schmid, D. R., Smirnov, S., Margańska, M., Dirnaichner, A., Stiller, P. L., Grifoni, M., Hüttel, A. K., and Strunk, C. (2015a). Broken SU(4) symmetry in a Kondo-correlated carbon nanotube. *Phys. Rev. B*, 91:155435. (Cited on page 23)

[Schmid et al., 2015b] Schmid, D. R., Stiller, P. L., Strunk, C., and Hüttel, A. K. (2015b). Liquid-induced damping of mechanical feedback effects in single electron tunneling through a suspended carbon nanotube. *Applied Physics Letters*, 107(12). (Cited on page 104)

[Schmid et al., 2012] Schmid, D. R., Stiller, P. L., Strunk, C., and Hüttell, A. K. (2012). Magnetic damping of a carbon nanotube nano-electromechanical resonator. *New Journal of Physics*, 14(8):083024. (Cited on pages 54, 65, 71 and 104)

[Singh et al., 2014] Singh, V., Schneider, B. H., Bosman, S. J., Merkx, E. P. J., and Steele, G. A. (2014). Molybdenum-rhenium alloy based high-Q superconducting microwave resonators. *Applied Physics Letters*, 105(22):222601. (Cited on pages 91, 95 and 105)

[Steele et al., 2013] Steele, G., Pei, F., Laird, E., Jol, J., Meerwaldt, H., and Kouwenhoven, L. (2013). Large spin-orbit coupling in carbon nanotubes. *Nat Commun*, 4:1573–. (Cited on pages 35 and 36)

[Stiller, 2011] Stiller, P. (2011). Carbon nanotubes as nano-mechanical resonators. Diplomarbeit, Universität Regensburg. (Cited on pages 14, 20 and 23)

[Stiller et al., 2013] Stiller, P., Kugler, S., Daniel, Strunk, C., and Hüttel, A. K. (2013). Negative frequency tuning of a carbon nanotube nano-electromechanical resonator under tension. *physica status solidi (b)*, 250(12):2518–2522. (Cited on pages 2, 54, 65, 74 and 104)

[Svensson and Campbell, 2011] Svensson, J. and Campbell, E. E. B. (2011). Schottky barriers in carbon nanotube-metal contacts. *Journal of Applied Physics*, 110(11):–. (Cited on page 27)

[Tans et al., 1997] Tans, S. J., Devoret, M. H., Dai, H., Thess, A., Smalley, R. E., Geerligs, L. J., and Dekker, C. (1997). Individual single-wall carbon nanotubes as quantum wires. *Nature*, 386(6624):474–477. (Cited on pages 1 and 24)

[Tans et al., 1998] Tans, S. J., Verschueren, A. R. M., and Dekker, C. (1998). Room-temperature transistor based on a single carbon nanotube. *Nature*, 393(6680):49–52. (Cited on pages 1 and 27)

[Tinkham, 2004] Tinkham, M. (2004). *Introduction to superconductivity*. Dover Publication, Inc. (Cited on page 95)

[Toida et al., 2013] Toida, H., Nakajima, T., and Komiyama, S. (2013). Vacuum Rabi Splitting in a Semiconductor Circuit QED System. *Phys. Rev. Lett.*, 110:066802. (Cited on pages 98 and 100)

[Tománek and Louie, 1988] Tománek, D. and Louie, S. G. (1988). First-principles calculation of highly asymmetric structure in scanning-tunneling-microscopy images of graphite. *Phys. Rev. B*, 37:8327–8336. (Cited on page 117)

[Usmani et al., 2007] Usmani, O., Blanter, Y. M., and Nazarov, Y. V. (2007). Strong feedback and current noise in nanoelectromechanical systems. *Phys. Rev. B*, 75:195312. (Cited on pages 71 and 104)

[van der Wiel et al., 2002] van der Wiel, W. G., De Franceschi, S., Elzerman, J. M., Fujisawa, T., Tarucha, S., and Kouwenhoven, L. P. (2002). Electron transport through double quantum dots. *Rev. Mod. Phys.*, 75:1–22. (Cited on page 24)

[van Houten et al., 1992] van Houten, H., Beenakker, C., and Staring, A. (1992). *Single Charge Tunneling*, volume 294. Plenum Press New York. (Cited on page 24)

[Viennot et al., 2015] Viennot, J. J., Dartiailh, M. C., Cottet, A., and Kontos, T. (2015). Coherent coupling of a single spin to microwave cavity photons. *Science*, 349(6246):408–411. (Cited on pages 2 and 100)

[Viennot et al., 2014] Viennot, J. J., Delbecq, M. R., Dartiailh, M. C., Cottet, A., and Kontos, T. (2014). Out-of-equilibrium charge dynamics in a hybrid circuit quantum electrodynamics architecture. *Phys. Rev. B*, 89:165404. (Cited on pages 2, 98, 99 and 100)

[Wallraff et al., 2004] Wallraff, A., Schuster, D. I., Blais, A., Frunzio, L., Huang, R.-S., Majer, J., Kumar, S., Girvin, S. M., and Schoelkopf, R. J. (2004). Strong coupling of a single photon to a superconducting qubit using circuit quantum electrodynamics. *Nature*, 431(7005):162–167. (Cited on pages 2 and 100)

[Wallraff et al., 2013] Wallraff, A., Stockklauser, A., Ihn, T., Petta, J. R., and Blais, A. (2013). Comment on "Vacuum Rabi Splitting in a Semiconductor Circuit QED System". *Phys. Rev. Lett.*, 111:249701. (Cited on page 100)

[Wang et al., 2013] Wang, Y., Zhou, P., Wei, L., Li, H., Zhang, B., Zhang, M., Wei, Q., Fang, Y., and Cao, C. (2013). Photon-induced thermal effects in superconducting coplanar waveguide resonators. *Journal of Applied Physics*, 114(15):–. (Cited on pages 91 and 93)

[Watanabe et al., 1994] Watanabe, K., Yoshida, K., Aoki, T., and Kohjiro, S. (1994). Kinetic Inductance of Superconducting Coplanar Waveguides. *Japanese Journal of Applied Physics*, 33(10R):5708. (Cited on page 97)

[Wen, 1969] Wen, C. (1969). Coplanar Waveguide: A Surface Strip Transmission Line Suitable for Nonreciprocal Gyromagnetic Device Applications. *Microwave Theory and Techniques, IEEE Transactions on*, 17(12):1087–1090. (Cited on page 2)

[White and Todorov, 1998] White, C. T. and Todorov, T. N. (1998). Carbon nanotubes as long ballistic conductors. *Nature*, 393(6682):240–242. (Cited on page 23)

[Witkamp, 2009] Witkamp, B. (2009). *High-frequency nanotube resonators*. PhD thesis, TU Delft. (Cited on page 66)

[Witkamp et al., 2006] Witkamp, B., Poot, M., and van der Zant, H. S. J. (2006). Bending-Mode Vibration of a Suspended Nanotube Resonator. *Nano Letters*, 6(12):2904–2908. (Cited on pages 66 and 68)

[Wu and Zhong, 2011] Wu, C. C. and Zhong, Z. (2011). Capacitive Spring Softening in Single-Walled Carbon Nanotube Nanoelectromechanical Resonators. *Nano Letters*, 11(4):1448–1451. (Cited on page 74)

List of publications

1. D. R. Schmid, P. L. Stiller, Chr. Strunk and A. K. Hüttel: *Magnetic damping of a carbon nanotube NEMS resonator*; New Journal of Physics 14, 083024 (2012)

2. P. L. Stiller, S. Kugler, D. R. Schmid, Chr. Strunk and A. K. Hüttel: *Negative frequency tuning of a carbon nanotube nano-electromechanical resonator under tension*; Physica status solidi (b) 250, 2518 (2013)

3. D. R. Schmid, S. Smirnov, M. Marganska, A. Dirnaichner, P. L. Stiller, M. Grifoni, A. K.Hüttel, Ch. Strunk: *Broken SU(4) symmetry in a Kondo-correlated carbon nanotube*; Physical Review B 91, 155435 (2015)

4. D. R. Schmid, P. L. Stiller, Chr. Strunk and A. K. Hüttel: *Liquid-induced damping of mechanical feedback effects in single electron tunneling through a suspended carbon nanotube*; Applied Physics Letters 107,123110 (2015)

5. K. J. G. Götz, S. Blien, P. L. Stiller, O. Vavra, T. Mayer, T. Huber, T. N. G. Meier, M. Kronseder, Ch. Strunk, A. K. Hüttel: *Co-sputtered MoRe thin films for carbon nanotube growth-compatible superconducting coplanar resonators*, Nanotechnology 27, 135202 (2016)

Danksagung

Ich möchte mich ganz besonders bei allen Personen bedanken, die zum Gelingen dieser Arbeit beigetragen haben.

Großer Dank gilt meinem Betreuer Dr. Andreas K. Hüttel. Lieber Andreas, vielen Dank für die letzten Jahre. Du warst immer mit Rat und Tat zur Stellen, wenn ich etwas gebraucht habe. Die super Zusammenarbeit war wichtig für das Gelingen dieser Arbeit. Ich wünsche dir alles Gute für die Zukunft.

Besonderer Dank gilt Daniel Schmid, danke für die enge Zusammenarbeit in allen Bereichen während unserer gemeinsamen Zeit am Lehrstuhl. Unvergessen bleiben die vielen gemütlichen Stunden neben der ganzen Physik.

Ich danke allen Mitgliedern der Arbeitsgruppe Hüttel für die super Zusammenarbeit in all den Jahren. Besonderer Dank gilt den Masterstudenten Sabine Kugler, Alexander Feigl und Thomas Huber. Bei Stefan Blien bedanke ich mich für die Hilfe und Unterstützung mit dem neuen Mischkryostaten und den Hochfrequenz-Messungen.

Bei Thomas Haller, Michael Weigl, Florian Birkner und Uli Gürster möchte ich mich für die schnelle und professionelle Unterstützung bei allen technischen Problemen in und um den Reinraum bedanken.

Zudem danke ich Thomas Solleder und Christian Haimerl für die professionelle und unkomplizierte Versorgung mit kalten "Flüssigkeiten".

Vielen Dank an unser Sekretariat, Claudia Rahm und Elke Haushalter, für die schnelle Hilfe bei allen Verwaltungsangelegenheiten.

Ich bedanke mich bei allen Mitgliedern der AG Strunk und des gesamten Lehrstuhls Weiss für die super Zusammenarbeit in den letzten Jahren.

Ich möchte mich bei Herrn Prof. Dr. Christoph Strunk für die Unterstützung und die hilfreichen Diskussionen während meiner Promotion bedanken.

Bei Herrn Prof. Dr. Dieter Weiss bedanke ich mich für die perfekt ausgebaute Infrastruktur, die ich jederzeit nutzen konnte und die Möglichkeit, bei der DPG-Tagung in Regensburg mitzuarbeiten.

I want to thank the collaborators of the theory group of Prof. Dr. Milena Grifoni; especially I want to thank Dr. Magdalena Marganska, thank you for helping with the numerical calculations and the helpful discussions about carbon nanotubes. In additions i want to thank Andrea Donarini for the helpful discussions.

Zum Abschluss möchte ich meinen Eltern danken für die tolle Unterstützung in all den Jahren meines Studiums und meiner Promotion. Vieles hätte ohne euch so nicht funktioniert!

Nachträgliche Änderungen

- Seite 6: Der Satz "An important quantity for graphene and also carbon nanotubes is the so-called chiral vector" wurde nachträglich zu "An important quantity for carbon nanotubes is the so-called chiral vector " geändert.

- Seite 6: "Together with the translation vector $\vec{T}$ they built up the carbon nanotube unit cell, each unit cell contains two carbon atoms. Two sublattices called A and B arise." wurde nachträglich zu "Together with the translation vector $\vec{T}$ it defines the carbon nanotube unit cell." geändert.

- Seite 7, Abbildung 2.1: Die Grafik wurde inhaltlich nicht verändert, nur komplett neu gezeichnet, um sie an den Text anzupassen.

- Seite 8: Der Satz "Only two of the six corner points are independent in the graphene lattice," wurde nachträglich zu "Only two of the six corner points are independent in the reciprocal graphene lattice," geändert.

- Seite 9, Formel 2.10: Die Formel "$0 \cdot (m+n) \pm \frac{4\pi}{3} \cdot \frac{a}{2} (m-n) = 2\pi q$." wurde nachträglich zu "$0 \cdot (m+n) \pm \frac{4\pi}{3} \cdot \frac{1}{2} (m-n) = 2\pi q$." geändert.

- Seite 9: Der Satz "Armchair carbon nanotubes are rolled up in $\vec{k}_x$-direction;" wurde nachträglich zu "Armchair carbon nanotubes are rolled up in $\vec{x}$-direction;" geändert.

- Seite 10: Der Satz "In a zigzag type carbon nanotube, rolled up in $\vec{k}_y$ direction, the quantization is given by" wurde nachträglich zu "In a zigzag type carbon nanotube the quantization is given by" geändert.

- Seite 28, Abbildung 4.3: Abbildung wurde nachträglich geändert, da die Fermie-Energie falsch eingezeichnet war.

- Seite 29: "excited charging state $\mu^*(N)$" wurde nachträglich zu "excited state $\mu^*(N)$" geändert.
- Seite 42, Abbildung 5.3(e): Linienschnitt für $\delta = 0.0008$ wurde nachträglich korrigiert. Ebenso: $\Delta = \sqrt{\Delta_{\mathrm{SO}}^2 + \Delta_{\mathrm{KK'}}^2}$
- Seite 46, Abbildung 5.6(d): Die falsche y-Achsenbeschriftung wurde nachträglich korrgiert. Die richtige y-Achsenwerten gehen von 10 meV bis 13 meV.
- Seite 53: Der Satz "The interplay of electronic transport and mechanical motion was first observed in a C_{60}-oscillator." wurde nachträglich zu "The interplay of electronic transport and mechanical motion in single electron tunneling was first observed in a C_{60}-oscillator." geändert.
- Seite 54: Die Formel "$E_{\mathrm{RBM}} = \frac{27.8}{d}$ meV." wurde nachträglich zu "$E_{\mathrm{RBM}} = \frac{27.8}{d[nm]}$ meV." geändert.
- Seite 55, Abbildung 6.1: Die Einheit "eV" wurde durch "meV" ersetzt und "Leturcq, Nature" wurde durch "Leturcq, Nature Phys." ersetzt.
- Seite 56, Formel 6.5: Die Formel "$P_n = \sum_n P_n = 1$" wurde zu "$Q_n = \sum_n P_n = 1$" geändert.
- Seite 56: Der Satz "the initial state involved in the vibrational transition is then always in its ground state." wurde nachträglich zu "the initial state involved in the vibrational transition is then always its ground state." geändert.
- Seite 58, Abbildung 6.2: P_n wurde durch Q_n ersetzt.
- Seite 75, Formel 7.16: Die Formel "$f\left(V_{\mathrm{gate}}\right) = f_{\mathrm{max}} - \beta\left(V_{\mathrm{gate}} - V_{\mathrm{gate,0}}\right)$" wurde nachträglich zu "$f\left(V_{\mathrm{gate}}\right) = f_{\mathrm{max}} - \beta\left(V_{\mathrm{gate}} - V_{\mathrm{gate,0}}\right)^2$" geändert.
- Seite 91: Der Satz "F is given by the ration of the stored energy in TLS and the total stored energy of the microwave resonator." wurde nachträglich zu "F is given by the ration of the stored energy in the TLS host material and the total stored energy of the microwave resonator." geändert.
- Seite 98: Der Satz "In literature the deviations are assumed to be due to disorder in the superconducting resonator material [Driessen et al., 2012, Coumou et al., 2013]; a generalized Mattis-Bardeen theory employing a broadened quasi-particle density of states with an effective pair-breaking." wurde nachträglich zu "In literature the deviations are assumed to be due to disorder in the superconducting resonator material [Driessen et al., 2012, Coumou et al., 2013]; a generalized Mattis-Bardeen theory employing a broadened quasi-particle density of states with an effective pair-breaking is used." geändert.

- Seite 105: Der Satz "Carbon nanotubes are grown by CVD on silicon stamps and transferred to a device with pre-defined metallic contacts;" wurde nachträglich zu "Carbon nanotubes are grown by CVD on SiO_2 stamps and transferred to a device with pre-defined metallic contacts;" geändert.
- Seite 141: "Co-sputtered MoRe thin films for carbon nanotube growth-compatible superconducting coplanar resonators" wurde mittlerweile veröffentlicht; die endgültigen bibliographischen Daten wurden eingefügt.